



UNIVERSIDAD DE INVESTIGACIÓN DE TECNOLOGÍA EXPERIMENTAL YACHAY

Escuela de Ciencias Físicas y Nanotecnología

TÍTULO:

Analysis of the winds that influence Ecuador considering the presence of the Ecuadorian Andes using the Model for Prediction Across Scales (MPAS)

Trabajo de integración curricular presentado como requisito para la obtención del título de Física

Autor:

Gabriela Lizbeth Cruz Pillaga

Tutor:

Wladimir Banda-Barragán, Ph.D

Co-tutor:

Oscar Chimborazo, Ph.D

Urcuquí, Noviembre de 2024

Autoría

Yo, **Gabriela Lizbeth Cruz Pillaga**, con cédula de identidad 0350331815, declaro que las ideas, juicios, valoraciones, interpretaciones, consultas bibliográficas, definiciones y conceptualizaciones expuestas en el presente trabajo; así como, los procedimientos y herramientas utilizadas en la investigación, son de absoluta responsabilidad de el/la autor/a del trabajo de integración curricular. Así mismo, me acojo a los reglamentos internos de la Universidad de Investigación de Tecnología Experimental Yachay.

Urcuquí, Noviembre 2024.

Gabriela Lizbeth Cruz Pillaga
CI: 0350331815

Autorización de publicación

Yo, **Gabriela Lizbeth Cruz Pillaga**, con cédula de identidad 0350331815, cedo a la Universidad de Investigación de Tecnología Experimental Yachay, los derechos de publicación de la presente obra, sin que deba haber un reconocimiento económico por este concepto. Declaro además que el texto del presente trabajo de titulación no podrá ser cedido a ninguna empresa editorial para su publicación u otros fines, sin contar previamente con la autorización escrita de la Universidad.

Asimismo, autorizo a la Universidad que realice la digitalización y publicación de este trabajo de integración curricular en el repositorio virtual, de conformidad a lo dispuesto en el Art. 144 de la Ley Orgánica de Educación

Urcuquí, Noviembre, 2024.

Gabriela Lizbeth Cruz Pillaga
CI: 0350331815

Dedication

A mi madre, siempre a mi madre.

*Con amor,
Gaby.*

Acknowledgment

*"Hoy que el tiempo ya pasó...
hoy que me río si pienso...
no sé por qué me despierto
algunas noches vacías
oyendo una voz que canta
y que, tal vez, es la mía."*
—**Idea Vilariño**

Agradezo a la educación pública, por brindarme una formación que va más allá de los libros y exámenes. A Yachay y a todos sus maestros, en particular, al profesor Oscar, cuya paciencia y comprensión siempre me hicieron sentir capaz -su amabilidad nunca pasó desapercibida-; y al profesor Wladimir, cuya meticulosa guía no solo me instruyó, sino que cultivó en mí una profunda admiración.

A mi mami China, que me crió con una tacita de café en la mano, con la convicción de que la ternura es la más poderosa de las fortalezas; y a mi madre, mi propia "Lorelai Gilmore", a quien le debo todo lo que soy.

A mis amigos: a Damián, que sin pedir nada me regaló todo su amor; a Mila, mi amiga estupenda, por enseñarme tanto a través de pedacitos de canciones; y a Jean, que me abrió las puertas de su corazón y de su casa. (También a Criss, que me cuidó sin darse cuenta, cuando yo no sabía cómo hacerlo).

A las mujeres cuyas palabras han sido mi faro y refugio en estos años universitarios: Virginia, Clarice, Sylvia, Idea, Alejandra y Annie; sus voces son mi abrazo en el mundo.

Finalmente, quisiera expresar mi agradecimiento CEDIA por proporcionar los recursos de computación de alto rendimiento (HPC) que fueron cruciales para esta investigación y al apoyo brindado por el Centro de Modelización Matemática en Áreas Clave para el Desarrollo (MODEMAT) en la Escuela Politécnica Nacional (EPN) que facilitaron la finalización de este estudio.

La autora de esta tesis reconoce el uso del siguiente software de acceso público: 1) para el análisis y visualización de datos, la biblioteca de Python UXarray [1] y Xarray [2], y la biblioteca de Python Matplotlib [3]; y 2) para mejorar la claridad del texto, ChatGPT/Grammarly [4], que solo se utilizó para corregir errores gramaticales y ortográficos en partes seleccionadas del texto.

Resumen

Comprender las dinámicas físicas que gobiernan los procesos atmosféricos y su interacción con las características topográficas del terreno es esencial para la predicción precisa del clima y el tiempo. Este estudio emplea el Modelo de Predicción a Escalas (MPAS) para investigar el impacto de la Cordillera de los Andes en los patrones de viento, la humedad relativa y la precipitación en Ecuador. Se realizaron simulaciones en cuatro escenarios con diferentes alturas de la montaña: altura real, mitad de la altura, 10% de la altura y 1% de la altura. Los resultados indican perturbaciones significativas en los patrones de viento y niveles elevados de humedad en las simulaciones con el terreno real, especialmente durante eventos de El Niño. En contraste, las simulaciones con terrenos más planos muestran patrones de viento uniformes y valores de humedad consistentes. Además, los mapas de precipitación revelan una alta variabilidad en las regiones influenciadas por la elevación, lo que subraya el papel crítico de los Andes en la configuración de las dinámicas climáticas regionales. Estos hallazgos contribuyen a una comprensión más profunda de la relación intrincada entre la topografía del terreno y los procesos atmosféricos en Ecuador.

Palabras Clave: Dinámicas atmosféricas, vientos alisios, procesos hidrológicos, cordillera de los Andes

Abstract

Understanding the physical dynamics governing atmospheric processes and their interaction with topographical features of the terrain is essential for accurate weather and climate prediction. This study employs the Model for Prediction Across Scales (MPAS) to investigate the impact of the Andes Mountains on wind patterns, relative humidity, and precipitation in Ecuador. Simulations were conducted across four scenarios with different mountain heights: actual height, half the height, 10% of the height, and 1% of the height. The results indicate significant disturbances in wind patterns and elevated humidity levels in real terrain simulations, particularly during El Niño events. In contrast, flatter terrain simulations exhibit uniform wind patterns and consistent humidity values. Additionally, precipitation maps show high variability in regions influenced by elevation, underscoring the Andes' critical role in shaping regional climate dynamics. These insights contribute to a deeper understanding of the intricate relationship between terrain topography and atmospheric processes in Ecuador.

Keywords: Atmospheric dynamics, trade winds, hydrological processes, Andes Mountains

Contents

Autoría

Autorización de publicación

Dedication

Acknowledgment

Resumen

Abstract

Contents

List of Tables

List of Figures

| | | |
|----------|---|----------|
| 1 | Introduction | 1 |
| 1.1 | Background | 1 |
| 1.1.1 | Meteorological Data: From Data Collection to Climate Modeling | 2 |
| 1.1.2 | Climate Studies in the Andean Region | 3 |
| 1.1.3 | Climate Studies in Ecuador | 4 |
| 1.1.4 | Influence of Geography on Numerical Models | 5 |
| 1.2 | Problem statement | 5 |
| 1.3 | Objectives | 6 |
| 1.3.1 | General Objective | 6 |
| 1.3.2 | Specific Objectives | 6 |
| 2 | Methodology | 7 |
| 2.1 | Software Tools | 8 |
| 2.1.1 | Data Sources | 8 |
| 2.1.2 | ENSO and date selection: | 9 |
| 2.1.3 | Preprocessing Tools | 12 |

| | | |
|----------|--|-----------|
| 2.1.4 | Data Transformation and Integration: | 12 |
| 2.2 | Simulation | 13 |
| 2.2.1 | Model Components | 13 |
| 2.2.2 | Model Parametrization Schemes | 13 |
| 2.2.3 | Initial and Boundary Conditions | 15 |
| 2.2.4 | Governing Equations | 16 |
| 2.3 | Hardware | 18 |
| 2.3.1 | HPC Configuration | 18 |
| 2.4 | Specific Scenarios and Numerical Experiments | 19 |
| 3 | Results and Discussion | 20 |
| 3.1 | Regional Wind Patterns | 20 |
| 3.1.1 | Wind Component Analysis | 20 |
| 3.2 | Role of the Andes Elevation | 32 |
| 3.2.1 | Half Height | 33 |
| 3.2.2 | 10% Height | 35 |
| 3.2.3 | 1% Height | 37 |
| 3.2.4 | Overall Elevation Impact | 38 |
| 3.3 | Vertical Cross-Section Analysis | 39 |
| 3.3.1 | Cayambe Mountain | 40 |
| 3.3.2 | Chimborazo Mountain | 42 |
| 3.3.3 | Sangay Mountain | 45 |
| 3.4 | Impact on El Niño and La Niña Events | 47 |
| 3.4.1 | Relative Humidity: Strong vs Weak El Niño Analysis | 47 |
| 3.4.2 | Relative Humidity: Strong vs Weak La Niña Analysis | 51 |
| 3.4.3 | Overall relative humidity observations | 55 |
| 3.4.4 | Precipitation: Strong vs Weak El Niño Analysis | 55 |
| 3.4.5 | Precipitation: Strong vs Weak La Niña Analysis | 57 |
| 3.4.6 | Overall precipitation observations | 58 |
| 4 | Conclusions | 59 |
| | Bibliography | 61 |
| | Appendices | 66 |
| .1 | Appendix 1. | 68 |
| .2 | Additional Figures | 69 |
| .3 | Appendix 2: MPAS-Atmosphere Configuration Files | 70 |
| .4 | namelist.init_atmosphere | 70 |
| .5 | namelist.atmosphere | 72 |

List of Tables

| | | |
|-----|---|----|
| 2.1 | Key Periods of El Niño and La Niña Phenomena with ONI Values[5, 6, 7, 8, 9, 10, 11, 12, 13, 14, 15] | 11 |
| 2.2 | The parameterization schemes featured in the ‘convection-permitting’ physics suite. | 14 |
| 2.3 | Topographic Scenarios for Wind Pattern Simulations | 19 |

List of Figures

| | | |
|-----|--|----|
| 1.1 | Infographic illustrating the difference between weather and climate. | 1 |
| 1.2 | Flowchart of the Meteorological Data Processing Workflow | 3 |
| 1.3 | Topographic map of continental Ecuador showing elevation contours. Figure reproduced from Ortiz-Prado et al. (2021)[16] | 4 |
| 2.1 | SCVT grids on a spherical surface. The left globe shows a coarse grid suitable for broad analysis, while the right globe presents a finer grid for detailed studies. Adapted from source: MPAS-Dev Atmosphere [17]. | 8 |
| 2.2 | Worldwide distribution and impact of the El Niño (left) and La Niña (right) events during winter (up) and summer (bottom). Source: Giralt et al. (2007) [18]. | 9 |
| 2.3 | Schematic structure of the MPAS-A model components. The MPAS Superstructure includes separate initialization (init_atmosphere) and simulation (atmosphere) modules, built on the common infrastructure. Figure reproduced from MPAS-Atmosphere Model User’s Guide: Version 8.1.0 [19]. . . | 13 |
| 2.4 | Static geographical data for Ecuador used in the climatological simulations. The elliptical region centered over Ecuador includes its coastal plains, the Andean highlands, and the Amazon rainforest, ensuring comprehensive coverage of the area’s diverse topography for accurate atmospheric modeling. . | 15 |
| 2.5 | Terrain Elevations for the Analysis: This figure shows the terrain elevation at different data resolutions: (a) Full, (b) Half, (c) 10%, and (d) 1% of the terrain. The color bar indicates elevation from 0 to over 5000 meters. . . . | 19 |
| 3.1 | Wind patterns at 850 hPa over Ecuador in March 1983 (Real Terrain), showing variability influenced by the Andes. White arrows indicate wind direction, with length corresponding to 5 m/s. | 21 |
| 3.2 | Wind patterns at 850 hPa over Ecuador in February 1998 (Real Terrain), showing interactions between coastal and highland air masses. White arrows indicate wind direction, with length corresponding to 5 m/s. | 22 |
| 3.3 | Wind patterns at 850 hPa over Ecuador in February 2016 (Real Terrain), highlighting complex wind deflections due to the Andes. White arrows indicate wind direction, with length corresponding to 5 m/s. | 23 |
| 3.4 | Wind patterns at 850 hPa over Ecuador in October 2004 (Real Terrain), showing complex convergence and divergence. White arrows indicate wind direction, with length corresponding to 5 m/s. | 24 |

| | | |
|------|--|----|
| 3.5 | Wind patterns at 850 hPa over Ecuador in February 2007 (Real Terrain), showing significant wind variability due to the Andes. White arrows indicate wind direction (5 m/s reference), with speeds up to ~ 21 m/s and complex convergence and divergence patterns. | 25 |
| 3.6 | Wind patterns at 850 hPa over Ecuador in January 2010 (Real Terrain), showing complex convergence and divergence. White arrows indicate wind direction (5 m/s reference), with speeds up to ~ 16.8 m/s. | 26 |
| 3.7 | Wind patterns at 850 hPa over Ecuador in January 1989 (Real Terrain), showing complex convergence and divergence. White arrows indicate wind direction (5 m/s reference), with speeds up to ~ 12.8 m/s. | 27 |
| 3.8 | Wind patterns at 850 hPa over Ecuador in November 1998 (Real Terrain), showing complex convergence and divergence. White arrows indicate wind direction (5 m/s reference), with speeds up to ~ 16.8 m/s. | 28 |
| 3.9 | Wind patterns at 850 hPa over Ecuador in January 2011 (Real Terrain). White arrows indicate wind direction (5 m/s reference), with speeds up to ~ 14.4 m/s. | 29 |
| 3.10 | Wind patterns at 850 hPa over Ecuador in October 1984 (Real Terrain). White arrows indicate wind direction (5 m/s reference). | 30 |
| 3.11 | Wind patterns at 850 hPa over Ecuador in December 1995 (Real Terrain), showing complex convergence and divergence. White arrows indicate wind direction (5 m/s reference), with speeds up to ~ 14.4 m/s. | 31 |
| 3.12 | Wind patterns at 850 hPa over Ecuador for three consecutive days in January 2001 (Real Terrain). The white arrows on the wind vector maps indicate wind direction, with their length corresponding to a reference wind speed of 5 m/s. complex patterns of convergence and divergence, with wind speeds reaching up to ~ 14.4 m/s | 32 |
| 3.13 | Wind patterns at 850 hPa over Ecuador on March 24, 1983 (Half Height). Less pronounced patrons are observed compared to the actual height scenario. | 33 |
| 3.14 | Wind patterns at 850 hPa over Ecuador on February 16, 2007 (Half Height). Notable convergence and divergence patterns, with wind speeds reaching up to 21 m/s. | 33 |
| 3.15 | Wind patterns at 850 hPa over Ecuador on November 6, 1998 (Half Height) | 34 |
| 3.16 | Wind patterns at 850 hPa over Ecuador on December 11, 1995 (Half Height) | 34 |
| 3.17 | Wind patterns at 850 hPa over Ecuador on March 24, 1983 (10% Height) . | 35 |
| 3.18 | Wind patterns at 850 hPa over Ecuador on February 16, 2007 (10% Height) | 35 |
| 3.19 | Wind patterns at 850 hPa over Ecuador on November 6, 1998 (10% Height) | 36 |
| 3.20 | Wind patterns at 850 hPa over Ecuador on December 11, 1995 (10% Height) | 36 |
| 3.21 | Wind patterns at 850 hPa over Ecuador on March 24, 1983 (1% Height) . | 37 |
| 3.22 | Wind patterns at 850 hPa over Ecuador on February 16, 2007 (1% Height) | 37 |
| 3.23 | Wind patterns at 850 hPa over Ecuador on November 6, 1998 (1% Height) | 38 |
| 3.24 | Wind patterns at 850 hPa over Ecuador on December 11, 1995 (1% Height) | 38 |
| 3.25 | Ecuador's Peaks: Cayambe, Chimborazo, and Sangay - This map highlights the geographic locations and elevations of Cayambe (5790m), Chimborazo (6263m), and Sangay (5230m), representing the significant mountainous landmarks in the northern, central, and southern regions of Ecuador respectively. | 39 |

| | | |
|------|---|----|
| 3.26 | Zonal Wind at 850 hPa around the Cayambe Mountain, March 1983 . . . | 40 |
| 3.27 | Zonal Wind at 850 hPa around the Cayambe Mountain, February 2007 . . | 41 |
| 3.28 | Zonal Wind at 850 hPa around the Cayambe Mountain, November 1998 . | 41 |
| 3.29 | Zonal Wind at 850 hPa around the Cayambe Mountain, December 1995 . . | 42 |
| 3.30 | Zonal Wind at 850 hPa around the Chimborazo Mountain, March 1983 . . | 43 |
| 3.31 | Zonal Wind at 850 hPa around the Chimborazo Mountain, Feb 2007 . . . | 43 |
| 3.32 | Zonal Wind at 850 hPa around the Chimborazo Mountain, November 1998 | 44 |
| 3.33 | Zonal Wind at 850 hPa around the Chimborazo Mountain, December 1995 | 44 |
| 3.34 | Zonal Wind at 850 hPa around the Sangay Mountain, March 1983 | 45 |
| 3.35 | Zonal Wind at 850 hPa around the Sangay Mountain, February 2007 . . . | 46 |
| 3.36 | Zonal Wind at 850 hPa around the Sangay Mountain, November 1998 . . . | 46 |
| 3.37 | Zonal Wind at 850 hPa around the Sangay Mountain, December 1995 . . . | 47 |
| 3.38 | Comparative Analysis of Relative Humidity at 850hPa - Strong and Weak El Niño Events (Real terrain vs 1% terrain) | 49 |
| 3.39 | Vertical cross section comparison of Relative Humidity at Chimborazo Moun- tain - March 24, 1983 | 50 |
| 3.40 | Vertical cross-section comparison of relative humidity at Chimborazo Moun- tain - Feb 16, 2007 (Real terrain vs 1% of the terrain) | 50 |
| 3.41 | Comparative Analysis of Relative Humidity at 850hPa - Strong and Weak La Niña Events (Real terrain vs 1% terrain) | 52 |
| 3.42 | Vertical cross-section comparison of relative humidity at Chimborazo Moun- tain - Nov 06, 1998 (Real terrain vs 1% of the terrain) | 53 |
| 3.43 | Vertical cross-section comparison of relative humidity at Chimborazo Moun- tain - Dec 11, 1995 (Real terrain vs 1% of the terrain) | 54 |
| 3.44 | Comparative Analysis of Precipitation - Strong and Weak El Niño Events (Real terrain vs 1% of the terrain) | 56 |
| 3.45 | Comparative Analysis of Precipitation - Strong and Weak La Niña Events (Real terrain vs 1% of the terrain) | 57 |
| 1 | Workflow of MPAS-A Data Handling and Simulation. | 68 |
| 2 | Bounding Circle Subsets Around Ecuadorian Mountains used in our study | 69 |

Chapter 1

Introduction

1.1 Background

Atmospheric processes encompass a wide range of physical phenomena that shape the behavior of the Earth's atmosphere, affecting weather and climate. Among these processes are the circulation of air masses, precipitation, cloud formation, and the transfer of energy between the Earth's surface and the atmosphere. In essence, weather refers to the short-term variations in atmospheric conditions [20], such as temperature, wind speed, humidity, and precipitation, which can fluctuate from one moment to the next. Conversely, climate describes the long-term average of weather patterns over extended periods [21], typically spanning decades or centuries, as illustrated in Figure 1.1. Understanding the distinction between weather and climate is crucial for studying both, i.e., immediate atmospheric conditions and long-term trends [22].

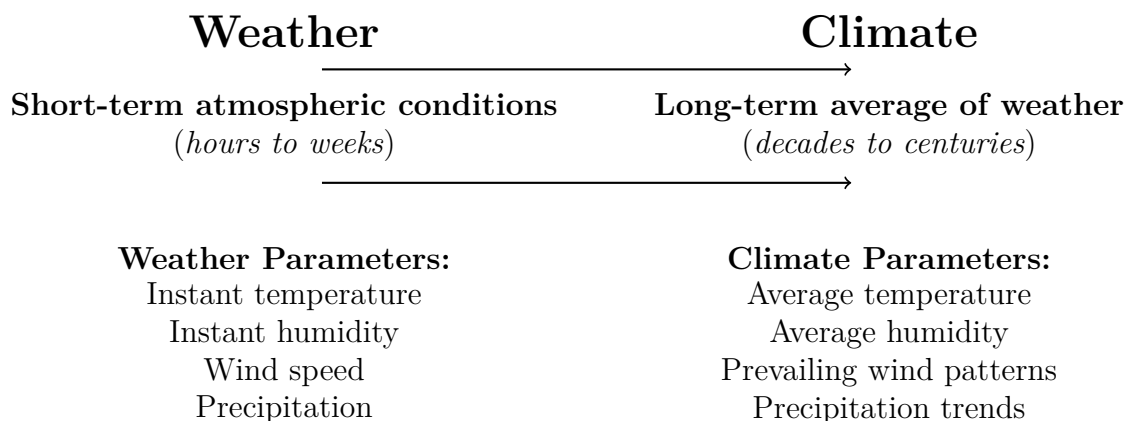


Figure 1.1: Infographic illustrating the difference between weather and climate.

Seasonal variations, driven by the tilt of the Earth's axis and its orbit around the Sun, result in changes in Solar radiation received at different latitudes throughout the year. These variations cause distinct seasonal weather patterns, influencing agriculture, water resources, and ecosystems. Accurate prediction of phenomena such as droughts, heat waves,

rainy periods, and hurricanes, which have substantial socio-economic consequences, relies on a deep understanding of these cycles.

In addition, the analysis of seasonal cycles introduces complexity when examining climate change, which refers to long-term shifts in average weather patterns mainly influenced by human activities such as industrial processes, burning fossil fuels, and deforestation. These activities elevate the concentration of greenhouse gases in the atmosphere, resulting in global warming[23]. The consequences of climate change are extensive, including rising global temperatures, glacier melting, sea-level rise, and more frequent and intense extreme weather events[24]. Addressing these impacts requires an understanding of atmospheric processes and the interactions between different components of the global climate system. Progress in atmospheric science, including the innovation of satellites, ground-based sensors, and sophisticated numerical models, has greatly improved our capacity to monitor and forecast atmospheric changes[25]. These instruments are crucial for developing effective strategies to combat climate change, enabling us to adapt to its effects towards a more sustainable future.

1.1.1 Meteorological Data: From Data Collection to Climate Modeling

Collecting and processing meteorological data is critical for understanding climate and weather patterns. Over the past century, weather forecasting has evolved from an art based on experience and intuition into a science built on synoptic data processing and numerical models that incorporate the principles of mass, momentum, and energy conservation[22]. In Ecuador, the establishment of the first meteorological station at the Astronomical Observatory of Quito (OAQ)¹ in 1873 marked the beginning of systematic climate monitoring. This historical context sets the stage for discussing how these data have been leveraged for modern climate studies.

Meteorological stations are equipped with various instruments including thermometers, barometers, hygrometers, and so on, to measure temperature, pressure, relative humidity, and other climatic variables. These measurements are taken regularly to guarantee consistent and reliable data collection. However, the data may contain errors due to equipment malfunctions or environmental factors, making it essential to review and clean the data before they are used for scientific purposes [26]. This meticulous data collection and validation process is fundamental to the high-performance computing (HPC) systems used in advanced climate simulations.

The data processing pipeline for meteorological data can be visualized in a flowchart (Figure 1.2), illustrating the steps from data collection to climate modeling. Once validated and cleaned, the data are processed using HPC systems to facilitate numerical modeling and simulation. The initial step involves ingesting the cleaned data into centralized databases, such as the European Centre for Medium-Range Weather Forecasts (ECMWF) database², the National Centers for Environmental Information (NCEI)³ database, and the Earth

¹OAQ official website: <https://oaq.epn.edu.ec>.

²ECMWF website: <https://www.ecmwf.int/>

³NCEI website: <https://www.ncei.noaa.gov/>

System Grid Federation (ESGF)⁴. These databases are then used for preprocessing to standardize formats, such as NetCDF (Network Common Data Form), GRIB (Gridded Binary), and HDF (Hierarchical Data Format), and correct any remaining inconsistencies. Numerical models that simulate atmospheric behavior use these data to predict weather and climate patterns; such models are run on HPC facilities at high numerical resolutions to provide detailed and accurate forecasts. Data assimilation techniques further refine these models by integrating real-time observations, enhancing the initial conditions, and improving forecast accuracy [27].

Following data assimilation, ensemble forecasting methods frequently measure uncertainty by conducting multiple simulations with slightly varied initial conditions. This technique helps in understanding the range of possible outcomes and improves forecast reliability. The reliability is usually evaluated by comparing the predicted events with observed variability and historical events, ensuring forecasts are well-calibrated and aligned with recorded outcomes.

The results undergo postprocessing, which includes interpolation, statistical analysis, and visualization, to generate user-friendly weather forecasts and climate analyses and products, such as daily weather forecasts, severe weather warnings, and long-term climate change projections, among others [28]. Additionally, verification processes, done both qualitatively and quantitatively, are essential to compare model outputs with observed data, ensuring the continuous improvement of the models.

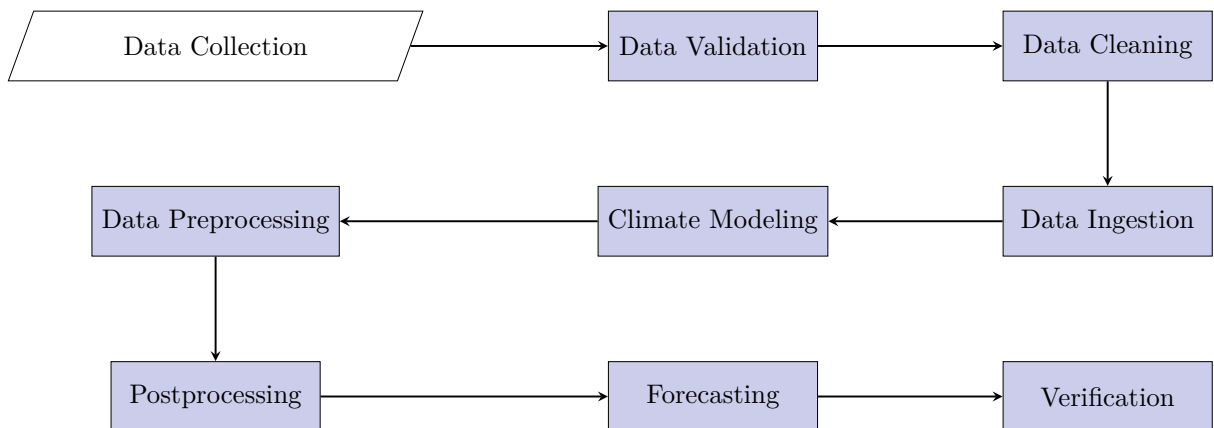


Figure 1.2: Flowchart of the Meteorological Data Processing Workflow

1.1.2 Climate Studies in the Andean Region

The complex topography of the Andes significantly influences regional climate, resulting in diverse weather patterns. Garreaud, Vuille, and Clement (2003)[29] explored the Altiplano in Bolivia, demonstrating how high elevations enhance precipitation on windward slopes and create arid conditions on leeward sides due to orographic effects. Their study highlights the critical role of topography in shaping local weather systems. Building on this, Falvey and Garreaud (2007)[30] investigated winter precipitation in central Chile using the

⁴ESGF website: <https://esgf.llnl.gov/>

Weather Research and Forecasting (WRF) model. They illustrated how the Andes shape seasonal rainfall and influence atmospheric circulation. Their work underscores the role of mountains in channeling moisture and influencing precipitation patterns, which is vital for regional water management and agriculture.

Adding to the understanding of Andean climate dynamics, Vuille et al. (2008)[31] examined climate change in the tropical Andes covering parts of Venezuela, Colombia, Ecuador, Peru, Bolivia, Chile, and Argentina. Their study focused on how altitude and topography create unique temperature and precipitation patterns. They found substantial temperature variations over short distances, resulting in diverse climatic zones from tropical lowland areas to high-altitude environments. This research underscores the complex interactions between altitude, topography, and climate, offering crucial insights into long-term climatic patterns in the Andes.

Together, these studies emphasize the pivotal influence of the Andes on regional climate dynamics.

1.1.3 Climate Studies in Ecuador

In Ecuador, climate studies have delved into the intriguing complexity of climatic patterns, a result of the country's diverse topography. From the coastal plains to the towering Andes mountains, the geography of continental Ecuador creates a myriad of microclimates that significantly influence local weather patterns (see Figure 1.3). Researchers have harnessed a combination of empirical data from meteorological stations and advanced numerical models to unravel these intricate patterns.

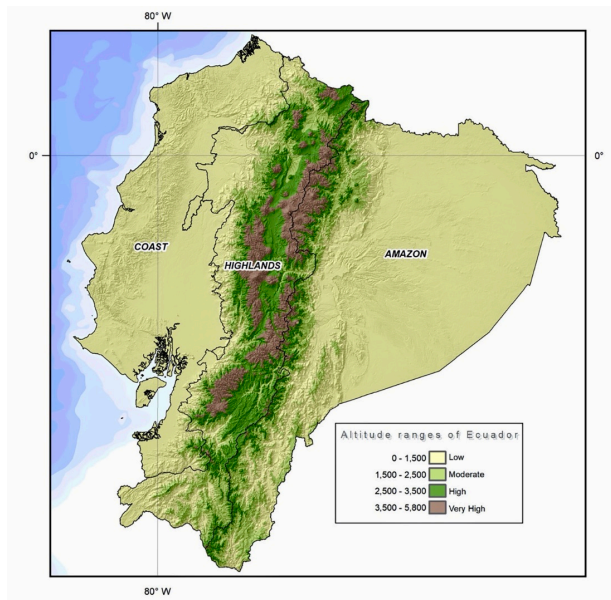


Figure 1.3: Topographic map of continental Ecuador showing elevation contours. Figure reproduced from Ortiz-Prado et al. (2021)[16]

Vuille et al. (2000)[32] examined seasonal precipitation and temperature variability in the Andes of Ecuador, revealing how both Pacific and Atlantic sea surface temperature

anomalies affect local climates. Their research demonstrated that El Niño and La Niña events have differing impacts on precipitation in various parts of the Andes, illustrating the complex interplay between local and large-scale climatic drivers. Specifically, El Niño events are associated with below-average precipitation, while La Niña events bring above-average precipitation. These impacts are most pronounced in the western Andes, where ENSO-induced atmospheric circulation anomalies significantly alter moisture advection patterns, leading to dry conditions during El Niño and wetter conditions during La Niña periods.

Complementing this, Rollenbeck and Bendix (2011)[33] combined weather radar data and meteorological measurements to analyze rainfall distribution in the southern Andes of Ecuador. The integration of high-resolution radar images and in-situ measurements provided a comprehensive understanding of the spatial variability of rainfall, which is crucial for water resource management and agricultural planning. The authors identified significant spatial variability in rainfall distribution, with pronounced heterogeneity driven by interactions between advective rain from the Amazon, convective cloud systems, valley and mountain breeze systems, and terrain-specific moisture transport.

Furthermore, Espinoza Villar et al. (2015)[34] conducted a study on rainfall hot spots in the southern tropical Andes, including areas within Ecuador. Their research identified regions with high rainfall intensity and examined the relationship between these patterns and large-scale atmospheric circulation.

These studies collectively emphasize the importance of understanding climatic dynamics in Ecuador, particularly the influence of the Andes on regional weather patterns.

1.1.4 Influence of Geography on Numerical Models

Geographic features significantly influence the creation of microclimates, which are small-scale climatic conditions that differ from their surroundings [35]. In Ecuador, the Andes Mountains generate diverse microclimates due to variations in elevation, slope orientation, and proximity to water bodies. For instance, the eastern slopes of the Andes experience heavy rainfall from moist air masses originating in the Amazon, while the inter-Andean valleys tend to be drier. These microclimates impact local weather patterns and pose challenges for accurate climate modeling[36].

Incorporating geographic aspects into numerical models enhances the accuracy of climate simulations. Previous studies by Morán-Tejeda et al. (2016) and Ochoa et al. (2014) used detailed topographical data to analyze the long-term trends in precipitation and temperature across different regions of Ecuador. These models underscore the importance of considering mountain ranges and valleys in climate simulations. Including these elements allows models to capture the variability and dynamics of microclimates better, leading to more accurate predictions and informed environmental management decisions [37, 38].

1.2 Problem statement

The Andes Mountains significantly impact the regional atmospheric circulation in Ecuador by acting as a topographical barrier that modifies easterly trade winds and affects humidity

transport. This interaction results in orographic lifting, where air is forced to ascend over the mountains, cools, and condenses, leading to precipitation. It also causes wind direction changes and the formation of diverse microclimates.

Understanding these physical interactions, influenced by the Andes mountains, is essential for accurate weather and climate predictions in the region. Traditional atmospheric models, often relying on uniform grids, have proven effective for large-scale climate simulations [39]. However, they must still improve in areas with complex topographies like the Andes. These uniform grids require tweaks to faithfully represent the intricate variations in elevation and landscape features, leading to less precise weather and climate predictions. This limitation underscores the pressing need to develop more adaptable grid systems.

Our research employs the Model for Prediction Across Scales (MPAS)⁵ that utilizes an unstructured Voronoi, tessellation-based, C-grid discretization. This mesh can dynamically adapt to the geographical features of the study area, allowing for an accurate representation of Ecuador’s varied topography. This tool will enable us to capture the fine-scale atmospheric variations caused by the Andes and other geographical features. These specialized meshes, tailored to the geography of Ecuador, are important for improving the simulations of its weather and microclimates and providing reliable predictions for weather and climate-related phenomena.

1.3 Objectives

1.3.1 General Objective

We aim to analyze the atmospheric dynamics over Ecuador, focusing on the influence of the Ecuadorian Andes. We use the Model for Prediction Across Scales (MPAS), which adapts dynamically to complex topography, providing more accurate simulations and reliable predictions.

1.3.2 Specific Objectives

- Conduct a comprehensive review of existing research on atmospheric dynamics in the Andes, emphasizing the capabilities and applications of the Model for Prediction Across Scales (MPAS).
- Determine the optimal MPAS setup for the continental Ecuador region and run simulations to capture wind patterns..
- Assess the impact of Andes elevation on wind patterns, relative humidity, and precipitation by comparing model outputs across varying terrain heights.
- Examine the interplay between El Niño/La Niña events and Andean topography, focusing on how these interactions impact wind, humidity, and precipitation.

⁵MPAS website: <https://mpas-dev.github.io>

Chapter 2

Methodology

The Model of Prediction Across Scales (MPAS) is the result of a collaboration between the Los Alamos National Laboratory (LANL) and the National Center for Atmospheric Research (NCAR), which are research institutes in the United States. MPAS offers advanced simulation tools for studying atmospheric, oceanic, and other Earth-system interactions [17].

This section focuses on the MPAS-Atmosphere (MPAS-A) component, specifically designed for atmospheric simulations. MPAS-A, like all MPAS modules, employs an unstructured centroidal Voronoi tessellation and C-grid staggering. In this context, grid staggering refers to the arrangement of variables at different grid points, which improves numerical stability and accuracy. To grasp the underlying mechanisms of the simulations, it is necessary to explore the following concepts.

1. **Spherical Centroidal Voronoi Tessellations (SCVT):** A Voronoi diagram is a method for dividing a space into regions based on proximity to a set of points, known as generators [40]. Each region includes all points that are closer to its generator compared to any other.

Spherical Centroidal Voronoi Tessellations (SCVT) extend this concept to a spherical surface, like the Earth. Initially, generators are distributed across the sphere and then iteratively adjusted to the center of mass of their respective regions (centroidal) based on a density function. The center of mass refers to the geometric center of the region, and the density function typically represents spatial distribution factors relevant to the application, such as population density or geographical features.

The result is a set of adaptive grids with varying resolutions. These grids are finer in areas of interest, where more detail is needed, and coarser elsewhere, optimizing computational resources [41].

Figure 2.1 illustrates the SCVT applied to a spherical surface representing the Earth. The left-hand globe features a coarse grid, which is ideal for broad regional analysis, while the right-hand globe displays a finer grid, providing higher resolution for detailed local studies.

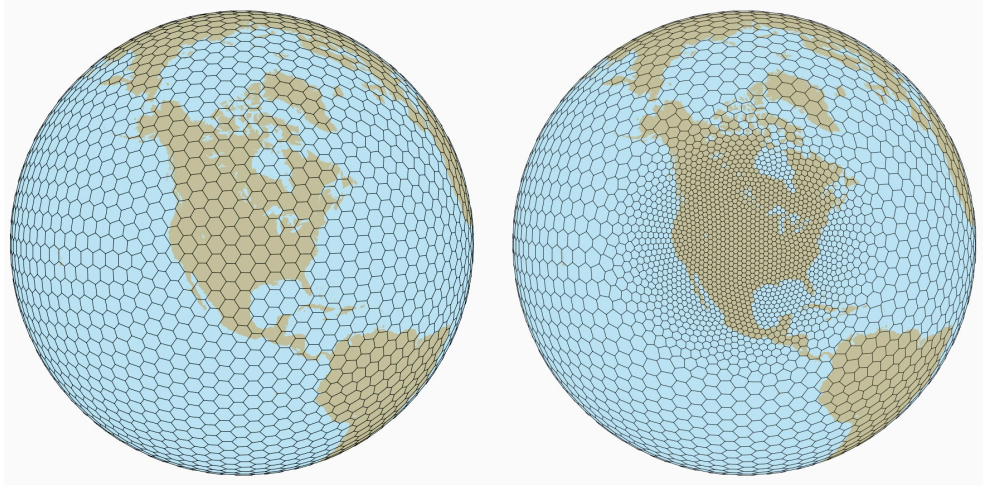


Figure 2.1: SCVT grids on a spherical surface. The left globe shows a coarse grid suitable for broad analysis, while the right globe presents a finer grid for detailed studies. Adapted from source: MPAS-Dev Atmosphere [17].

2. **C-Grid Discretization:** This technique in MPAS (Model for Prediction Across Scales) improves the stability and accuracy of atmospheric simulations by staggering key variables. Wind velocity components are positioned at the edges of grid cells, while scalar variables like pressure are placed at the center [42]. This setup minimizes errors in wave propagation and advection by allowing for more accurate flux calculations at cell boundaries [43]. By separating the locations of velocity and scalar variables, the method prevents computational issues that arise from calculating all variables in the same spot. This leads to smoother simulations and reduces artificial numerical errors, especially in complex topographical regions. Moreover, the technique supports variable resolution, providing finer grids in areas of interest while maintaining coarser grids elsewhere. This balance between accuracy and computational efficiency is crucial for modeling geophysical flows, where interactions between wind, temperature, and humidity vary greatly with topography. Thus, this approach offers a more detailed and efficient representation of atmospheric dynamics compared to uniform grid models.

2.1 Software Tools

2.1.1 Data Sources

This study employs a variety of reliable data sources to set up initial and boundary conditions, as detailed below:

- **Climate Forecast System Reanalysis (CFSR) Data:** The CFSR offers global reanalysis data with high-resolution atmospheric fields, specifically at $0.5^\circ \times 0.5^\circ$ for this research. It includes essential variables such as temperature, humidity, wind speed, and pressure across multiple vertical levels [44].

- **Climate Forecast System Version 2 (CFSv2) Data:** From April 2011 onwards, the initial conditions were set using the CFSv2 dataset, which continues from the period covered by CFSR. [45].
- **Moderate Resolution Imaging Spectroradiometer (MODIS) Data:** Provides high-resolution data for land use, vegetation fraction, albedo, and maximum snow albedo, which are key to accurately mimicking land surface properties that influence land-atmosphere interactions [46].
- **Global Multi-resolution Terrain Elevation Data 2010 (GMTED2010):** It offers detailed topographical data at multiple resolutions; allowing, in this way, to represent the elevation variations[47].

2.1.2 ENSO and date selection:

Criteria for Choosing Dates for Our Numerical Work

In selecting dates for our numerical work, we aimed to ensure that the chosen periods reflect diverse climatic conditions. We considered the following context carefully.

El Niño and La Niña represent the warm and cool phases of the El Niño Southern Oscillation (ENSO), respectively. They are characterized by significant variations in sea surface temperatures (SST) over the central and eastern zones of the tropical Pacific Ocean [48] as shown in more detail in Fig. 2.2.

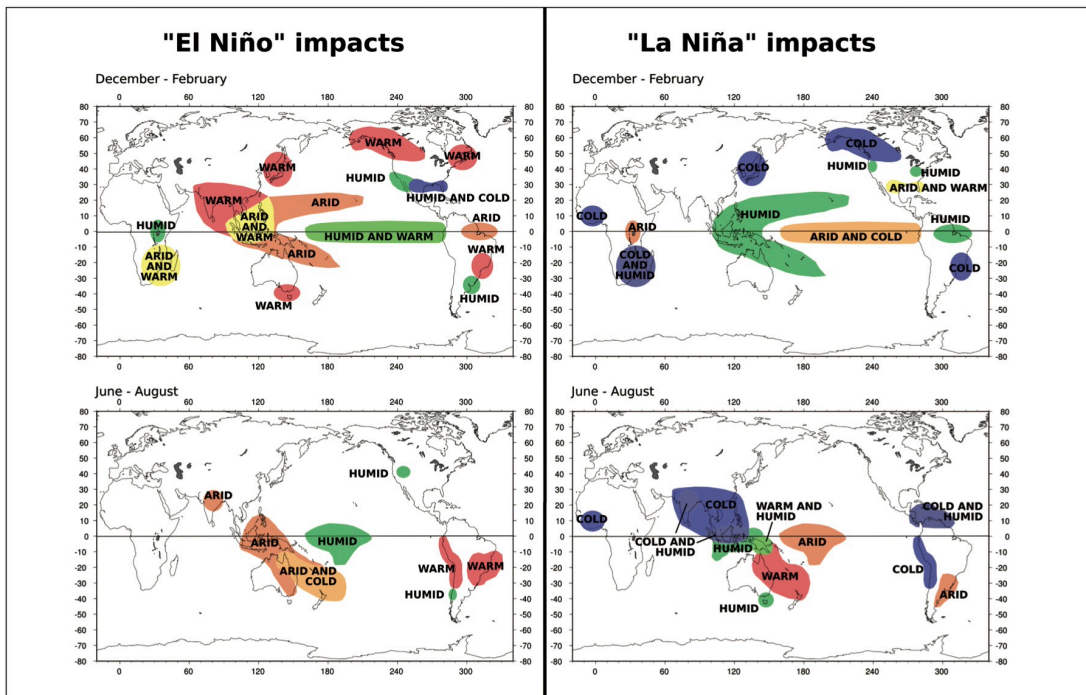


Figure 2.2: Worldwide distribution and impact of the El Niño (left) and La Niña (right) events during winter (up) and summer (bottom). Source: Giralt et al. (2007) [18].

During the El Niño phase, significantly warm SSTs lead to widespread changes in weather patterns, such as rainfall intensification across southern North America and Peru, while drought prevails in the western Pacific [49]. In contrast, La Niña is characterized by unusually cool SSTs, often resulting in opposite weather patterns to those of El Niño, including increased precipitation in the western Pacific and drier conditions in the eastern Pacific [50].

These events have a profound impact on Ecuador, even leading to negative socio-economic and environmental effects. El Niño typically causes heavy rainfall, causing major flooding, landslides, and extensive damage to infrastructure and agricultural lands. These disruptions affect local economies, particularly along the Pacific coast and low-lying areas [51]. On the other hand, La Niña usually results in drier conditions along the coastal regions, causing droughts that negatively impact water supply and agriculture. However, La Niña can also increase rainfall in the highlands and Amazon region, sometimes triggering localized flooding and landslides [9].

Classification of Strong and Weak Phenomena: This classification is based on the Oceanic Niño Index (ONI), which measures the sea surface temperature (SST) anomalies in the central and eastern equatorial Pacific.

- **Strong El Niño Events:** These are defined by ONI values greater than or equal to $+1.5^{\circ}\text{C}$. These events typically lead to intense rainfall and significant temperature anomalies, causing severe inundations, especially in the coastal plains of southern Ecuador [52].
- **Moderate El Niño Events:** These are events characterized by ONI values between $+1.0^{\circ}\text{C}$ and $+1.4^{\circ}\text{C}$, including above-average rainfall and warmer temperatures, but with less intensity than strong El Niño events [53].
- **Weak El Niño Events:** The ONI values are between $+0.5^{\circ}\text{C}$ and $+0.9^{\circ}\text{C}$ [53]. These events typically produce less intense weather changes than strong El Niño conditions.
- **Strong La Niña Events:** The ONI values are less or equal to -1.5°C and often result in substantial climatic shifts, encompassing reduced rainfall and cooler temperatures [54].
- **Moderate La Niña Events:** These are events characterized by ONI values between -1.0°C and -1.4°C [53], including below-average rainfall and cooler temperatures, but with less intensity than strong La Niña events.
- **Weak La Niña Events:** The ONI values are between -0.5°C and -0.9°C . The impacts are less pronounced than those of strong La Niña events but can still influence local and regional climates.

Criteria for Date Selection The selected dates serve as inputs for the numerical models presented later in this thesis. By using these specific periods, the models can simulate and analyze atmospheric conditions under a spectrum of climatic scenarios, thereby providing insights into the impacts of El Niño and La Niña events on Ecuador's climate.

- **Historical Climatic Data:** We referred to historical climatic records and datasets, such as those of the National Oceanic and Atmospheric Administration (NOAA) and the Climate Prediction Center (CPC), to identify periods when significant El Niño and La Niña events occurred [55, 56, 57].
- **Availability of High-Quality Data:** Dates were selected to ensure the availability of high-resolution atmospheric and surface data from various sources such as the Climate Forecast System Reanalysis (CFSR) and Climate Forecast System Version 2 (CFSv2) datasets[58].
- **Representation of Climatic Variability:** Key periods were chosen to capture various climatic scenarios, including strong and weak El Niño and La Niña events. [55].
- **Local Reports and Impacts:** Local reports and newspaper articles documenting floods, heavy rains, and additional climatic impacts were reviewed, ensuring the dates chosen reflect the real-world conditions experienced in Ecuador.

| Phenomenon | Strength | Dates | ONI Value |
|------------|----------|----------------------|-----------|
| El Niño | Strong | March 23-25, 1983 | 2.0°C |
| | | February 18-20, 1998 | 2.3°C |
| | | February 12-14, 2016 | 2.1°C |
| | Weak | October 5-7, 2004 | 0.7°C |
| | | February 15-17, 2007 | 0.6°C |
| | | January 10-12, 2010 | 0.8°C |
| La Niña | Strong | January 12-14, 1989 | -1.7°C |
| | | November 5-7, 1998 | -1.8°C |
| | | January 10-12, 2011 | -1.6°C |
| | Weak | October 5-7, 1984 | -0.9°C |
| | | December 10-12, 1995 | -0.7°C |
| | | January 15-17, 2001 | -0.8°C |

Table 2.1: Key Periods of El Niño and La Niña Phenomena with ONI Values[5, 6, 7, 8, 9, 10, 11, 12, 13, 14, 15]

The dates are summarized in Table 2.1, providing a clear overview of the periods for El Niño and La Niña phenomena along with their respective ONI values. These values are calculated by comparing current SSTs to a 30-year average of SSTs for the same region and time (currently 1991-2020). Positive anomalies, indicating El Niño conditions, occur when SSTs exceed the 30-year average by significant margins. Conversely, negative anomalies, indicating La Niña conditions, reflect SSTs significantly below the baseline [11].

2.1.3 Preprocessing Tools

To prepare raw data for analysis and ensure compatibility with the simulation model, we employed the following tools:

- **Weather Research and Forecasting (WRF) Pre-processing System (WPS):** This component of the WRF model plays a pivotal role in this phase by preparing both geographic and meteorological data to ensure it is compatible with the MPAS-A. WPS consists of three main components:
 - **Geogrid Program:** This generates static geographic fields required by MPAS-A [59], such as terrain height, land use categories, and soil types (independent of any meteorological data). Its output is in NetCDF format.
 - **Ungrib Program:** This extracts meteorological data (atmospheric variables like wind speed, temperature, and humidity) from GRIB1 or GRIB2 files and converts them into an intermediate format suitable for further processing [59].
 - **Metgrid Program:** It takes the intermediate files created by Ungrib, as well as the NetCDF files from Geogrid, and horizontally interpolates the meteorological data onto the MPAS-A model grid [59].
- **NetCDF (Network Common Data Form) Utilities:** These utilities are useful in manipulating and converting data formats between different stages of preprocessing. NetCDF Operators (NCO) [60] and Climate Data Operators (CDO) [61]. Operations such as slicing, dicing, and aggregating netCDF data help with the compatibility and preparation of input files.

2.1.4 Data Transformation and Integration:

- **Extraction of Atmospheric Variables:** The first step is to extract the atmospheric variables (temperature, pressure, humidity, and wind fields) from the raw data files using the ungrib tool. [62].
- **Intermediate File Creation:** Once the atmospheric variables are extracted, they are stored in intermediate files, and formatted to facilitate the consequent steps of horizontal interpolation and integration. [62].
- **Horizontal Interpolation and Integration:** The Metgrid tool conducts the interpolation, adjusting the spatial resolution and projecting the atmospheric data used by MPAS. Sophisticated interpolation algorithms fill in data points across the model grid, ensuring that all necessary atmospheric variables are accurately represented at each grid point [62].
- **Finalization of Initial Condition Files:** The final step of the data transformation process is the creation of initial condition files in a format readable by the MPAS-Atmosphere model to initialize the model simulations. [62].

2.2 Simulation

2.2.1 Model Components

MPAS-A consists of two primary components: the model for simulating dynamics and physics of the atmosphere, and the initialization component that prepares initial conditions and updates for sea-surface temperature, sea ice, and boundary conditions. Both components function as cores within the MPAS framework, sharing a common driver program and infrastructure, yet each is compiled as a separate executable [19].

The MPAS framework is organized into different sections to facilitate efficient simulations (Figure 2.3). The MPAS Superstructure serves as the top-level coordinator, overseeing interactions among the model’s components. Complementing this, the MPAS Common Infrastructure provides shared resources like data handling and grid configuration. Within this arrangement, the `init_atmosphere` module establishes all necessary initial states, such as atmospheric and land conditions, sea-surface temperature, and ice levels, preparing the model for an accurate simulation start [19]. The atmosphere module then conducts the core calculations, simulating atmospheric dynamics and physical processes based on the initialization data.

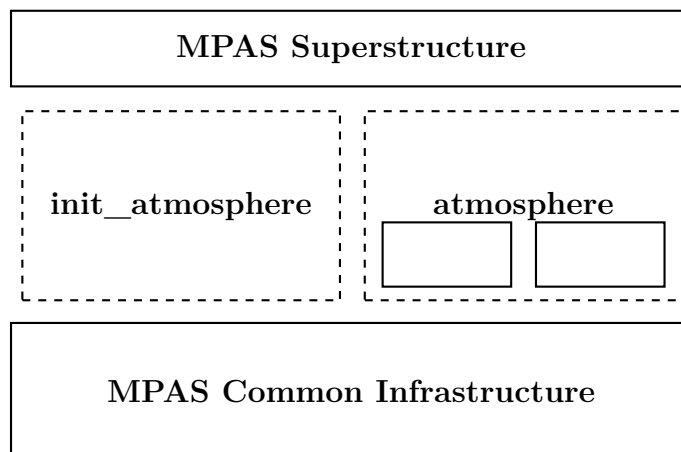


Figure 2.3: Schematic structure of the MPAS-A model components. The MPAS Superstructure includes separate initialization (`init_atmosphere`) and simulation (`atmosphere`) modules, built on the common infrastructure. Figure reproduced from MPAS-Atmosphere Model User’s Guide: Version 8.1.0 [19].

2.2.2 Model Parametrization Schemes

For this study, we employed the ‘convection-permitting’ physics suite, recommended for the 3 km mesh used in our research. This suite is designed for high-resolution models, allowing for the explicit resolution of both hydrostatic and non-hydrostatic convection processes. [19]. Table 2.2 provides a summary of the schemes included in our numerical simulations, and we briefly explain them below:

Table 2.2: The parameterization schemes featured in the ‘convection-permitting’ physics suite.

| Parameterization | Scheme |
|--------------------------------|---------------------------|
| Convection | Grell-Freitas |
| Microphysics | Thompson et al. scheme |
| Longwave Radiation | RRTMG |
| Shortwave Radiation | RRTMG |
| Land Surface | Noah-MP |
| Boundary Layer | MYNN |
| Surface Layer | Revised MM5 Monin-Obukhov |
| Cloud fraction for radiation | Xu-Randall |
| Gravity wave drag by orography | YSU |

- The Grell-Freitas scheme is applied to simulate convection. Its scale-aware design allows adaptation to various grid resolutions, enhancing the quality of simulations [19].
- Microphysical processes, including cloud formation and precipitation were managed using the Thompson et al. method [63] [64].
- For simulating radiative transfer, the Rapid Radiative Transfer Model for Global Circulation Models (RRTMG) was used for both longwave and shortwave radiation. The longwave component models terrestrial infrared radiation, and the shortwave component handles solar radiation [65].
- The Noah-Multiparameterization (Noah-MP), a land surface model, improves the simulation of land-atmosphere interactions by providing multiple parameterization options for various physical processes, including soil moisture and temperature, vegetation processes, snowpack dynamics, and surface runoff [66].
- The Mellor-Yamada-Nakanishi-Niino (MYNN) Level 2.5 [67] turbulence parametrization is implemented to represent the boundary layer dynamics. The boundary layer is the lowest part of the atmosphere, directly influenced by the Earth’s surface, where friction, turbulence, and mixing occur in response to surface forcings. This parametrization significantly impacts cloud formation, heat exchange, and momentum transfer near the Earth’s surface, thereby playing a main role in accurately simulating atmospheric processes.
- Surface layer processes were represented using the revised MM5 Monin-Obukhov scheme [68]. This approach refines the handling of vertical profiles of wind, temperature, and humidity, along with fluxes of momentum, heat, and moisture near the surface, which is crucial for simulating the entire boundary layer.
- To determine cloud fraction for radiation calculations, we employed the Xu-Randall method [69]. This scheme calculates the fraction of a grid cell covered by clouds based on various atmospheric conditions.

- Gravity wave drag by orography was represented using the Yonsei University (YSU) [70] scheme to simulate the effects of gravity wave drag caused by orographic features.

2.2.3 Initial and Boundary Conditions

Geographical Domain and Mesh Configuration

To capture the essential geographical features of Ecuador and the Andes region, we generated static geographical data (see Fig.2.4). We defined an elliptical domain centered at latitude -1.75 and longitude -77.2, a semi-major axis of 1,264,000 meters, a semi-minor axis of 800,000 meters, and an orientation angle of 45 degrees.

Vertical Grid and Terrain-Following Configuration

The vertical grid of our simulations is configured with 55 levels, extending up to 30 kilometers in altitude. This configuration allows for the representation of processes occurring at both near-surface and higher altitudes. The minimum vertical grid spacing of 0.3 meters captures fine-scale details near the surface. Additionally, the model uses a terrain-following grid that aligns vertical levels with the underlying topography, reducing numerical errors that may arise from sudden changes in altitude.

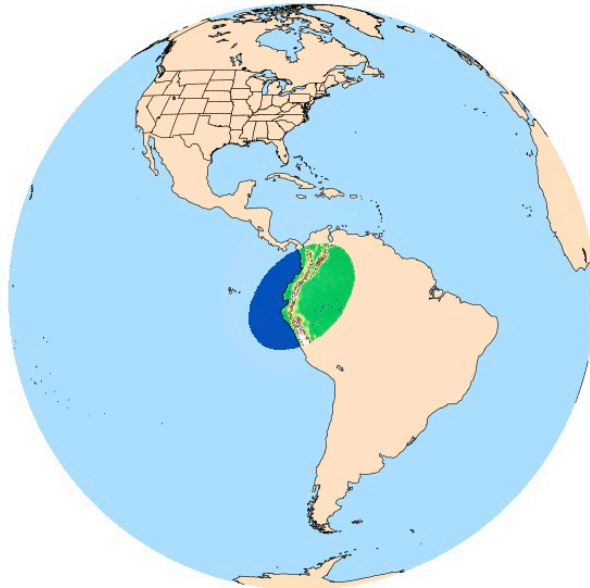


Figure 2.4: Static geographical data for Ecuador used in the climatological simulations. The elliptical region centered over Ecuador includes its coastal plains, the Andean highlands, and the Amazon rainforest, ensuring comprehensive coverage of the area's diverse topography for accurate atmospheric modeling.

- **Initial Conditions:**

- **Configuration:** The initial atmospheric state was set using the CFSR PGBH (Pressure on Gaussian Grid) / CFSv2 dataset. Initially, the model initialization case was set to 7 and later updated to 9, generating static fields and subsequently initializing the atmospheric conditions dynamically. Temporal parameters are specified to ensure the timeline of the model aligns with the input data, accurately reflecting the atmospheric state for the designated period and forming a reliable baseline for the simulation. We employ a second-order time integration method with a short timestep of 18 seconds for capturing rapid changes and small-scale phenomena, such as local wind patterns and turbulence.
- **Boundary Conditions:**
 - **Configuration:** The data were acquired from the CFSR, which updates every six hours. The frequent updating allows the model to effectively capture the evolving weather patterns. Additionally, the incorporation of surface conditions such as sea surface temperature (SST) and land surface data, enhances the simulation of interactions at the land-sea interface.

2.2.4 Governing Equations

The MPAS model relies on a set of fundamental equations to simulate atmospheric dynamics accurately. These equations include the continuity equation (which is a mass conservation equation), momentum conservation equations, thermodynamic energy equation, moisture conservation equation, and the ideal gas law, which closes the system of hyperbolic partial differential equations. These equations are initialized with observational data and reanalysis datasets to ensure accurate starting conditions and are iteratively solved throughout the simulation.

The continuity equation ensures mass conservation across the grid:

$$\frac{\partial \rho}{\partial t} + \nabla \cdot (\rho u) = 0 \quad (2.1)$$

This equation (2.1) updates air density (ρ), maintaining the critical balance of mass as the model evolves [19]. It tracks mass transport across the atmospheric grid, ensuring that the total mass remains constant over time. This is crucial for realistic simulations of atmospheric processes, as any mass imbalance could lead to significant errors in weather prediction. MPAS divides the atmosphere into a 3D grid of cells, calculating and updating the mass of each cell at every time step. The movement of air mass between cells is meticulously tracked to ensure mass conservation across the entire grid. Boundary conditions, updated every six hours, further ensure that incoming and outgoing mass at the edges of the model are accurately represented.

The momentum equations determine wind velocity (u) while accounting for pressure gradients, gravitational forces, Coriolis effects, and frictional forces:

$$\frac{\partial u}{\partial t} + (u \cdot \nabla)u = -\frac{1}{\rho} \nabla p + g + F \quad (2.2)$$

These equations (2.2) capture the dynamic nature of atmospheric motion, influencing

how wind patterns develop and change [19]. The terms include the pressure gradient force, which drives wind from high to low-pressure areas; gravitational force, influencing vertical motion; Coriolis force, affecting wind direction due to the Earth’s rotation; and frictional force, which influences wind near the surface, reducing speed and altering its direction. In MPAS, wind velocities are calculated at each cell face using the staggered grid arrangement (C-grid). The model computes the net force on each air parcel, updating velocities accordingly and separately handling vertical and horizontal components to ensure accurate simulation of wind patterns influenced by topographical features like the Andes.

Temperature variations within the atmosphere are tracked through the thermodynamic energy equation, focusing on potential temperature (θ):

$$\frac{\partial \theta}{\partial t} + u \cdot \nabla \theta = Q_\theta \quad (2.3)$$

This equation (2.3) incorporates advection (transport by wind) and diabatic heating sources (such as radiation and latent heat release). The term Q_θ represents heat sources and sinks. This equation is vital for understanding temperature distribution and evolution, affecting weather patterns and phenomena like convection and cloud formation [19]. In MPAS, the temperature of each cell is updated based on advection and local heating or cooling, with heat transported horizontally and vertically influenced by wind patterns. This equation also accounts for latent heat from processes like condensation and evaporation, which are crucial for simulating cloud formation and dissipation.

The moisture conservation equation manages water vapor content (q_v), simulating processes such as evaporation, condensation, and advection:

$$\frac{\partial q_v}{\partial t} + u \cdot \nabla q_v = Q_{q_v} \quad (2.4)$$

This equation (2.4) is crucial for predicting humidity and precipitation [19]. The term Q_{q_v} includes sources and sinks of moisture, such as condensation (releasing latent heat) and evaporation (absorbing heat). In MPAS, water vapor content in each cell is updated based on local sources/sinks and advection. This equation helps simulate the conditions under which water vapor condenses into clouds and tracks the formation and fallout of precipitation, essential for accurate weather forecasting.

The equation of state, or ideal gas law, ensures consistency between pressure (p), density (ρ), and temperature (T):

$$p = \rho R_d T \quad (2.5)$$

where R_d is the specific gas constant for dry air. This equation (2.5) maintains the fundamental relationship between these critical atmospheric variables, ensuring that the simulated atmospheric conditions remain physically realistic [19]. In MPAS, the pressure in each cell is recalculated every time step to reflect changes in temperature and density, ensuring all other equations work harmoniously to maintain realistic physical conditions. This equation is applied consistently at the boundaries to maintain accurate pressure conditions throughout the model.

In each time step, these equations are solved iteratively using numerical methods optimized for the grid structure of the model. The MPAS model utilizes advanced techniques

to discretize equations mentioned on the spherical centroidal Voronoi tessellation grid, allowing for adaptive resolution and enhancing computational efficiency. The simulation starts with initial conditions derived from ECMWF reanalysis data, which provides realistic starting values for all variables. The governing equations are solved at each time step, updating variables to reflect the latest state of the atmosphere. This process includes managing boundary conditions and external influences. The model generates output data every hour that is later analyzed. This structured approach allows MPAS-A to accurately simulate the complex and dynamic behavior of the Earth's atmosphere, providing valuable insights for weather prediction and climate research.

2.3 Hardware

The simulations were performed using two advanced high-performance computing clusters: the HPC cluster at CEDIA (Corporación Ecuatoriana para el Desarrollo de la Investigación y la Academia)¹ and another multi-CPU HPC facility. These computing resources supplied the necessary computational power to handle large-scale and complex simulations. The specific configuration of the HPC system used in this investigation is as follows:

2.3.1 HPC Configuration

- **Nodes and Cores:** The simulations used 64 compute nodes, each equipped with 48 cores, giving a total of 3,072 cores. This configuration enabled parallel processing, substantially reducing the time required for simulations.
- **Memory:** Each node was allocated 48 GB of RAM, essential for managing the large datasets and intricate calculations involved in the simulations. This substantial memory provision ensured the model could process data efficiently without bottlenecks or slowdowns due to insufficient resources.
- **Disk Space:** Sufficient disk space was allocated to store the input data, simulation outputs, and intermediate files generated during the simulation runs. The pre-simulation and post-simulation data were transferred between different HPC centers via SSH-based protocols, such as SCP.
- **Multi-Core CPUs:** The simulations leveraged multi-core CPUs to parallelize computations, using the MPI library and significantly reducing the time required to run high-resolution models.
- **Simulation Time:** Model initialization and boundary condition setup took about 30 minutes, while the main run was set for 45 minutes but could extend to several hours depending on complexity. Efficient HPC resource management ensured timely completion.

¹CEDIA website: <https://cedia.edu.ec>

2.4 Specific Scenarios and Numerical Experiments

To study the influence of the Andes mountains on the atmospheric dynamics over Ecuador (in particular, winds), we conducted simulations under four different scenarios of mountain heights: the actual height, half the height, 10% of the height, and 1% of the height as seen in Table 2.3 and Figure 2.5.

Table 2.3: Topographic Scenarios for Wind Pattern Simulations

| Experiment | Topographic Adjustment |
|-------------|---|
| Full Height | Actual terrain elevation |
| Half | Terrain reduced to 50% of original height |
| 10% | Terrain reduced to 10% of original height |
| 1% | Terrain reduced to 1% of original height |

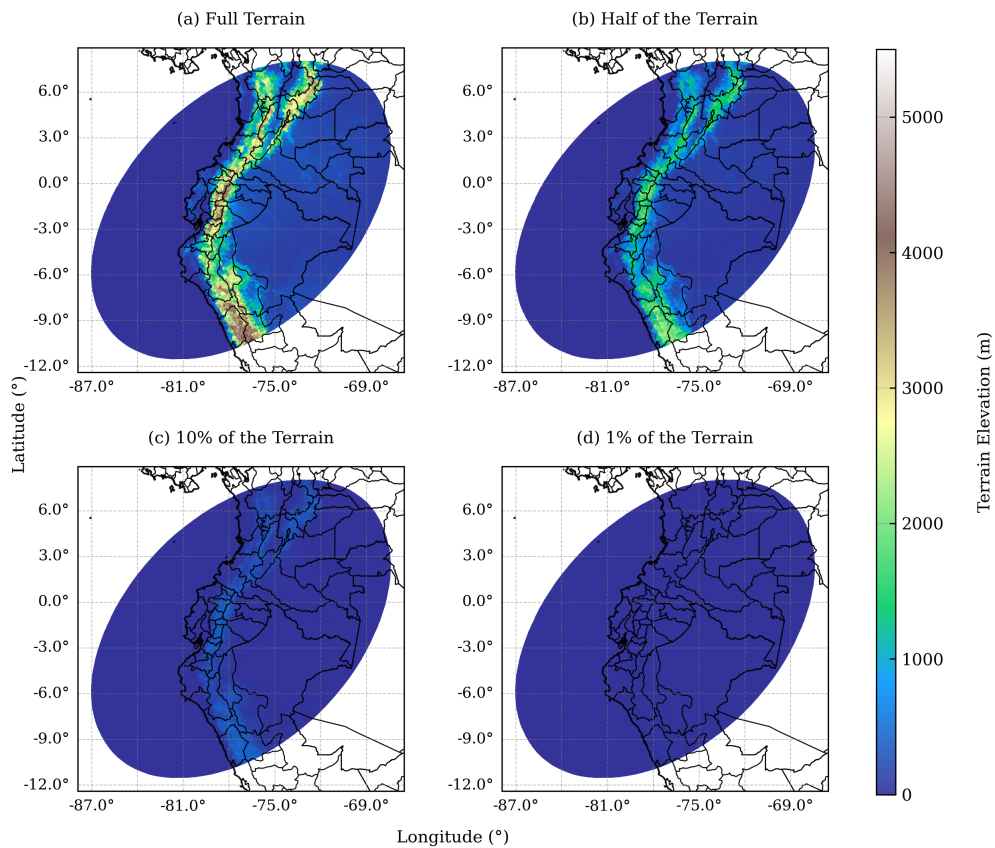


Figure 2.5: Terrain Elevations for the Analysis: This figure shows the terrain elevation at different data resolutions: (a) Full, (b) Half, (c) 10%, and (d) 1% of the terrain. The color bar indicates elevation from 0 to over 5000 meters.

Chapter 3

Results and Discussion

This section presents the findings from our analysis of the regional wind patterns and atmospheric conditions over continental Ecuador, particularly emphasizing the influence of the Ecuadorian Andes. Using the MPAS code, we examine wind behavior under various scenarios, including the presence of the Andes, different terrain elevations, and the impacts of them on El Niño and La Niña events. The results are discussed through descriptive and interpretative analyses of 2D wind maps, relative humidity and precipitation differences, highlighting the critical role of topography and climatic phenomena in shaping regional atmospheric dynamics.

3.1 Regional Wind Patterns

In this section, we separate our analysis by date. For clarity, we show the individual results for each selected date (see Table 2.1) and then discuss the overall effects. Observations were recorded at 15:00 UTC for three consecutive days, focusing on zonal (i.e., in the west-east direction) and meridional (i.e., in the north-south direction) wind components and wind speed at the 850 hPa pressure level (1.5 kilometers above sea level). This altitude is ideal for examining significant atmospheric processes affected by topography while minimizing the influence of surface friction.

3.1.1 Wind Component Analysis

The wind patterns over Ecuador are illustrated in a 3x3 grid. Each row represents a different day, while each column displays the U -zonal wind, the V -meridional wind, and the wind vectors.

March 1983

On March 23, the U -zonal winds over Ecuador range from approximately 10 m/s (westward) to -10 m/s (eastward). Eastward winds are more prominent in the northern regions, while stronger westward winds are observed in the south. This pattern remains consistent

on March 24, though with slightly diminished intensity; the strongest winds are still located near the coast but extend further inland. By March 25, the zonal wind direction shifts, with northern Ecuador experiencing westward winds and southern regions showing eastward winds. The V -meridional wind maps reveal values ranging from ~ -10 m/s (southward) to ~ 10 m/s (northward). Coastal areas experience strong northward winds, while inland regions display a mix of both northward and southward flows. On March 24, meridional winds strengthen, particularly in eastern Ecuador. The strong meridional flows continue on March 25, dispersing across the country. The third column features wind vector plots that combine the effects of both zonal and meridional components, illustrating wind speeds from 0 to ~ 18 m/s over the three days. High-speed winds (>10 m/s) are concentrated along the Andes and coastal regions, with wind direction indicating convergence over the Andes, resulting in complex patterns significantly influenced by topography (Figure 3.1).

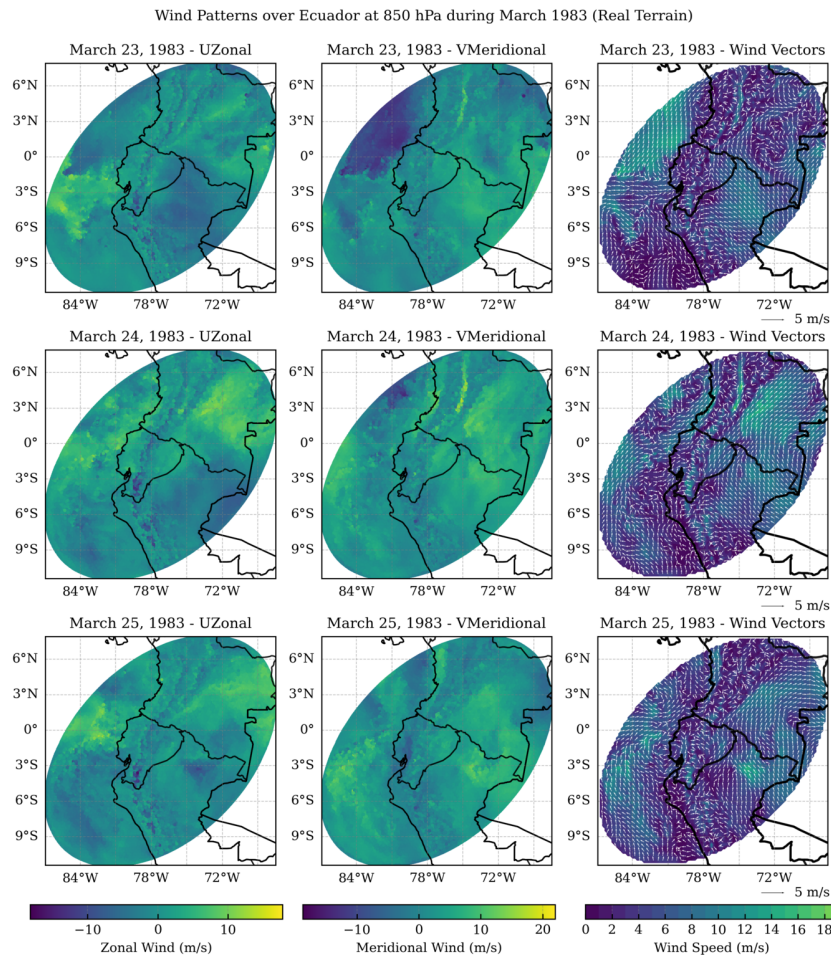
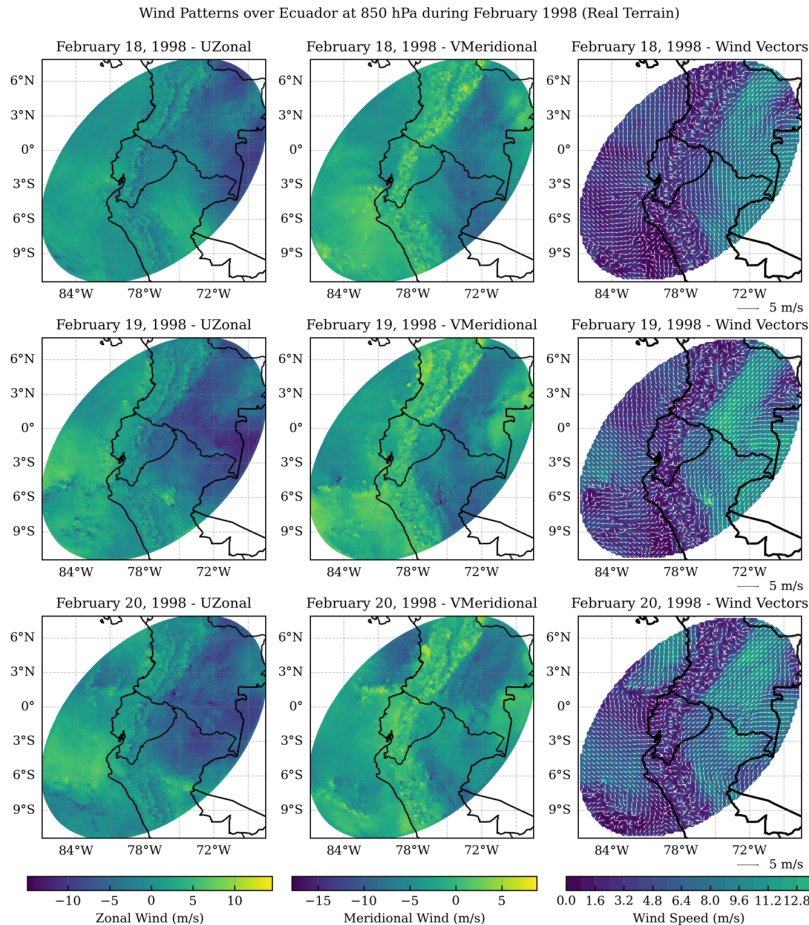


Figure 3.1: Wind patterns at 850 hPa over Ecuador in March 1983 (Real Terrain), showing variability influenced by the Andes. White arrows indicate wind direction, with length corresponding to 5 m/s.

February 1998

On February 18, the U -zonal wind component exhibits velocities ranging from approximately -10 m/s to 10 m/s. Eastward winds dominate the northern and central regions of Ecuador, while weaker westward winds are observed in the south. This pattern persists on February 19 and 20, with consistent eastward winds in the north and central areas, alongside noticeable westward winds in the south, maintaining similar velocity ranges. The V -meridional wind on February 18 ranges from ~ -10 m/s (southward) to ~ 10 m/s (northward), with strong northward winds along the coast and southward winds in the interior, indicating complex airflow likely influenced by topography. On February 19, strong northward winds continue along the coast, while on February 20, eastward winds are predominant in the north and stronger westward winds are present in the south, reflecting some consistency with earlier observations. Wind speeds generally range from 0 to ~ 12.8 m/s, with high-speed winds concentrated along the Andes and coastal areas. The wind vectors reveal significant deflections and accelerations due to the terrain, highlighting complex convergence patterns over the Andes throughout the three days (Figure 3.2).



February 2016

The zonal wind ranges from approximately -15 m/s (westward) to 10 m/s (eastward). The north regions show strong eastward winds, and the south region exhibits weak westward winds. By February 13, the pattern of zonal winds becomes more defined, with prominent eastward winds in the north and center, while weaker westward winds are observed in the south. On February 14, the zonal wind continues to show this variation. Regarding the V -meridional wind, values range from ~ -10 m/s (southward) to $\sim +10$ m/s (northward). On February 12, coastal areas show strong northward winds and the interior regions exhibit a mix of northward and southward flows. This becomes more pronounced on February 13 and by February 14, the patterns further intensify, showing a dominant south-to-north flow throughout the coastal areas and alternating northward and southward flows in the interior region. Wind speeds range from 0 to ~ 14.4 m/s. On February 12, the wind vectors reveal complex interactions with varying wind speeds across Ecuador. By February 13 and 14, the wind vectors display more organized patterns. High-speed winds (up to ~ 14.4 m/s) are concentrated along the Andes and coastal regions indicating significant terrain-induced deflections and accelerations (Figure 3.3).

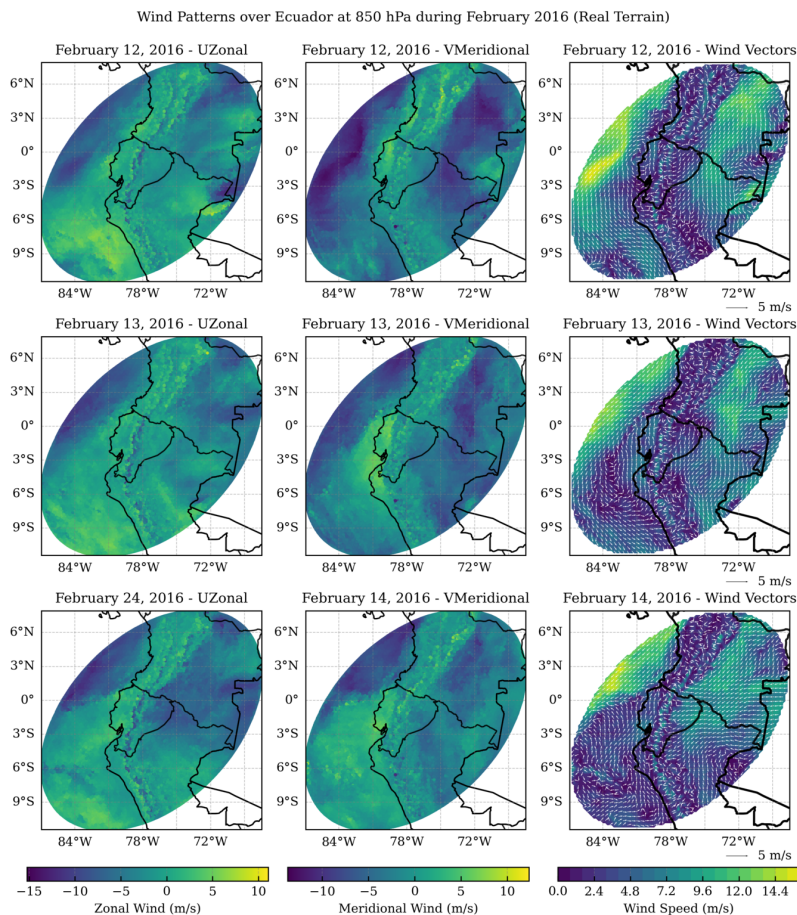
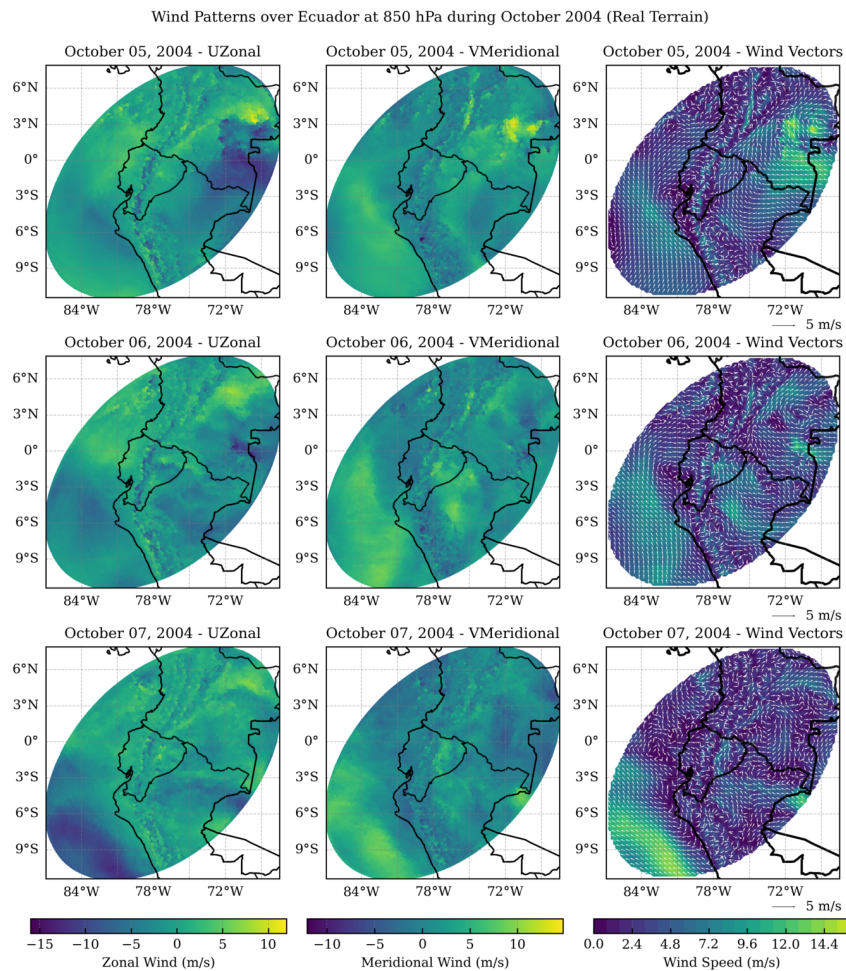


Figure 3.3: Wind patterns at 850 hPa over Ecuador in February 2016 (Real Terrain), highlighting complex wind deflections due to the Andes. White arrows indicate wind direction, with length corresponding to 5 m/s.

October 2004

Zonal wind ranges from ~ -15 m/s (westward) to $\sim +10$ m/s (eastward). On October 5, strong eastward winds are visible in the northern regions. On October 6, Eastward winds dominate northern and central Ecuador, while westward are present in the south. By October 7, the zonal wind patterns remain similar, but become more defined. Meridional wind ranges from ~ -10 m/s (southward) to $\sim +10$ m/s (northward). On October 5 there is a predominantly south-to-north flow across Ecuador, particularly in the central and northern regions. This south-to-north trend intensifies on October 6 and on October 7, the meridional wind continued to show a strong south-to-north component, particularly in the north and central regions, suggesting the influence of large-scale atmospheric circulation associated with the El Niño event. Wind speeds range from 0 to ~ 14.4 m/s. On October 5, reveal complex wind patterns with varying speeds, particularly high in the north and center. By October 6, the wind vectors displayed more organized and stronger wind flow, and on October 7 there is a more turbulent wind flow pattern (Figure 3.4).



February 2007

The zonal wind over Ecuador ranges from approximately -15 m/s (westward) to +10 m/s (eastward). The regions in the north show stronger eastward winds, while the southern parts exhibit weaker westward winds. This pattern is observed over the three days. The meridional wind values range from ~ -20 m/s (southward) to $\sim +10$ m/s (northward). Coastal areas show strong northward winds, while the inland regions exhibit a mix of northward and southward flows. Again, the pattern prevails over the three days. Wind speeds range from 0 to ~ 21 m/s. The plots show that high-speed winds are concentrated along the Amazon basin and complex convergence patterns over the Andes (Figure 3.5).

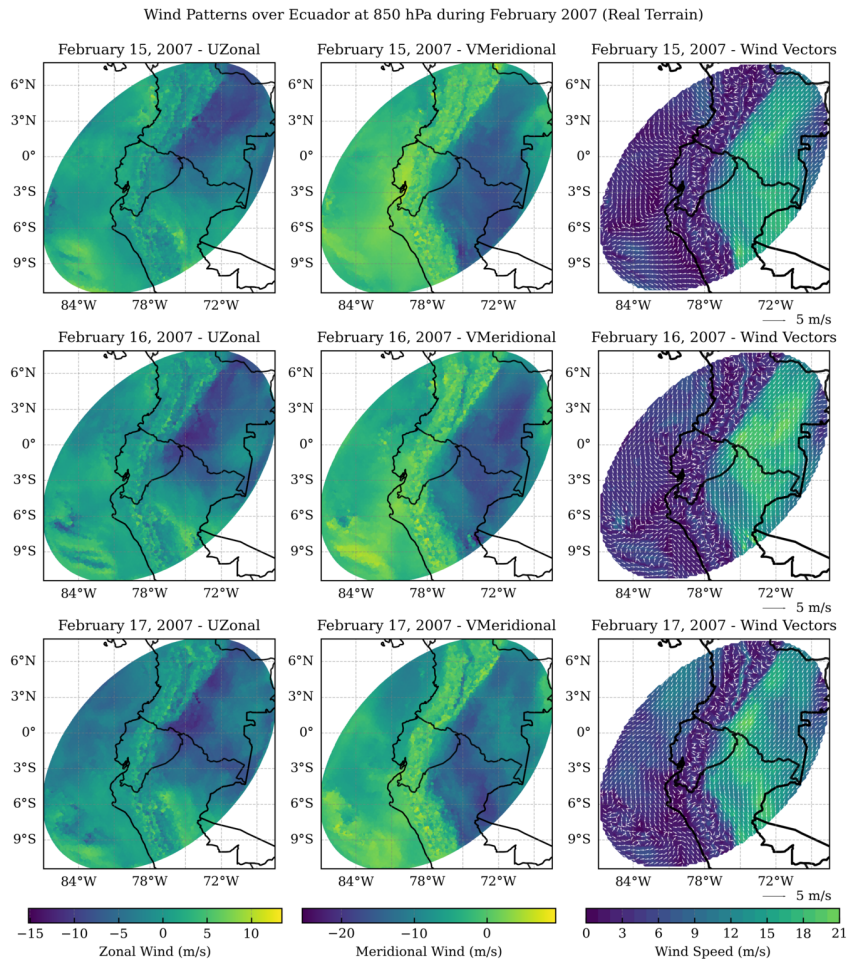


Figure 3.5: Wind patterns at 850 hPa over Ecuador in February 2007 (Real Terrain), showing significant wind variability due to the Andes. White arrows indicate wind direction (5 m/s reference), with speeds up to ~ 21 m/s and complex convergence and divergence patterns.

January 2010

The zonal wind over Ecuador ranges from approximately -10 m/s (westward) to +15 m/s (eastward). On January 10, there are predominantly westward winds in southern Ecuador

and eastward winds in the northern regions. This pattern is consistent on January 11 and 12, maintaining similar velocity ranges. Meridional wind values range from ~ -20 m/s (southward) to $\sim +10$ m/s (northward). The plots show a mix of northward and southward flows in the interior region and strong northward winds in the coastal region. Wind speeds range from 0 to ~ 16.8 m/s. High-speed winds are located along the Amazon basin and the Andes mountains show complex convergence zones (Figure 3.6).

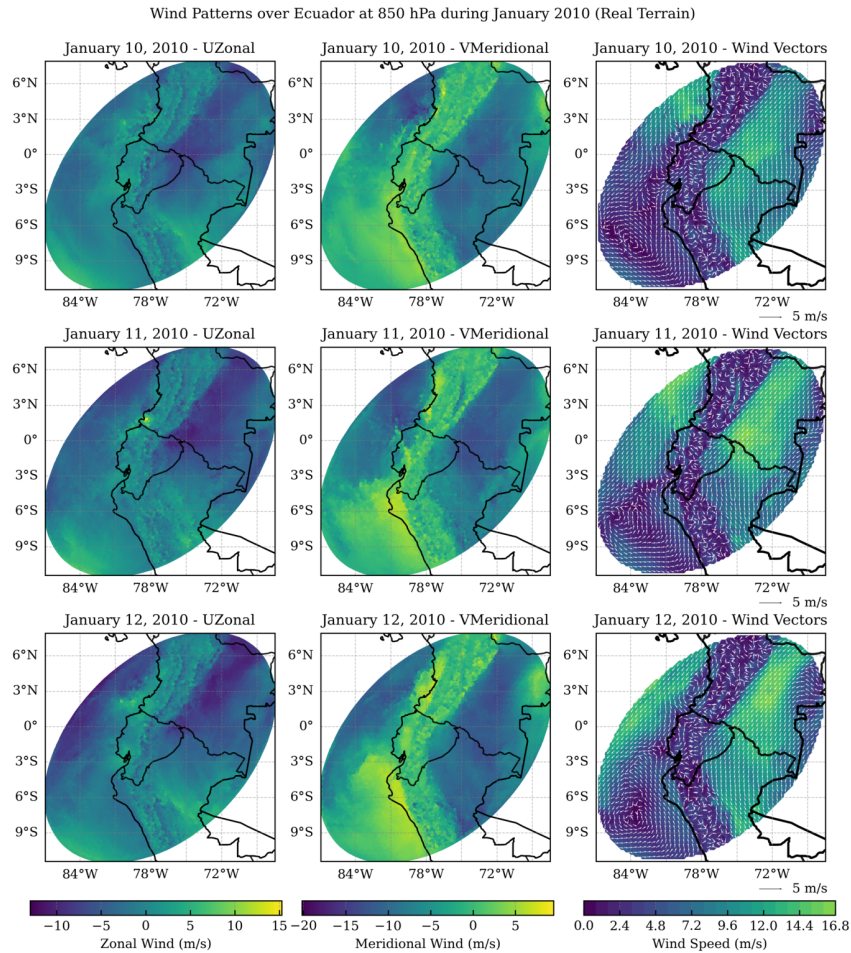


Figure 3.6: Wind patterns at 850 hPa over Ecuador in January 2010 (Real Terrain), showing complex convergence and divergence. White arrows indicate wind direction (5 m/s reference), with speeds up to ~ 16.8 m/s.

January, 1989

Zonal wind ranges from approximately -10 m/s (westward) to $+10$ m/s (eastward). On January 12, central and northern regions of Ecuador show stronger eastward winds, and southern regions exhibit weaker westward winds. This pattern persists on January 13 and 14, but the intensity slightly diminishes across the region. Meridional wind values range from ~ -10 m/s (southward) to $\sim +10$ m/s (northward). We find again strong northward winds along the coast, with southward winds in the interior regions, persistent over the days. Wind speeds range from 0 to ~ 12.8 m/s. Zones of high speed winds are concentrated

along the Amazon basin and the Andes. It is also clear directional changes and divergence zones are influenced by the Andes (Figure 3.7).

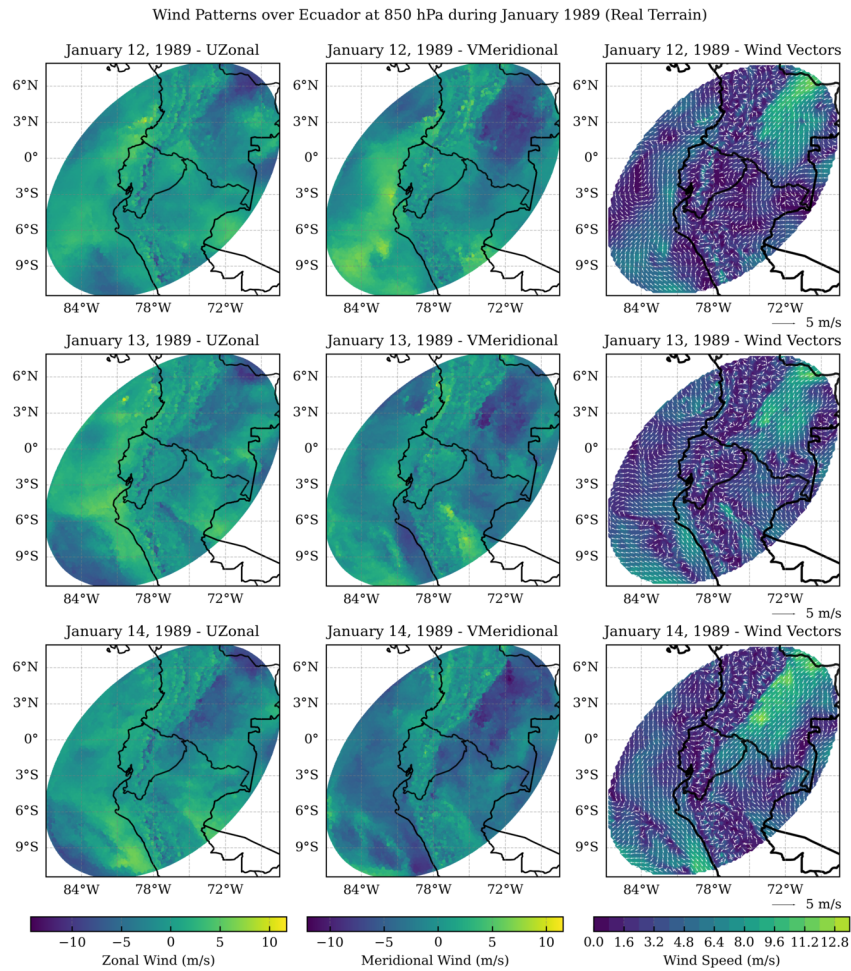
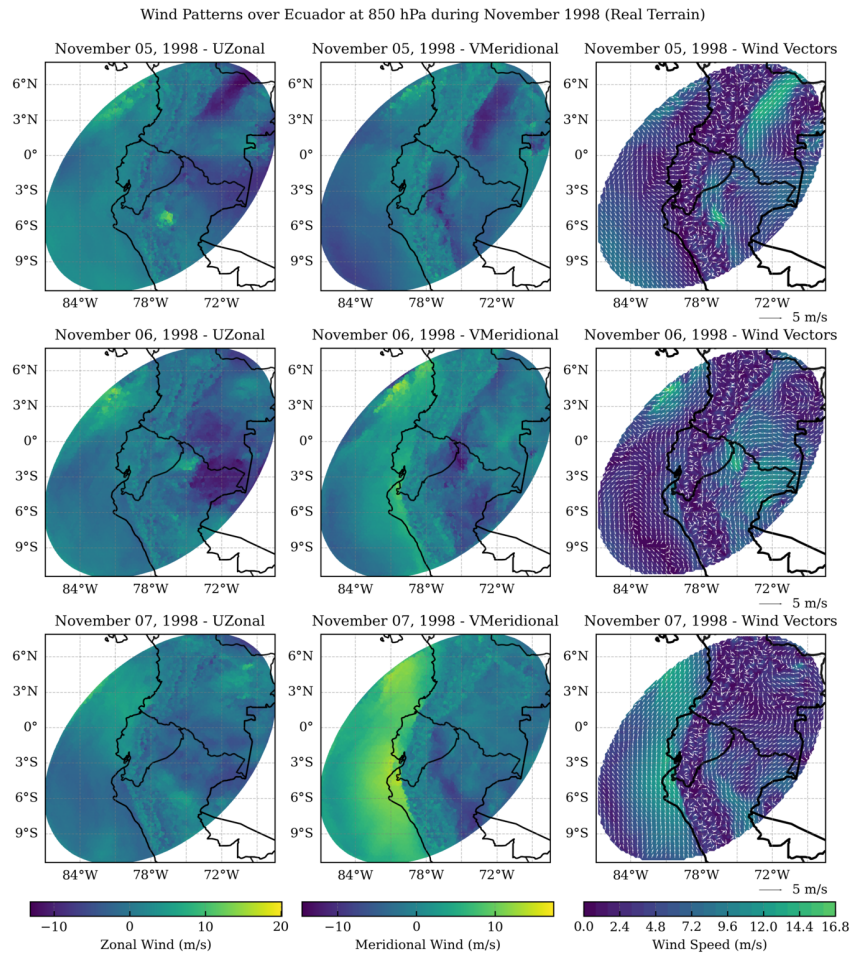


Figure 3.7: Wind patterns at 850 hPa over Ecuador in January 1989 (Real Terrain), showing complex convergence and divergence. White arrows indicate wind direction (5 m/s reference), with speeds up to ~ 12.8 m/s.

November, 1998

The wind patterns for November 1998 are shown in Figure 3.8. Zonal wind ranges from approximately -10 m/s (westward) to +20 m/s (eastward). The U-zonal wind component exhibits strong eastward winds, particularly along the coastal regions over the three days. Meridional wind values range from ~ -10 m/s (southward) to $\sim +15$ m/s (northward). On November 5 shows strong northward winds, particularly along the coast and eastern parts of the Andes. On November 6, strong northward winds continue along the eastern side, with notable southward winds along the Andes, and on November 7, northward winds intensify in the coastal regions. Wind speeds remain between 0 and ~ 16.8 m/s. The vectors reveal intricate wind patterns, directional changes over the Andes zone, and high wind speeds along the amazon region and some parts of the mountains.



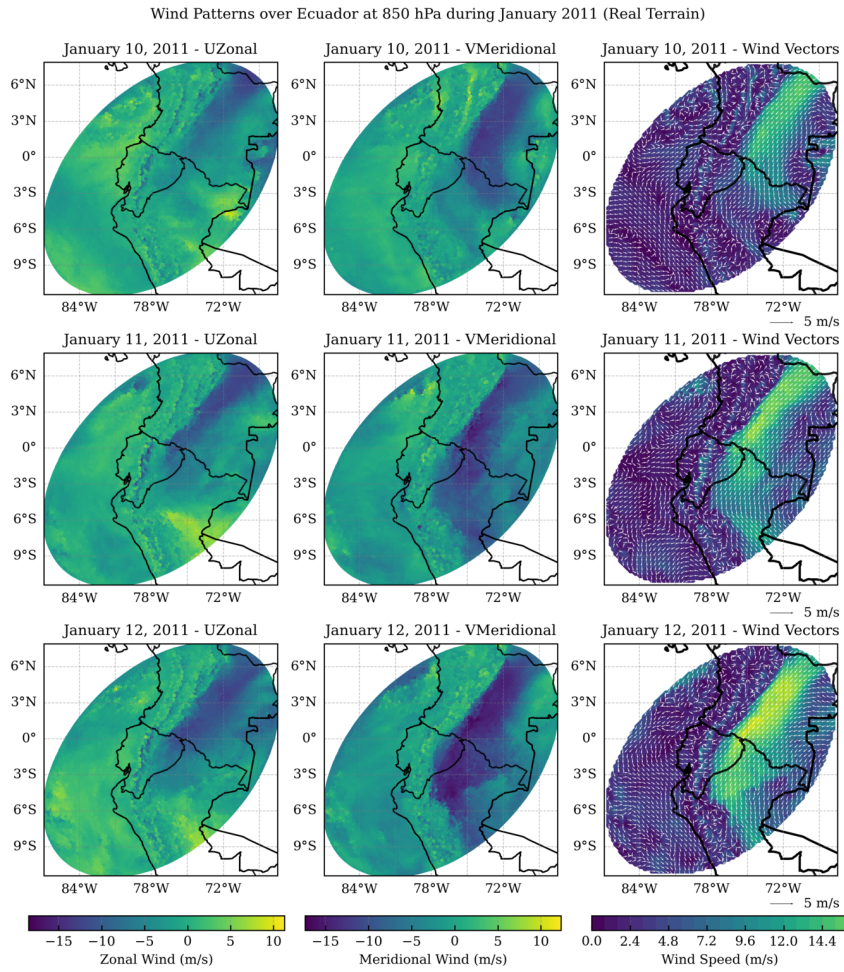


Figure 3.9: Wind patterns at 850 hPa over Ecuador in January 2011 (Real Terrain). White arrows indicate wind direction (5 m/s reference), with speeds up to ~ 14.4 m/s.

October, 1984

Zonal wind ranges from approximately -10 m/s (westward) to +10 m/s (eastward). On October 5 show a mix of eastward and westward flows. This variability persists on October 6 and 7, with strong westerly winds in the northern areas and easterly winds in others. Meridional wind ranges from ~ -10 m/s (southward) to $\sim +10$ m/s (northward). The plot indicates a predominantly south-to-north flow on October 5, which intensifies on October 6 and 7, particularly in the central and northern regions. Wind speeds range from 0 to ~ 12.6 m/s. The vectors reveal intricate wind patterns, with high-speed winds in the Amazon basin and directional changes influenced by the Andes, indicating significant terrain impact on airflow (Figure 3.10).

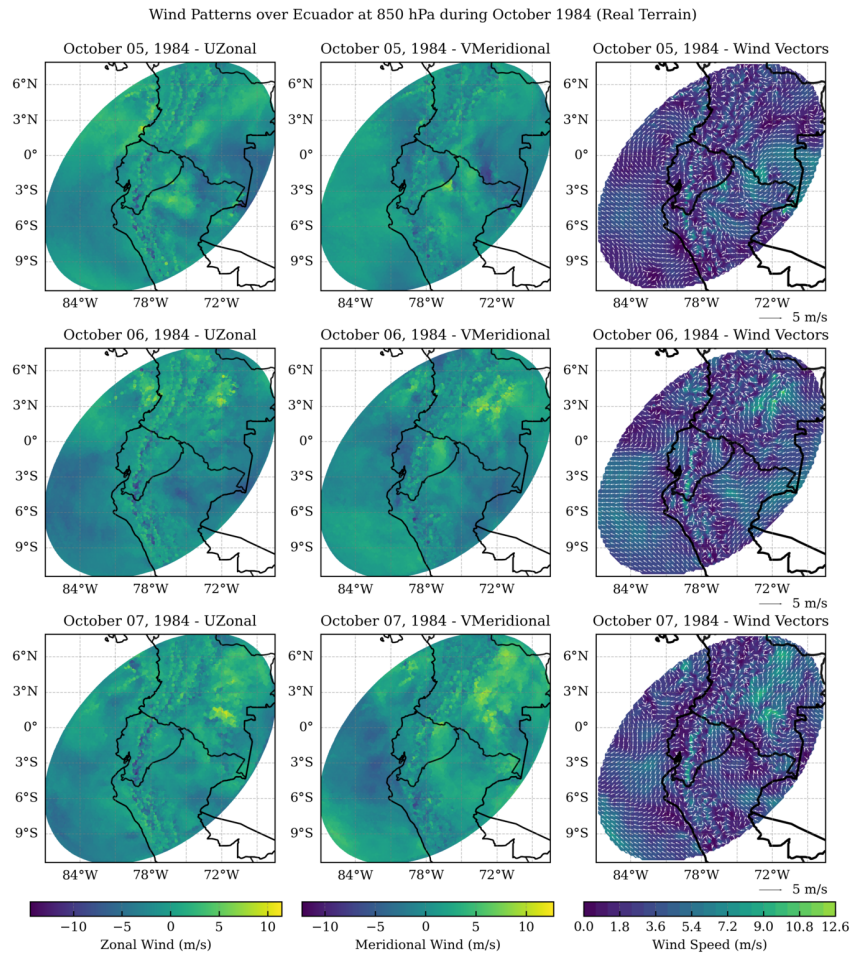


Figure 3.10: Wind patterns at 850 hPa over Ecuador in October 1984 (Real Terrain). White arrows indicate wind direction (5 m/s reference).

December, 1995

Zonal wind ranges from approximately -10 m/s (westward) to +15 m/s (eastward). On December 10, exhibits a mixture of easterly and westerly flows across Ecuador. By December 11 and 12, the patterns highlight stronger westerly winds in the north and consistent easterly winds in the south. Meridional wind values range from ~ -20 m/s (southward) to $\sim +10$ m/s (northward). On December 10, reveals a predominantly south-to-north flow, especially the eastern side, with significant southward winds over the Andes and Amazon basin. This pattern intensifies on December 11 and 12. Wind speeds continue to range from 0 to ~ 14.4 m/s. On December 10 shows complex patterns with varying speeds, particularly high in Amazon basin and directional changes influenced by the Andes. By December 11 and 12, the wind flows become more organized and stronger (Figure 3.11).

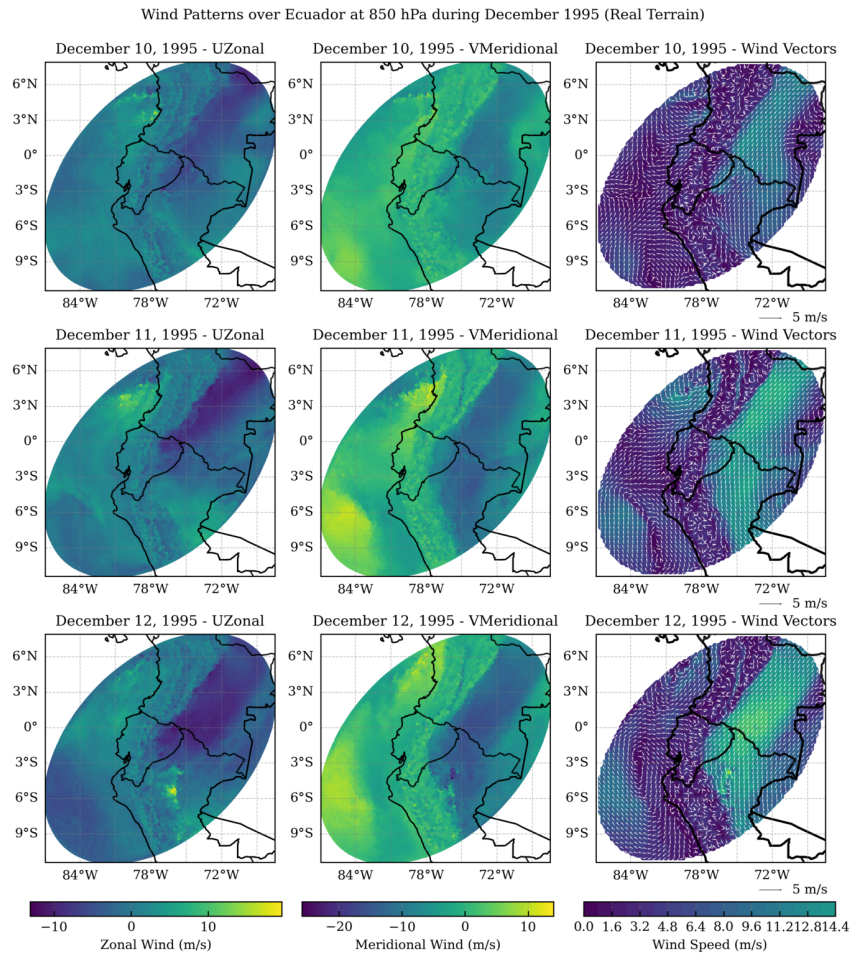


Figure 3.11: Wind patterns at 850 hPa over Ecuador in December 1995 (Real Terrain), showing complex convergence and divergence. White arrows indicate wind direction (5 m/s reference), with speeds up to ~ 14.4 m/s.

January, 2001

Zonal wind ranges from approximately -10 m/s (westward) to +10 m/s (eastward). On January 15 shows a mix of easterly and westerly flows with varying intensities across Ecuador. By January 16 and 17, the patterns highlight stronger westerly winds in the north and consistent easterly winds in the south. Meridional wind values range from ~ -10 m/s (southward) to $\sim +10$ m/s (northward). On January 15 reveals a predominantly south-to-north flow, which intensifies on January 16 and 17, particularly in the northern and central regions. The wind vectors on January 15 show complex patterns with varying speeds, particularly high in the northern regions. By January 16 and 17, the wind flows become more organized and stronger with high-speed winds (up to ~ 14.4 m/s) concentrated along the Amazon basin and some parts of the Andes (Figure 3.12).

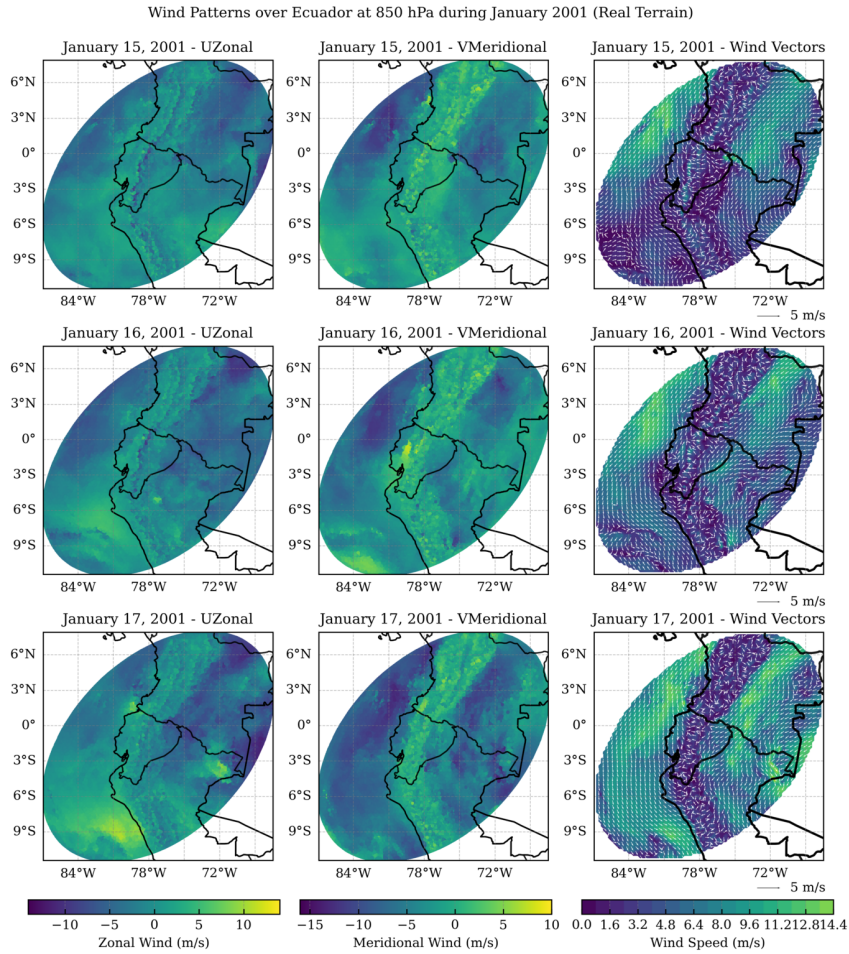


Figure 3.12: Wind patterns at 850 hPa over Ecuador for three consecutive days in January 2001 (Real Terrain). The white arrows on the wind vector maps indicate wind direction, with their length corresponding to a reference wind speed of 5 m/s. complex patterns of convergence and divergence, with wind speeds reaching up to ~ 14.4 m/s

3.2 Role of the Andes Elevation

To further explore the influence of the Andes on atmospheric dynamics, we analyzed simulations with the terrain reduced to half, 10%, and especially 1% of its actual height. These variations in elevation allow us to isolate and understand the role of the Andes in shaping wind patterns over continental Ecuador.

Given the complexity and the significant differences observed in the plots of the datasets, we strategically selected one representative date for each climatic event—both El Niño and La Niña—to focus our analysis. By concentrating on specific dates that capture the essence of these phenomena, we provide a clear and comprehensive analysis without diluting our findings.

3.2.1 Half Height

Strong El Niño Event: March, 1983

The U -zonal wind map shows strong eastward winds, particularly along the coast, with velocities reaching up to ~ 15 m/s. The V -meridional wind map indicates northward winds along the coast and eastern regions; southward winds are observed over the Andes and some western areas. The wind vector plot ranges from 0 to ~ 14.4 m/s and demonstrates a consistent mix of northerly and easterly winds converging over the Andes and diverging along the coast and Amazon basin (Figure 3.13).

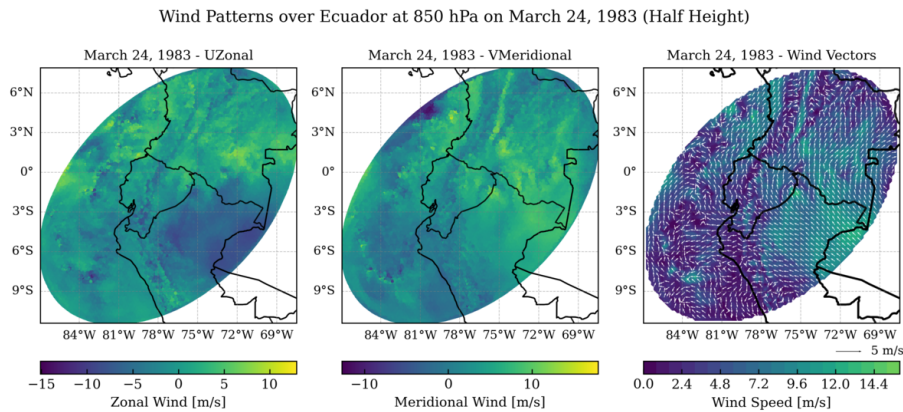


Figure 3.13: Wind patterns at 850 hPa over Ecuador on March 24, 1983 (Half Height). Less pronounced patterns are observed compared to the actual height scenario.

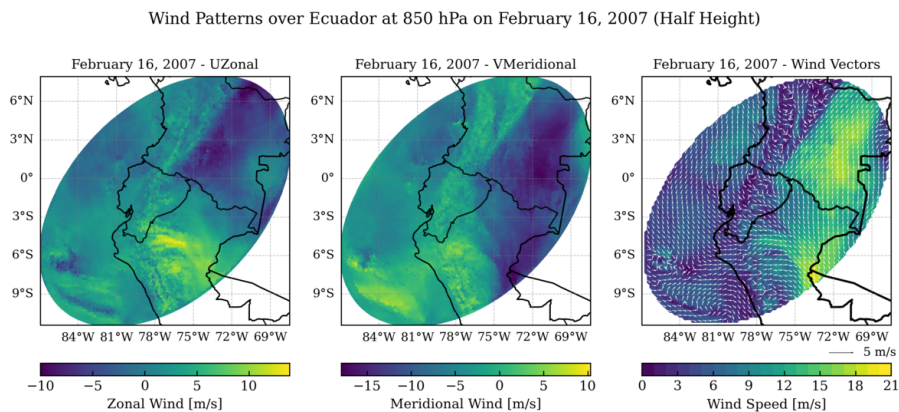


Figure 3.14: Wind patterns at 850 hPa over Ecuador on February 16, 2007 (Half Height). Notable convergence and divergence patterns, with wind speeds reaching up to 21 m/s.

Weak El Niño Event: February, 2007

On February 16, 2007, the U -zonal wind map shows predominantly eastward winds in the western region, while the southern regions and over the Andes experience westward

winds. The V -meridional wind map ranges from ~ -15 m/s (southward) to $\sim +10$ m/s (northward). It indicates northward winds are significant along the eastern regions and southward winds over the Andes and some western areas. Wind vectors reveal a mix of northerly and easterly winds converging over the Andes and diverging along the coast and Amazon basin (Figure 3.14).

Strong La Niña Event: November, 1998

The U -zonal wind map on November 6, 1998, shows significant variability, with strong eastward winds along the coast. The V -meridional wind map displays predominantly southward winds in the northern regions and mixed patterns in the central regions. Wind speeds range from 0 to ~ 18 m/s and indicate high-speed winds and significant convergence zones in eastern Ecuador (Figure 3.15).

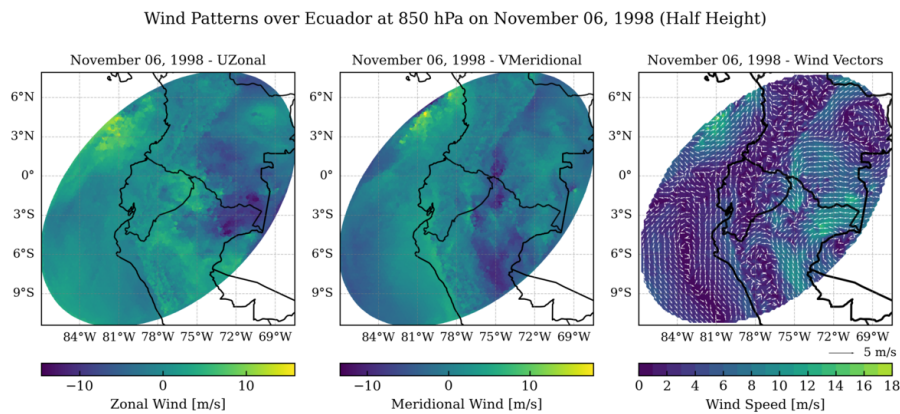


Figure 3.15: Wind patterns at 850 hPa over Ecuador on November 6, 1998 (Half Height)

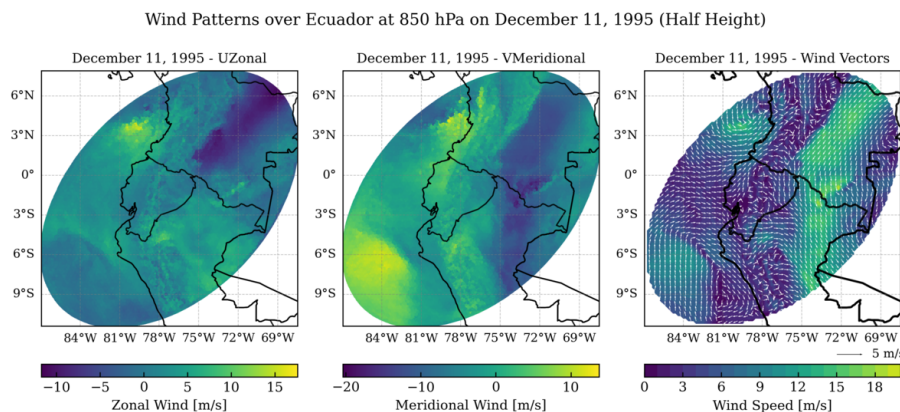


Figure 3.16: Wind patterns at 850 hPa over Ecuador on December 11, 1995 (Half Height)

Weak La Niña Event: December, 1995

On December 11, 1995, the U -zonal wind map shows a mix of easterly and westerly winds across Ecuador. The V -meridional wind map reveals strong south-to-north flows in central

regions. Wind vector plots highlight the influence of the Andes on wind patterns, showing high-speed winds in the north and organized flows in central Ecuador (Figure 3.16).

3.2.2 10% Height

Strong El Niño Event: March, 1983

On March 24, 1983, zonal winds exhibited consistent eastward flows across the region with minimal disruption from the Andes. Meridional winds show a slight northward component in central and northern Ecuador. The wind vectors indicate uniform wind speeds and directions, reflecting the reduced topographic influence.

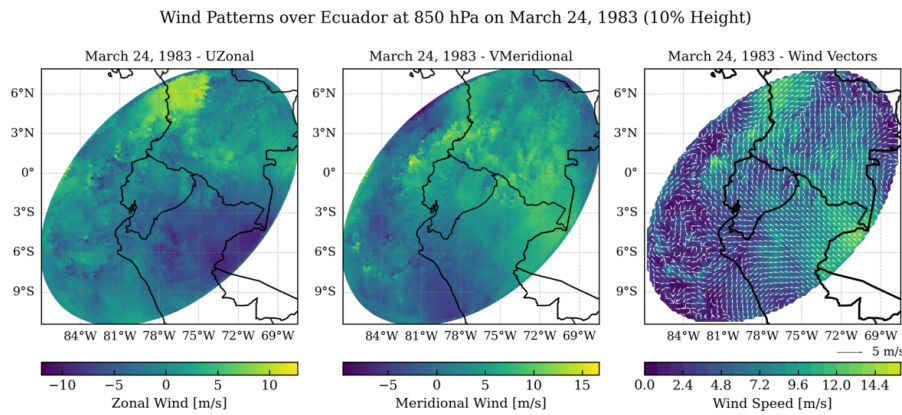


Figure 3.17: Wind patterns at 850 hPa over Ecuador on March 24, 1983 (10% Height)

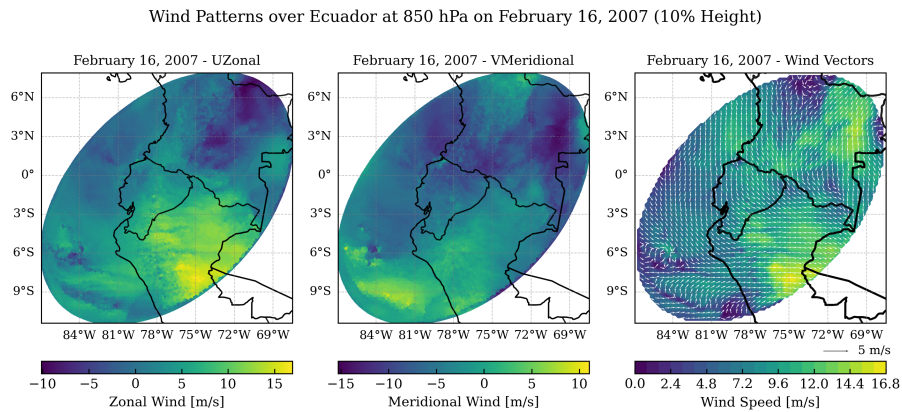


Figure 3.18: Wind patterns at 850 hPa over Ecuador on February 16, 2007 (10% Height)

Weak El Niño Event: February, 2007

On February 16, 2007, zonal winds displayed a mixture of eastward and westward flows, showing minimal disruption. Meridional winds present a weak south-to-north flow. The

wind vectors demonstrate low variability in speed and direction, consistent with the diminished influence of the Andes.

Strong La Niña Event: November, 1998

On November 6, 1998, zonal winds were predominantly eastward, covering the region uniformly. Meridional winds indicate minor northward flows in the eastern areas. Wind vectors highlight uniform wind patterns with consistent speeds, indicative of the negligible height.

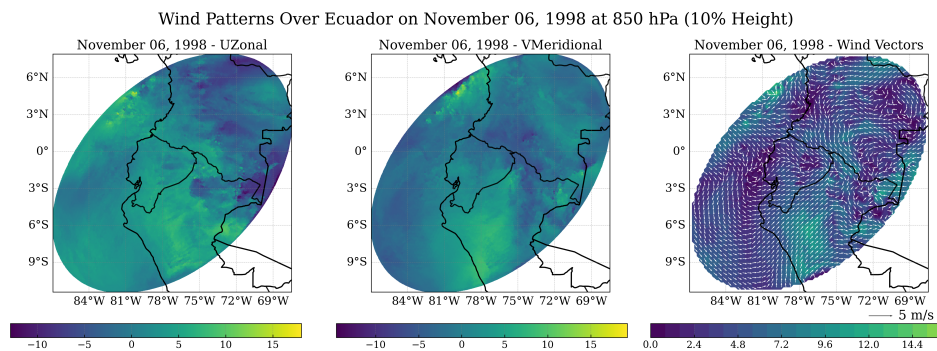


Figure 3.19: Wind patterns at 850 hPa over Ecuador on November 6, 1998 (10% Height)

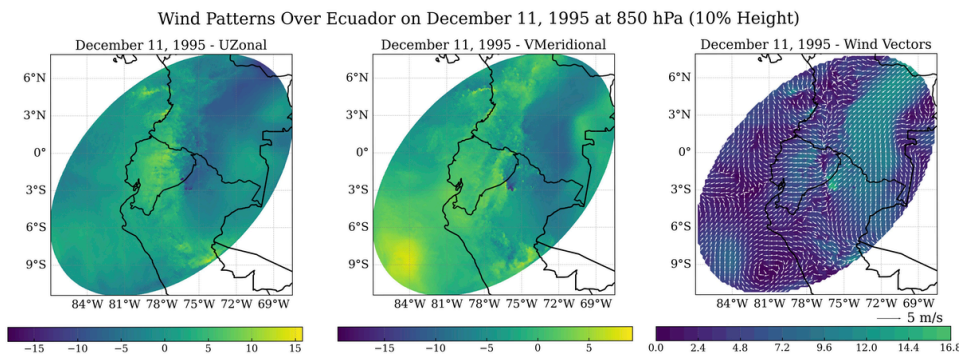


Figure 3.20: Wind patterns at 850 hPa over Ecuador on December 11, 1995 (10% Height)

Weak El Niño Event: December, 1995

The wind patterns over Ecuador on December 11, 1995, at 850 hPa show a predominant easterly flow, with variations in north-south wind components. The U-Zonal wind component highlights strong easterly winds across most of Ecuador, particularly along the coast, while the V-Meridional component shows mixed northerly and southerly winds in central Ecuador. The wind vector plot shows that the reduced Andes lead to less pronounced deflections and accelerations.

3.2.3 1% Height

Strong El Niño Event: March, 1983

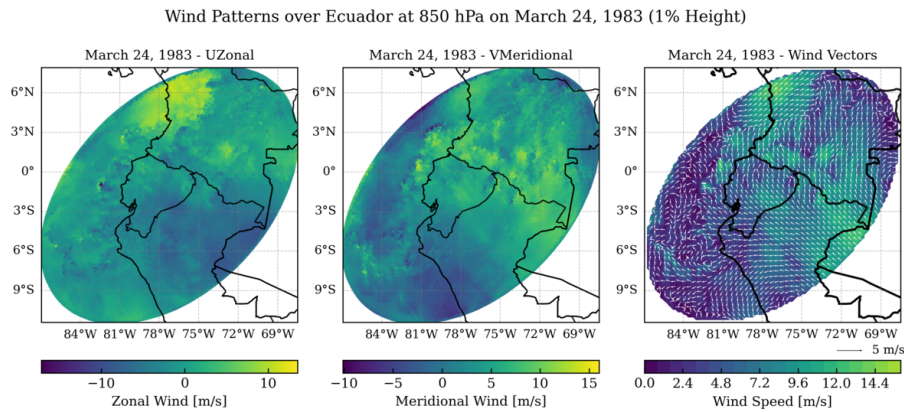


Figure 3.21: Wind patterns at 850 hPa over Ecuador on March 24, 1983 (1% Height)

On March 24, 1983, zonal winds exhibited consistent eastward flows across the region with reduced influence from the Andes. Meridional winds show a slight northward component in central and northern Ecuador. The wind vectors indicate uniform wind speeds and directions, reflecting the minimal topographic.

Weak El Niño Event: February, 2007

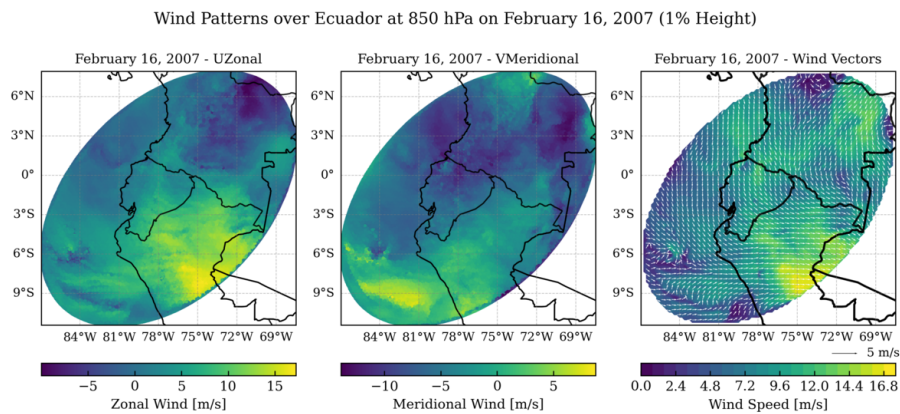


Figure 3.22: Wind patterns at 850 hPa over Ecuador on February 16, 2007 (1% Height)

On February 16, 2007, zonal winds displayed a mixture of eastward and westward flows, showing minimal disruption. Meridional winds present a weak south-to-north flow. The wind vectors demonstrate low variability in speed and direction.

Strong La Niña Event: November, 1998

On November 6, 1998, zonal winds were predominantly eastward, covering the region uniformly. Meridional winds indicate minor northward flows in the eastern areas. Wind vectors highlight uniform wind patterns with consistent speeds.

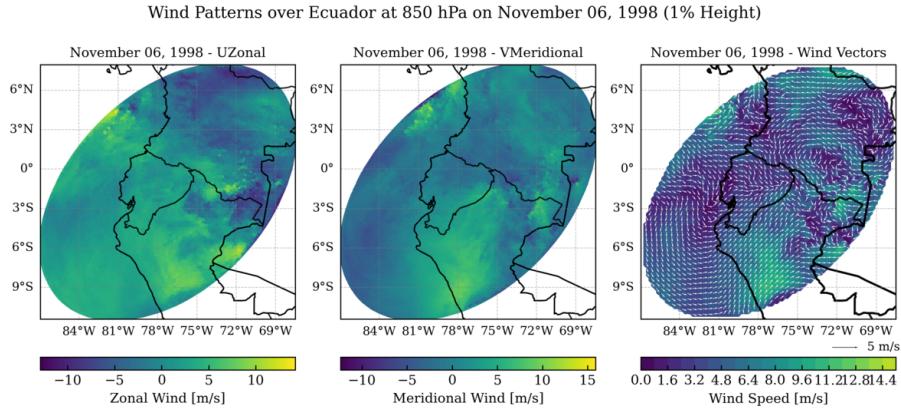


Figure 3.23: Wind patterns at 850 hPa over Ecuador on November 6, 1998 (1% Height)

Weak El Niño Event: December, 1995

On December 11, 1995, zonal winds showed a combination of eastward and westward movements without significant variation. Meridional winds reveal a weak northward trend. The wind vectors illustrate uniform patterns and speeds, reflecting the minimal impact of the Andes.

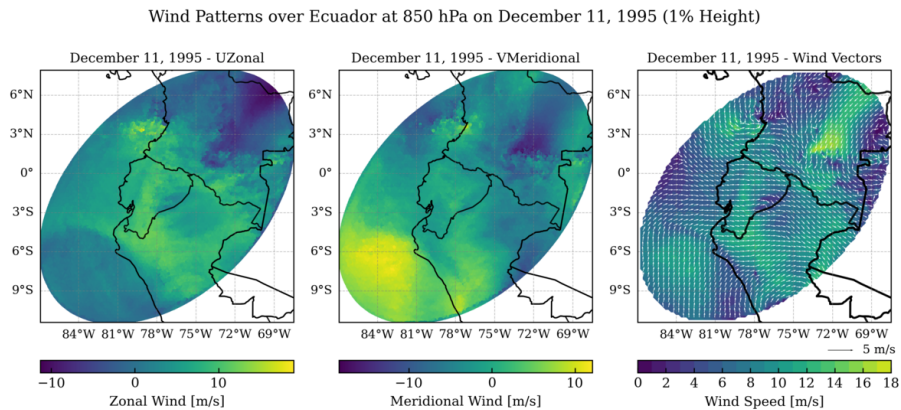


Figure 3.24: Wind patterns at 850 hPa over Ecuador on December 11, 1995 (1% Height)

3.2.4 Overall Elevation Impact

- Elevation has a strong impact on laminarity. As the terrain height increases, we observe more and more turbulence, and as the terrain elevation is reduced, more uniform and straightforward wind flows are observed.

- Terrain elevation introduces turbulence. At half the actual height, the Andes still exert a noticeable influence on wind patterns, though the effects are less pronounced compared to the actual elevation. Reducing the Andes to 10% of their actual height diminishes their impact further, resulting in more linear and less disrupted wind patterns. At 1% of their actual height, the Andes' impact is minimal. Wind patterns become almost uniform, highlighting the minimal topographic obstruction to atmospheric flows.
- Including realistic terrain elevation is essential for capturing accurate wind patterns over Ecuador. Models lacking realistic elevation data will fail to replicate the observed complexity and variability in wind flows, which emphasizes the need for detailed topographic representations.

3.3 Vertical Cross-Section Analysis

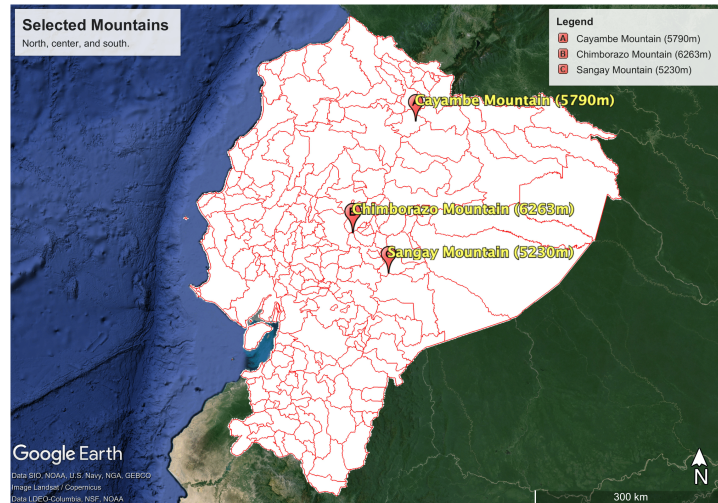


Figure 3.25: Ecuador's Peaks: Cayambe, Chimborazo, and Sangay - This map highlights the geographic locations and elevations of Cayambe (5790m), Chimborazo (6263m), and Sangay (5230m), representing the significant mountainous landmarks in the northern, central, and southern regions of Ecuador respectively.

To deepen our understatement, we will examine vertical cross-sections of the zonal wind component around three significant mountains: Cayambe in the north, Chimborazo in the center, and Sangay in the south (Figure 3.25). These mountains were selected due to their considerable heights and prominent roles in influencing local and regional atmospheric dynamics. Cayambe, at 5,790 meters, disrupts airflow and affects local climates. Chimborazo, the tallest peak in Ecuador at 6,310 meters, significantly modulates atmospheric circulation near the equator. Sangay, at 5,230 meters, is known for its volcanic activity and substantial impact on regional wind patterns. The comparative analysis of zonal wind includes two vertical cross-sections: one at the actual terrain height and the other one at 1% of this height. By comparing them, we aim to isolate and understand the specific topographical effects on zonal wind components.

3.3.1 Cayambe Mountain

Strong El Niño Event: March, 1983

- **Full Height (Cross-Section a):** The cross-section spans from the surface up to an altitude of 20,000 meters. At lower altitudes, below 5,000 meters, the terrain causes the airflow to be deflected and accelerated around the peak, resulting in variable wind speeds. This variability is a direct consequence of the intricate topographic features of the Andes, which act as barriers and channels for the airflow. At altitudes between 5,000 and 15,000 meters, the zonal wind speeds show a high degree of variability, with pockets of stronger winds interspersed with regions of calmer winds. Above 15,000 meters, the influence of the topography is less pronounced, and the wind speeds become more uniform.
- **1% Height (Cross-Section b):** The maximum wind speeds are lower, reaching up to ~ 6 m/s, indicated by lighter yellow and green shades. The reduction in elevation removes many of the barriers that cause turbulence, resulting in a more uniform wind pattern.

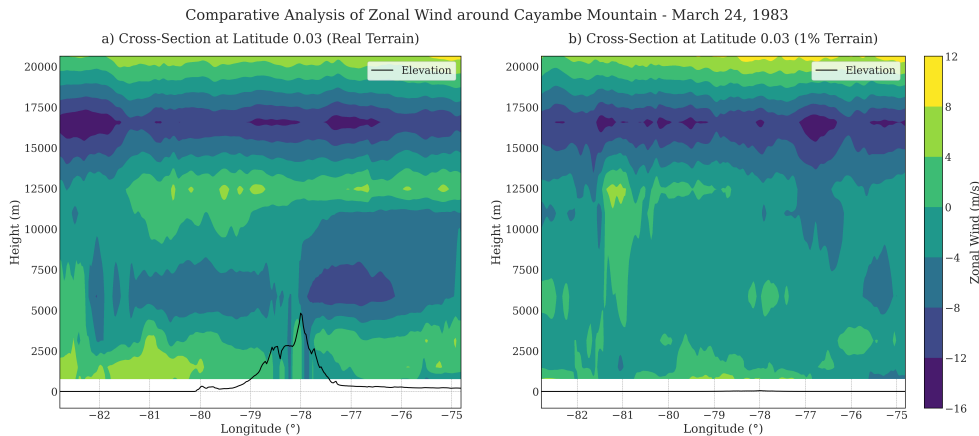


Figure 3.26: Zonal Wind at 850 hPa around the Cayambe Mountain, March 1983

Weak El Niño Event: February, 2007

- **Full Height (Cross-Section a):** At full height, the zonal wind component around Cayambe Mountain demonstrates distinct variation with elevation. The presence of the Andes induces significant wind shear near the peak, influencing airflow patterns considerably. Strong westward winds dominate above 10 km, while eastward winds prevail below this altitude. The complex topography of the Andes contributes to these varying wind speeds, creating zones of accelerated wind flow and turbulence.
- **1% Height (Cross-Section b):** When the Andes are reduced to 1% of their actual height, the zonal wind patterns show minimal variation. The influence of the terrain is greatly reduced. Westward winds remain consistent across all elevations, with little

to no disruption. The substantial reduction in height leads to a simpler wind patterns and decreased wind shear.

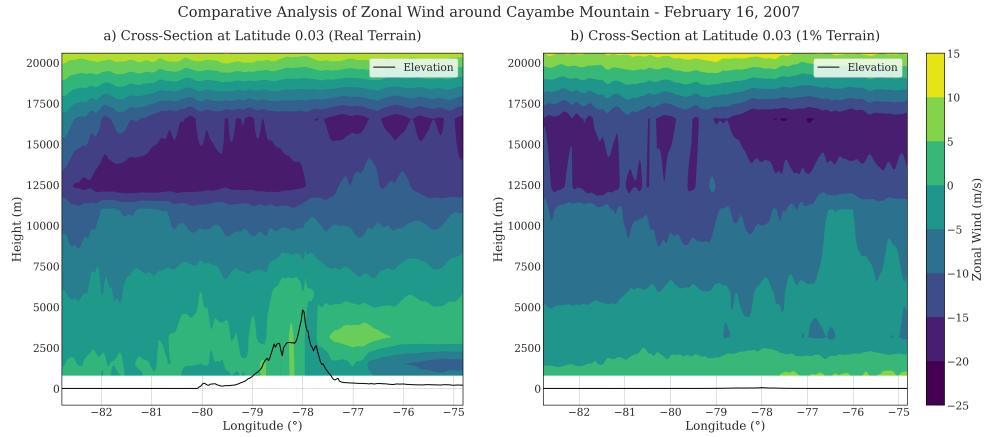


Figure 3.27: Zonal Wind at 850 hPa around the Cayambe Mountain, February 2007

Strong La Niña Event: November, 1998

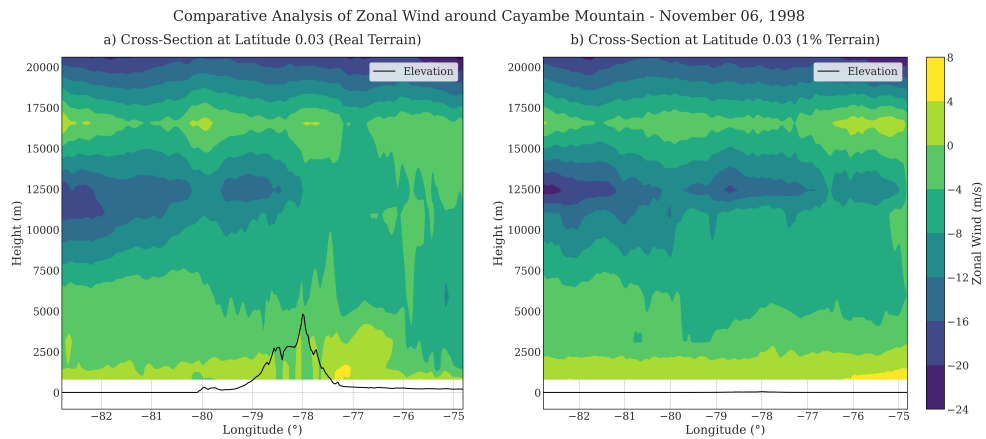


Figure 3.28: Zonal Wind at 850 hPa around the Cayambe Mountain, November 1998

- **Full Height (Cross-Section a):** In the full height cross-section for November 1998, the zonal wind around Cayambe Mountain shows significant variation with altitude. At lower altitudes, the winds are predominantly easterly, transitioning to more westerly winds at higher altitudes above the mountain peak. The presence of the Andes creates a pronounced wind shadow on the leeward side, with strong wind shear evident across different altitudes.
- **1% Height (Cross-Section b):** The influence of the Andes is minimal. The zonal wind shows a more uniform distribution with less pronounced wind shear and no significant wind shadow effect. The wind patterns are relatively consistent across the profile, indicating the reduced impact of the topography on atmospheric flow.

Weak La Niña Event: December, 1995

- **Full Height (Cross-Section a)**: For December 1995, the full height cross-section indicates substantial wind variation due to the presence of Cayambe Mountain. The lower altitudes exhibit easterly winds that shift to westerly at higher altitudes. The wind shadow effect is clear, with a marked decrease in wind speed on the western side of the mountain, accompanied by notable wind shear.
- **1% Height (Cross-Section b)**: In the 1% height cross-section, the zonal wind distribution is more uniform. The wind patterns are relatively steady, lacking the wind shadow and significant shear observed in the full height profile. This indicates a reduced topographic impact on wind flow when the terrain is minimized.

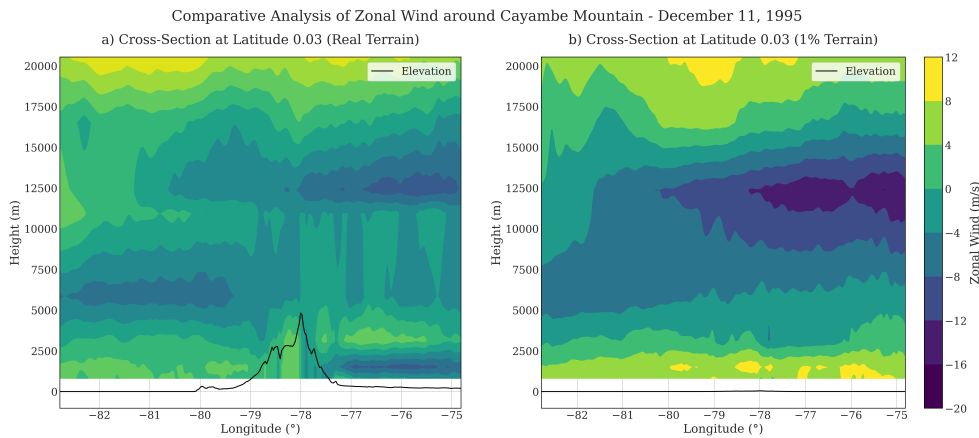


Figure 3.29: Zonal Wind at 850 hPa around the Cayambe Mountain, December 1995

3.3.2 Chimborazo Mountain

Strong El Niño Event: March, 1983

- **Full Height (Cross-Section a)**: The zonal wind profiles reveal significant westward flow, especially at altitudes above 10,000 meters. The Chimborazo Mountain induces substantial deceleration of wind speeds at lower elevations (below 5,000 meters), indicating pronounced orographic effects. This topographical influence forces wind to ascend, creating a shadow effect with reduced speeds on the lee side. Wind speeds range from ~ -20 m/s (dark purple) to ~ 10 m/s (yellow), demonstrating the impact of terrain on wind dynamics.
- **1% Height (Cross-Section b)**: At 1% of the terrain height, the wind flow becomes more uniform and less affected by topography. Wind speeds range between ~ -8 m/s and ~ 8 m/s, showing minimal variations. This indicates that reducing terrain height leads to smoother wind profiles, highlighting the significant influence of actual terrain height on atmospheric circulation.

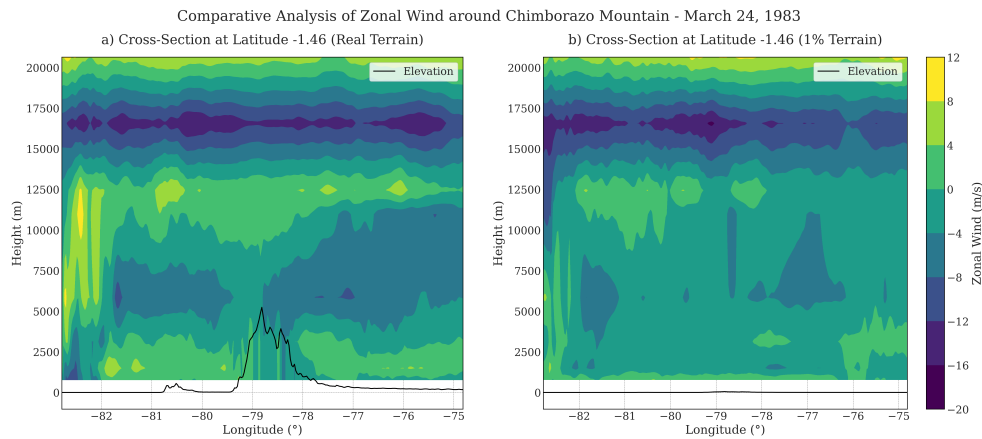


Figure 3.30: Zonal Wind at 850 hPa around the Chimborazo Mountain, March 1983

Weak El Niño Event: February, 2007

- **Full Height (Cross-Section a)**: Moderate westward wind flow interacts with the Chimborazo Mountain, causing deceleration at lower altitudes (below 5,000 meters) and increased speeds at higher altitudes (around 10,000 meters). Wind speeds range from ~ 15 m/s to ~ 10 m/s, reflecting the terrain's role in altering vertical wind profiles.
- **1% Height (Cross-Section b)**: With reduced terrain height, the wind flow is more streamlined, with speeds ranging from ~ 8 m/s to ~ 8 m/s. The orographic effects are minimized, leading to less turbulent flow. This underscores the crucial role of full terrain height in modifying wind patterns during weak El Niño events.

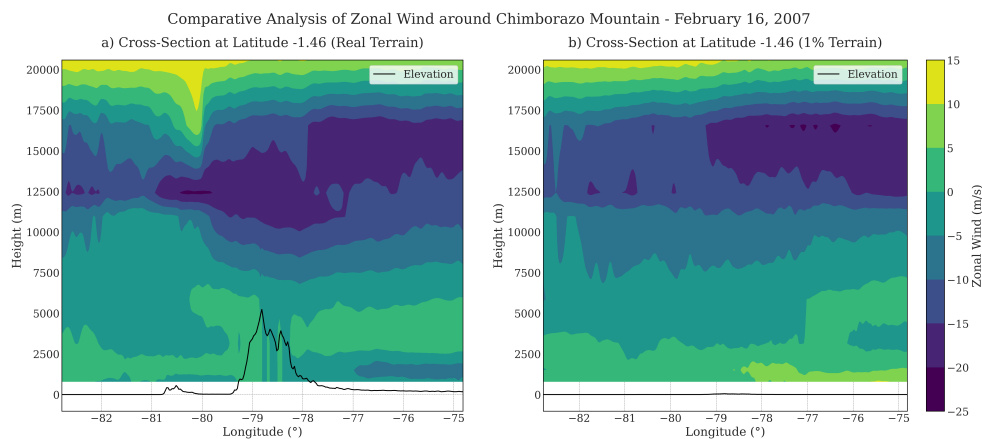


Figure 3.31: Zonal Wind at 850 hPa around the Chimborazo Mountain, Feb 2007

Strong La Niña Event: November, 1998

- **Full Height (Cross-Section a)**: Robust westward wind flow is significantly impacted by the Chimborazo Mountain, with marked reductions in speed at lower

altitudes due to strong orographic lifting and deflection. Wind speeds range from ~ 20 m/s to ~ 8 m/s, illustrating how the mountain forces winds to ascend, creating varied profiles.

- **1% Height (Cross-Section b):** Reduced terrain height results in a more uniform wind flow, with minimal terrain interaction. Wind speeds range from ~ 8 m/s to ~ 8 m/s, indicating a smoother profile with less orographic influence, highlighting the primary role of full terrain height during strong La Niña events.

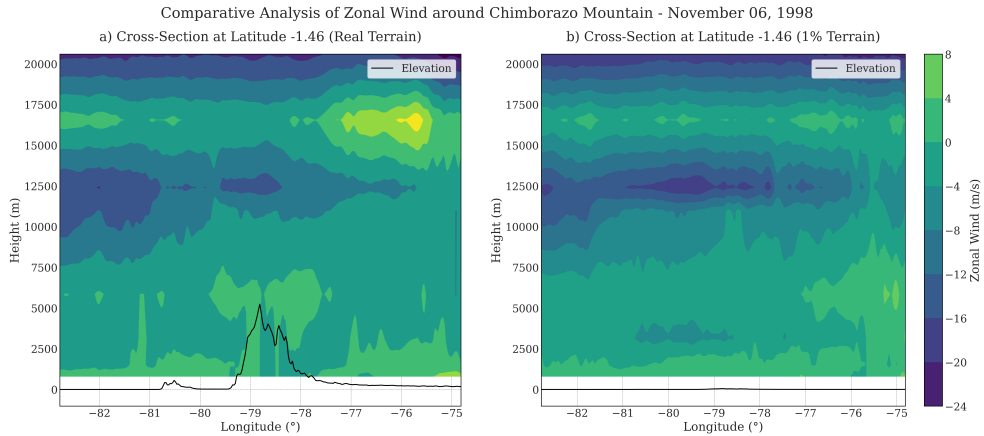


Figure 3.32: Zonal Wind at 850 hPa around the Chimborazo Mountain, November 1998

Weak La Niña Event: December, 1995

- **Full Height (Cross-Section a):** Zonal wind profiles indicate strong westward flow, significantly influenced by the Chimborazo Mountain. The terrain causes wind speed reductions and deflections at lower altitudes, with speeds ranging from ~ 16 m/s to ~ 12 m/s. This suggests strong orographic lifting and alteration of wind patterns.

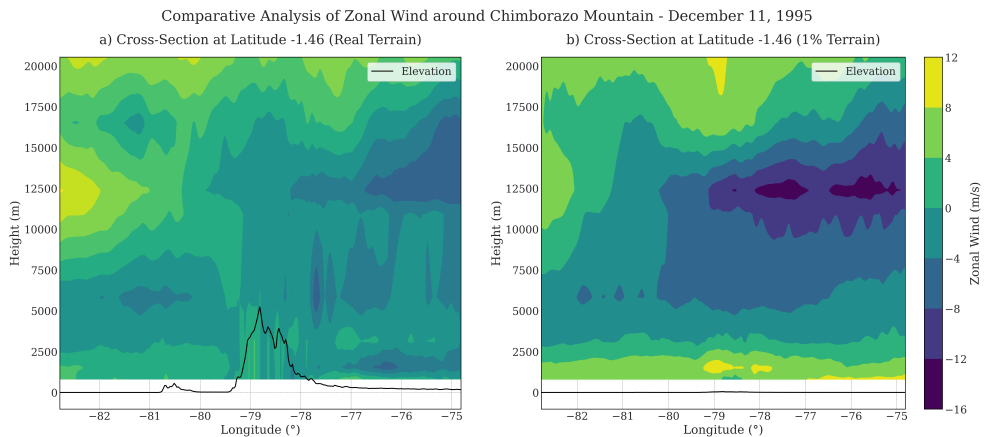


Figure 3.33: Zonal Wind at 850 hPa around the Chimborazo Mountain, December 1995

- **1% Height (Cross-Section b):** At reduced terrain height, the wind flow is homogeneous, with speeds ranging from ~ 8 m/s to ~ 8 m/s. The orographic influence is minimal, leading to less disruption. This demonstrates the significant impact of Chimborazo Mountain’s full height on wind dynamics during weak La Niña events.

3.3.3 Sangay Mountain

Strong El Niño Event: March, 1983

- **Full Height (Cross-Section a):** This cross-section reveals significant zonal wind velocities, with a peak of 12 m/s around 13000 m. The influence of Sangay Mountain is noticeable, disrupting wind patterns at lower altitudes with velocities ranging between ~ 8 m/s and ~ 4 m/s around 3,000 m to 7,500 m. The terrain effect is prominent up to 10,000 m, with velocities oscillating around the mountain’s elevation.
- **1% Height (Cross-Section b):** In this reduced terrain height scenario, the disruption caused by the Sangay Mountain is minimal. The wind velocities exhibit a more uniform pattern with dominating speeds ranging between ~ 2 m/s to ~ 6 m/s throughout the cross-section. The highest velocities are observed around 10,000 m, maintaining a relatively steady profile above 5,000 m.

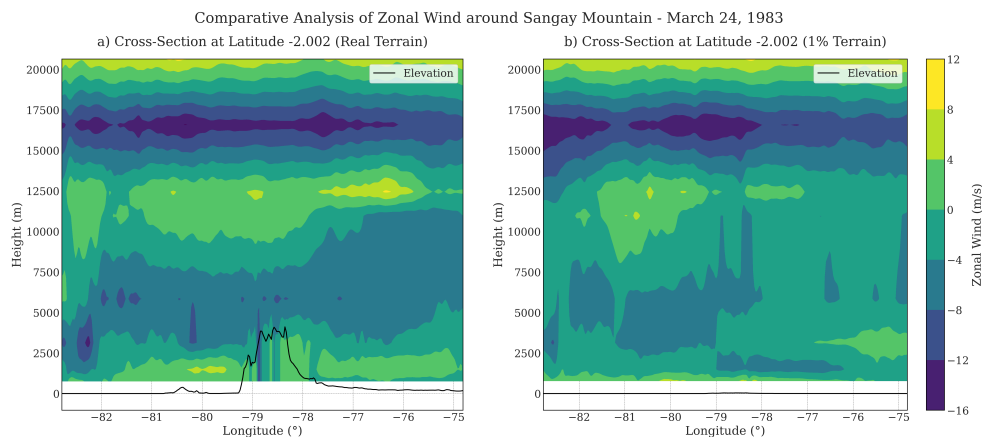


Figure 3.34: Zonal Wind at 850 hPa around the Sangay Mountain, March 1983

Weak El Niño Event: February, 2007

- **Full Height (Cross-Section a):** The zonal wind profile shows velocities reaching ~ 15 m/s around 10,000 m. The impact of Sangay Mountain is evident as wind speeds decrease significantly to ~ 6 m/s between 3,000 m and 7,500 m, illustrating the influence of the mountains on airflow disruption.
- **1% Height (Cross-Section b):** The reduced terrain height cross-section shows a smoother wind profile with velocities ranging from ~ 2 m/s to ~ 8 m/s. The highest wind speeds are seen around 10,000 m, with minimal disruption near the ground level, indicating the lessened effect of terrain at 1% height.

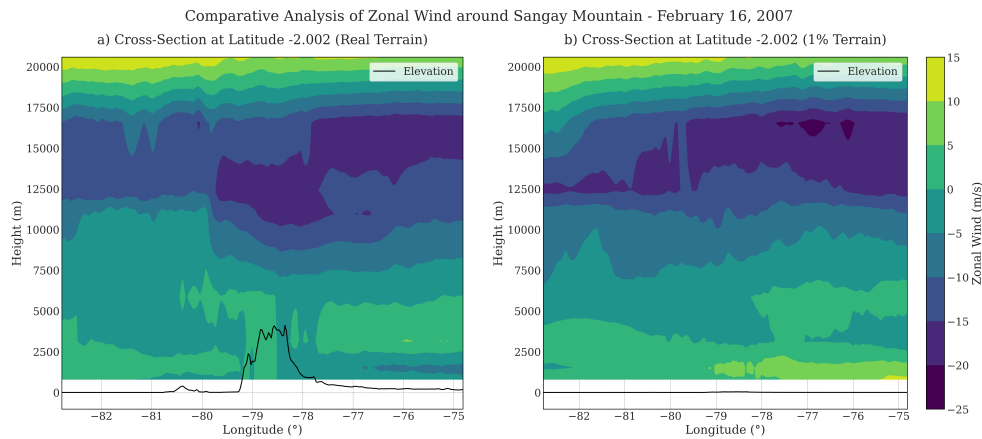


Figure 3.35: Zonal Wind at 850 hPa around the Sangay Mountain, February 2007

Strong La Niña Event: November, 1998

- **Full Height (Cross-Section a):** This cross-section displays zonal wind velocities peaking at ~ 8 m/s around 15,000 m. The Sangay Mountain significantly disrupts the wind pattern, especially between 2,500 m and 10,000 m, with velocities dipping to ~ -12 m/s in the vicinity of the mountain.

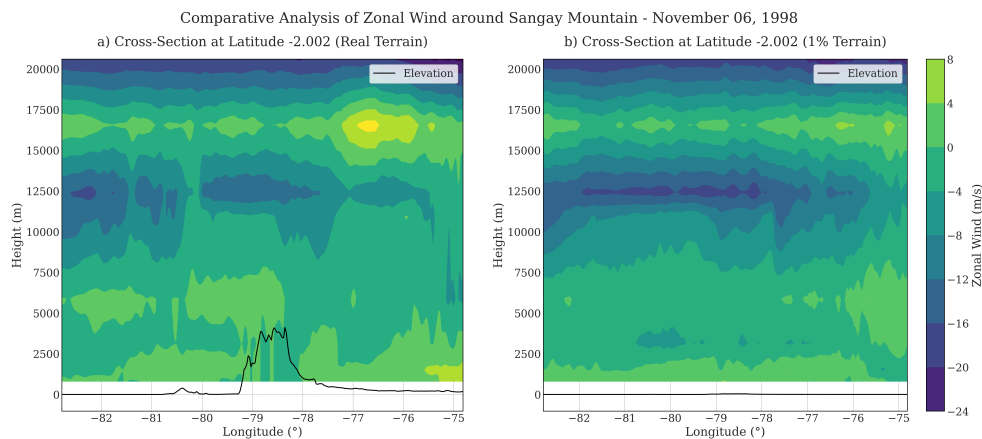


Figure 3.36: Zonal Wind at 850 hPa around the Sangay Mountain, November 1998

- **1% Height (Cross-Section b):** The wind profile at 1% terrain height is more uniform, with velocities varying between ~ -4 m/s and ~ 4 m/s. The highest velocities are around 10,000 m, with minimal disruption at lower altitudes, reflecting a smoother airflow.

Weak La Niña Event: December, 1995

- **Full Height (Cross-Section a):** The zonal wind pattern shows velocities up to ~ 12 m/s around 15,000 m. The Sangay Mountain impacts the wind, with speeds dropping to ~ -8 m/s between 3,000 m and 10,000 m, indicating substantial terrain-induced disturbances.

- **1% Height (Cross-Section b):** The wind profile at 1% terrain height exhibits velocities ranging from ~ 4 m/s to ~ 8 m/s. The highest speeds occur near 10,000 m, with a smoother pattern at lower elevations, suggesting reduced terrain influence.

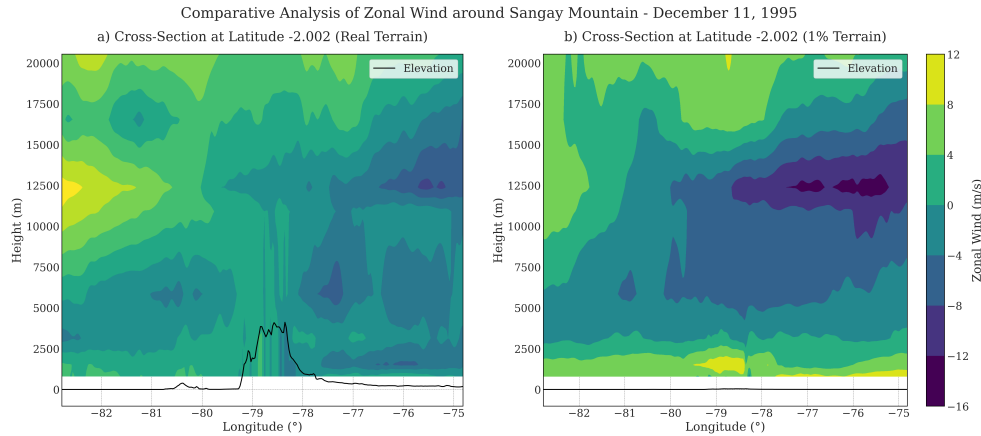


Figure 3.37: Zonal Wind at 850 hPa around the Sangay Mountain, December 1995

3.4 Impact on El Niño and La Niña Events

We also considered it important to examine the related atmospheric variables of relative humidity and precipitation. Winds play a pivotal role in the transport and distribution of moisture in the atmosphere, which directly influences relative humidity levels and precipitation rates. Moreover, changes in wind speed and direction can lead to significant variations in where and how much precipitation occurs.

3.4.1 Relative Humidity: Strong vs Weak El Niño Analysis

The analysis of relative humidity at 850 hPa, just like previous cases, focuses on the differences between real terrain and 1% terrain scenarios during strong and weak El Niño events (Figure 3.38).

Strong El Niño Events (March 24, 1983) - Maps at 850 hPa

- **Real Terrain:** The left panel of the top row displays the distribution of relative humidity across Ecuador and its neighboring regions. In this map, the color gradient ranges from purple (0%) to yellow (100%) relative humidity. Over much of Ecuador, particularly in the central and western areas, there are extensive regions of orange and yellow, signifying moderate to high humidity levels. Specifically, relative humidity over the west of Andes and the coastal areas of Ecuador reaches levels between $\sim 60\%$ and even $\sim 100\%$, driven by the strong El Niño event that enhances moisture transport from the Pacific Ocean. The Andes mountain range acts as a barrier that causes moist air to rise, resulting in orographic lifting and, consequently, an increase in moisture content on the windward (western) side of the mountains.

- **1% Terrain Height:** In the 1% terrain scenario, the effects of flattening the Andes become clear. The overall relative humidity over Ecuador decreases noticeably, particularly in the western and central regions. The previously high humidity values of $\sim 60\%$ to $\sim 100\%$ diminish significantly, with large portions of the area showing blue and purple colors, indicating humidity levels between $\sim 20\%$ and $\sim 40\%$. This dramatic reduction in humidity over Ecuador emphasizes the orographic role of the Andes in moisture retention during strong El Niño events. By flattening the terrain, the moisture-laden air from the Pacific no longer encounters a barrier, leading to less condensation and, thus, lower relative humidity across the region.
- **Difference between the real terrain map and the 1% terrain map:** The difference map (right panel) quantifies the change in relative humidity between the real and flattened terrain scenarios. In this panel, red areas represent regions where the relative humidity is lower in the flattened scenario, while green areas indicate regions with higher humidity. Over Ecuador, there is a striking reduction in relative humidity, especially along the Andes and the western part of the country, where relative humidity decreases by up to $\sim 40\%$ or more. This significant drop highlights the importance of the Andes in maintaining higher humidity levels during strong El Niño events, acting as a natural barrier that enhances condensation and moisture retention.

Weak El Niño Events - February 16, 2007

- **Real Terrain:** The bottom row examines the weak El Niño event on February 16, 2007, again focusing on the effects on Ecuador. In the real terrain scenario (left panel), the relative humidity is lower overall compared to the strong El Niño event. The purple and blue regions, representing lower humidity values (0% to $\sim 40\%$), dominate much of the eastern part of Ecuador, particularly in the Amazon basin. However, along the western Andes and parts of the coastal region, there are still patches of orange, indicating moderate humidity levels between $\sim 60\%$ and $\sim 90\%$. These regions are again influenced by the orographic lifting caused by the Andes. However, the weaker El Niño event results in less overall moisture being transported from the Pacific, leading to reduced humidity levels across the country.
- **1% Terrain:** In the 1% terrain scenario, the flattening of the Andes produces less dramatic changes than those seen in the strong El Niño case. The western regions of Ecuador, which previously exhibited moderate humidity now show lower values, ranging from $\sim 40\%$ to $\sim 60\%$. The purple and blue regions in the eastern part of the country remain largely unchanged, indicating that the overall reduction in terrain height has less impact during weaker El Niño events. Nevertheless, the flattening of the Andes still reduces relative humidity in the western regions, suggesting that even during weak El Niño phases, the terrain influences local moisture distribution.
- **Difference between the real terrain map and the 1% terrain map :** Over Ecuador, the red areas indicate a reduction in relative humidity in the western regions, particularly along the Andes and parts of the coastal region. However, the reduction is less significant compared to the strong El Niño event, with humidity

decreasing by up to $\sim 20\%$ in the flattened scenario. The green areas in the eastern part of the country indicate slightly higher relative humidity, suggesting that moisture is redistributed more evenly when the orographic barrier of the Andes is removed

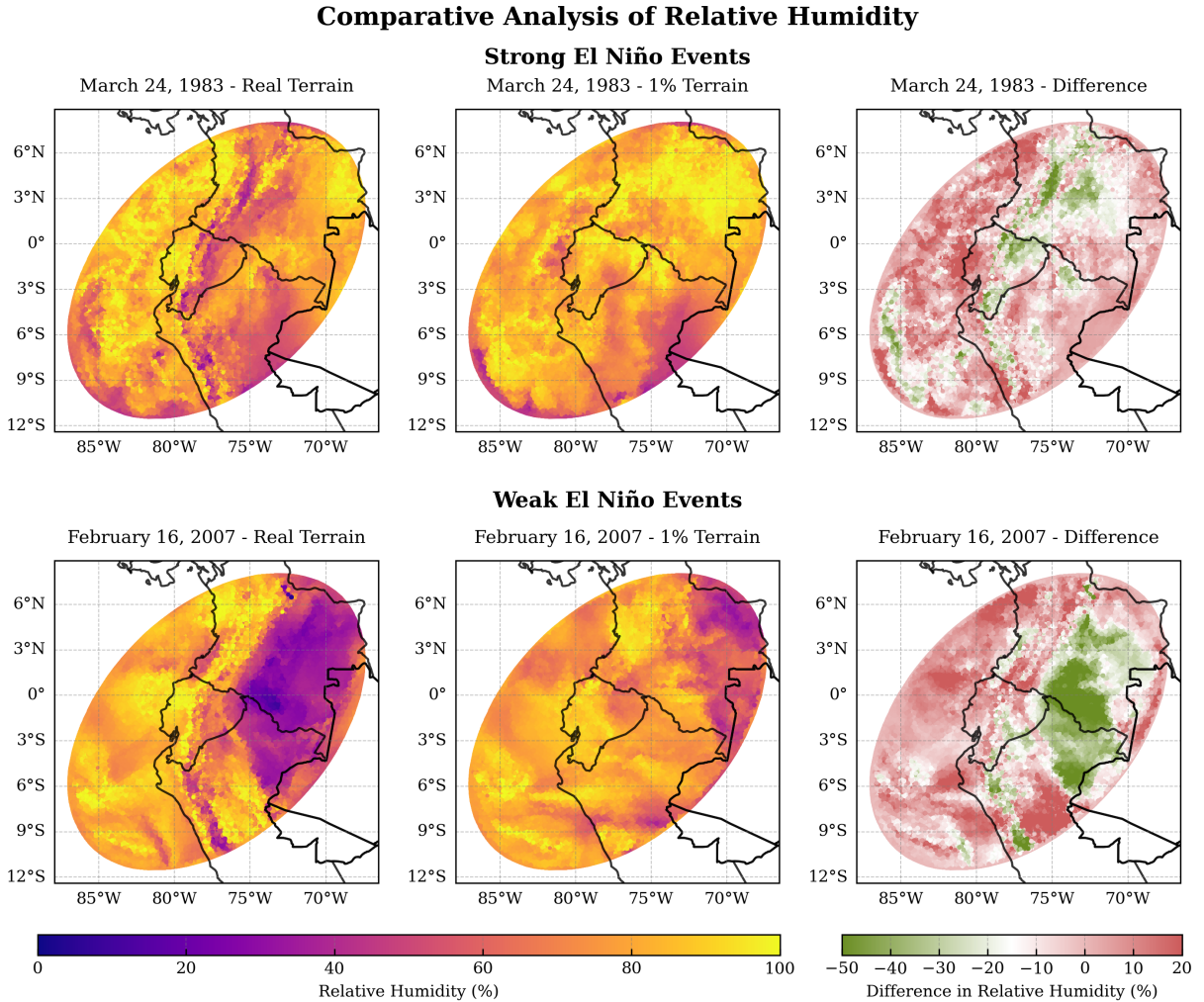


Figure 3.38: Comparative Analysis of Relative Humidity at 850hPa - Strong and Weak El Niño Events (Real terrain vs 1% terrain)

Cross Section: Strong El Niño Events (March 24, 1983)

Real Terrain (Cross section a) At lower altitudes, especially below 5,000 meters, the windward side of Chimborazo displays high relative humidity levels, as indicated by the yellow and orange areas, suggesting significant moisture uplift. Between 5,000 and 15,000 meters, there is a marked mix of high and low humidity bands, reflecting the turbulent interaction of air masses and the terrain; and above 15,000 meters, the influence of the topography diminishes.

1% Terrain (Cross section b) Lower altitudes show moderate relative humidity levels around $\sim 50\%$ to $\sim 70\%$. In mid-altitudes, the humidity distribution remains more consistent, lacking the complex interaction, as indicated by the relatively continuous orange and yellow bands. At higher altitudes, the influence of terrain is minimal; atmospheric dynamics dominate over topographic effects.

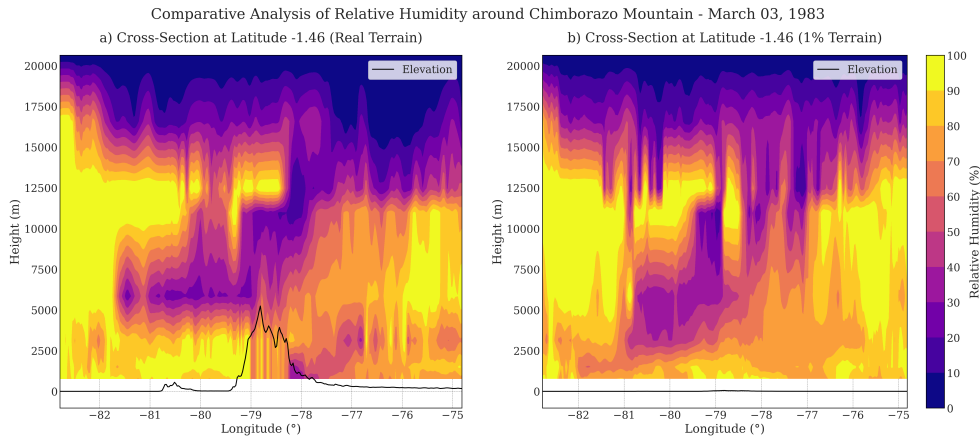


Figure 3.39: Vertical cross section comparison of Relative Humidity at Chimborazo Mountain - March 24, 1983

Cross Section: Weak El Niño Events (February 16, 2007)

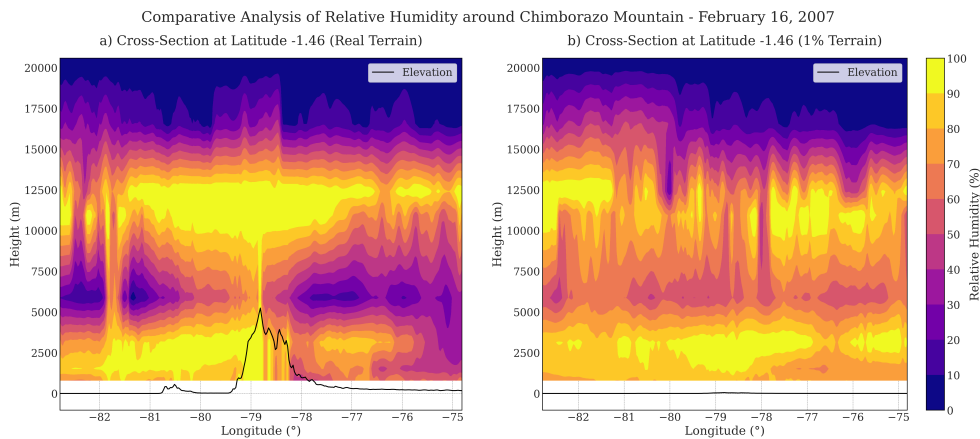


Figure 3.40: Vertical cross-section comparison of relative humidity at Chimborazo Mountain - Feb 16, 2007 (Real terrain vs 1% of the terrain)

Real Terrain (Cross section a) Below 5,000 meters, there are high relative humidity values (between $\sim 80\%$ - 100%) on the windward side of the mountain. This is due to the orographic lifting of moist air masses from the Amazon basin, which are forced upward by the mountain, cooling adiabatically and reaching saturation. The windward side experiences the highest humidity levels, while the leeward side shows slightly lower humidity

due to the rain shadow effect. Between 5,000 and 15,000 meters, the relative humidity exhibits considerable variability. As the moist air continues to rise, it creates regions of high humidity mixed with lower humidity zones due to turbulent mixing and varying wind speeds. Above 15,000 meters, relative humidity generally decreases, and the variability reduces.

1% Terrain (Cross section b) Lower altitudes display a smoother gradient of relative humidity, with moderate levels ($\sim 50\%$ and $\sim 70\%$), lacking the sharp gradients seen in the real terrain profile. From 5,000 to 15,000 meters, the relative humidity remains relatively consistent, with fewer disruptions and more even distribution, highlighted by continuous bands of yellow and orange. Above 15,000 meters, the relative humidity shows minimal variability.

3.4.2 Relative Humidity: Strong vs Weak La Niña Analysis

The analysis of relative humidity at 850 hPa, focuses on the differences between real terrain and 1% terrain scenarios during strong and weak La Niña events (figure 3.41).

Strong La Niña Events (November 06, 1998) - Maps at 850 hPa

- **Real Terrain:** In the real terrain, Ecuador experiences significant variations in relative humidity. The color gradient ranges from purple (0%) to yellow (100%), and much of the country shows moderate to high humidity ($\sim 60\%$ to $\sim 80\%$) in the western regions, including the Pacific coastal areas and the west Andes slopes. These areas exhibit orange and yellow hues, indicating elevated humidity levels driven by moisture from the Pacific Ocean. In contrast, the Amazon basin and the eastern parts of Ecuador show lower humidity ($\sim 20\%$ to $\sim 40\%$), indicated by purple and blue shades. The topographic barrier created by the Andes limits the eastward flow of moisture, leading to drier conditions in these regions during the strong La Niña phase.
- **1% Terrain Height:** The image shows a noticeable decrease in relative humidity over Ecuador, particularly along the Andean region. The previously humid western Andes and coastal areas now exhibit lower humidity ($\sim 20\%$ to $\sim 40\%$), as represented by blue and purple hues. The removal of the orographic effect significantly reduces the ability of the terrain to trap moisture, leading to drier conditions throughout the region. Without the mountains, the airflow dynamics are altered, and much of the moisture that would have been captured on the western slopes is lost, resulting in a marked reduction in humidity.
- **Difference between the real terrain map and the 1% terrain map:** Red areas indicate regions where relative humidity is lower in the flattened terrain scenario, while green areas represent regions where relative humidity is higher. Over Ecuador, the western Andes and coastal areas experience a significant drop in humidity, with reductions of up to $\sim 40\%$ or more, shown in red. The absence of the Andes' orographic effect leads to a substantial decline in moisture over these regions. The

eastern regions, particularly the Amazon basin, show minimal change, as indicated by green and white areas, suggesting that the Andes' role in regulating humidity is more pronounced on the western side of the range during strong La Niña events.

Comparative Analysis of Relative Humidity

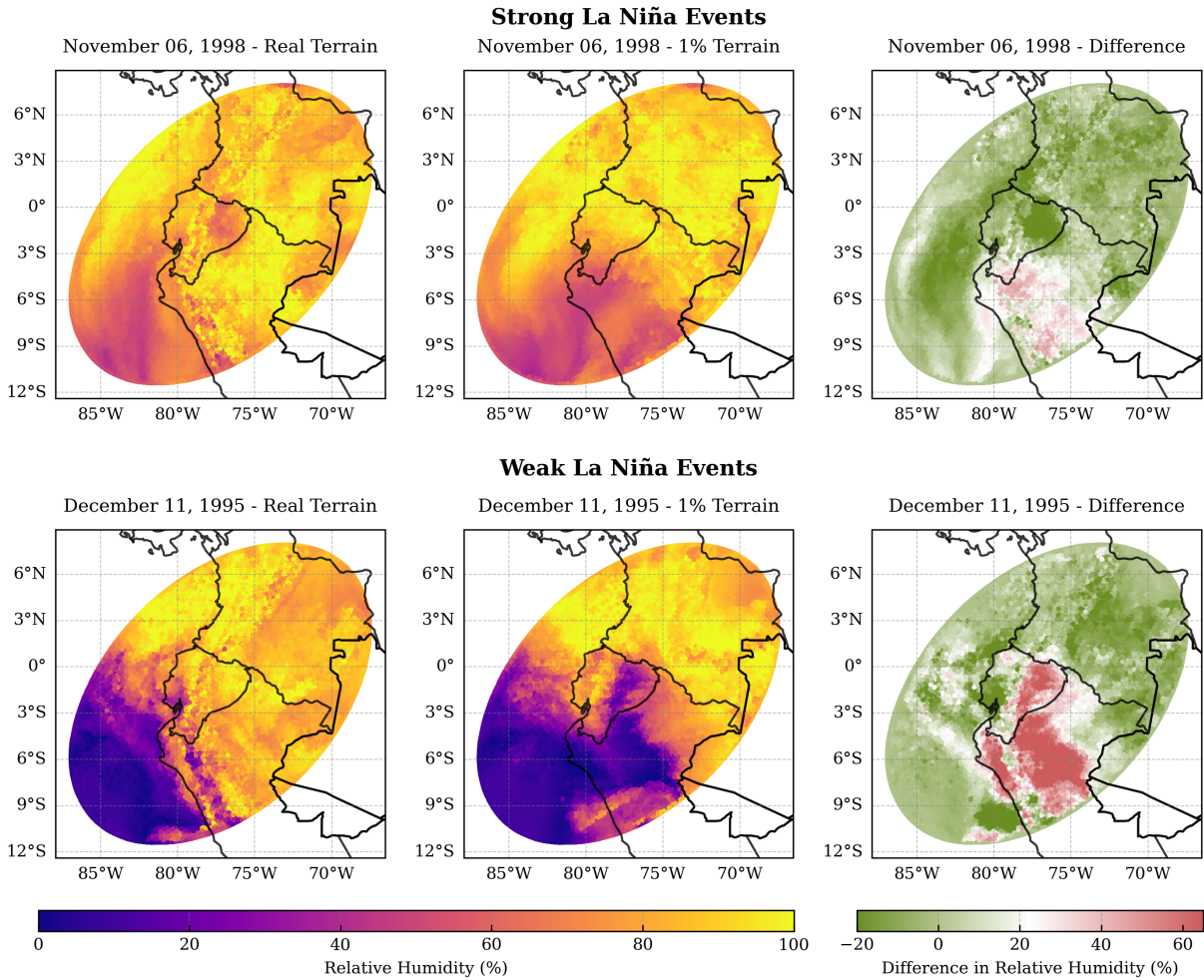


Figure 3.41: Comparative Analysis of Relative Humidity at 850hPa - Strong and Weak La Niña Events (Real terrain vs 1% terrain)

Weak La Niña Events (December 11, 1995) - Maps at 850 hPa

- Real Terrain:** The overall humidity levels across Ecuador are lower compared to the strong La Niña event. The image shows more purple and blue areas, particularly in the eastern regions and parts of the Amazon basin, where humidity levels drop to $\sim 20\%$ or below. The western slopes of the Andes and the coastal region still maintain moderate humidity levels ($\sim 60\%$ to $\sim 80\%$), indicated by orange and yellow hues, but these values are notably lower than during the strong La Niña event. The Andes continue to influence moisture retention on the windward side, but the overall atmospheric moisture is reduced during this weaker La Niña phase, leading to drier conditions in Ecuador, especially in the eastern part of the country.

- **1% Terrain Height:** When the terrain is flattened, the reduction in relative humidity is less dramatic than in the strong La Niña case, but still significant. The Andean region and western Ecuador show lower humidity (ranging from $\sim 20\%$ to $\sim 40\%$), represented by purple and blue shades. The Amazon basin and eastern Ecuador remain relatively dry, with humidity levels continuing to range from 0% to $\sim 40\%$. This suggests that the orographic effect of the Andes is still important, but the overall atmospheric moisture availability is lower during weak La Niña events, making the influence of terrain modification less pronounced.
- **Difference between the real terrain map and the 1% terrain map:** Red areas indicate a decrease in relative humidity, while green areas show regions where humidity increases. The western Andes and coastal regions of Ecuador exhibit a decrease in humidity, with reductions up to 20% . Compared to the strong La Niña event, the changes in relative humidity are smaller, reflecting the weaker influence of terrain during this climatic phase. The green areas in the Amazon basin suggest slight increases in humidity in the flattened scenario, indicating that moisture distribution becomes more uniform without the Andes' orographic effect. However, the overall differences are less pronounced during this weak La Niña event, reinforcing the idea that topography plays a more substantial role during strong La Niña events.

Cross Section: Strong La Niña Events (November 06, 1998)

Real Terrain (Cross section a) At lower altitudes (0 - $5,000$ meters), the humidity levels are near 100% , and they are concentrated on the windward side of the mountain. The leeward side, however, shows much lower humidity levels (10 - 30%). Between altitudes of $5,000$ to $15,000$ meters, the varying yellow and purple bands indicate areas of concentrated moisture and drier regions, respectively, and above $15,000$ meters, the relative humidity levels become more uniform, as indicated by the predominant purple and blue shades, reflecting lower humidity.

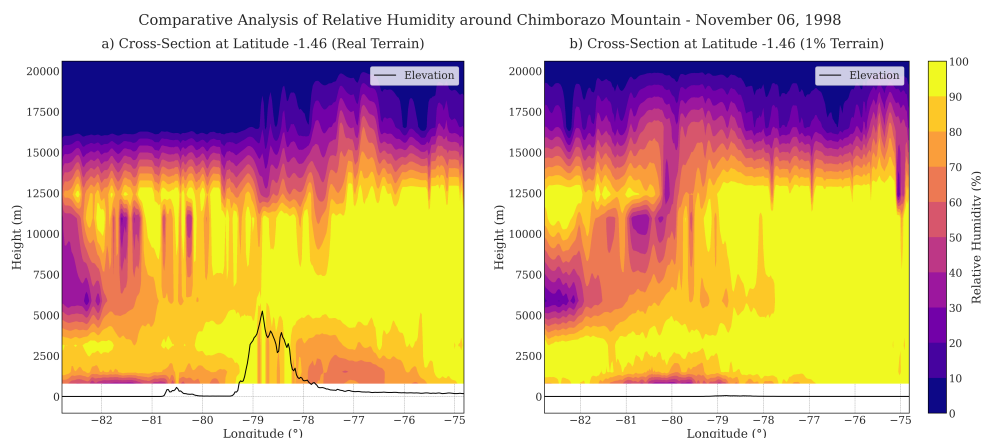


Figure 3.42: Vertical cross-section comparison of relative humidity at Chimborazo Mountain - Nov 06, 1998 (Real terrain vs 1% of the terrain)

1% Terrain (Cross section b) At lower altitudes, the absence of significant topographic features results in smoother gradients, with the majority of the area showing moderate humidity levels around $\sim 50\%$ to $\sim 70\%$. Between 5,000 and 15,000 meters, the humidity distribution is more consistent, lacking the variability seen in the real terrain scenario, and above 15,000 meters, the relative humidity levels continue to be more consistent.

Cross Section: Weak El Niño Events (December 11, 1995)

Real Terrain (Cross section a) At lower altitudes (0-5,000 meters), high relative humidity is present on the windward side of the mountain, with values close to 100%, while the leeward side shows much lower humidity levels ($\sim 10\%$ to $\sim 30\%$), shown by blue and purple hues. Between altitudes of 5,000 and 15,000 meters, there are alternating bands of high and low humidity, reflecting complex interactions between air masses and the mountainous terrain. Above 15,000 meters, the relative humidity becomes more uniform.

1% Terrain (Cross section b) The absence of significant topographic features results in a smoother gradient, with the majority of the area showing moderate humidity levels around $\sim 50\%$ to $\sim 70\%$. From 5,000 to 15,000 meters, the humidity distribution is more consistent, lacking the variability seen in the real terrain scenario. Above 15,000 meters, relative humidity levels remain fairly uniform.

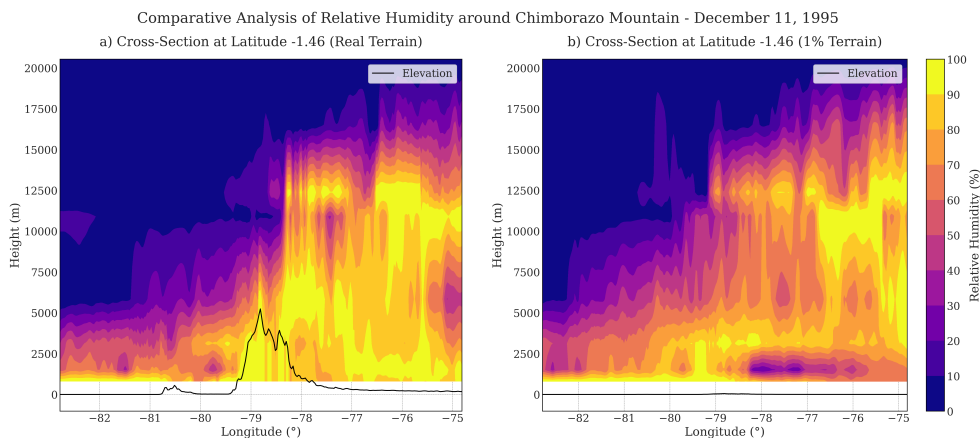


Figure 3.43: Vertical cross-section comparison of relative humidity at Chimborazo Mountain - Dec 11, 1995 (Real terrain vs 1% of the terrain)

It is clear that the Andes act as a barrier to the transport of moisture from the Amazon basin to the coastal areas. When the Andes are included, high humidity regions form on the eastern windward side due to orographic lifting, which forces moist air from the Amazon basin to rise, cool, and condense. This creates high humidity on the eastern side and much drier conditions on the western leeward side, effectively blocking moisture transport to coastal areas. When the terrain is minimized, this barrier effect is less pronounced, leading to a more uniform humidity distribution across the region.

3.4.3 Overall relative humidity observations

- El Niño and La Niña events exhibit distinct differences in how they affect atmospheric moisture, particularly in relation to the Andes mountains. During El Niño, especially in strong phases, the warmer Pacific sea surface temperatures (SSTs) lead to significantly increased moisture transport, resulting in higher relative humidity across Ecuador. This is particularly evident along the western slopes of the Andes and coastal areas, where humidity can exceed 80%. The orographic effect of the Andes is critical in trapping this moisture. When the terrain is flattened (as seen in the 1% terrain simulations), there is a substantial drop in relative humidity, demonstrating the key role of mountains in maintaining moisture during these events.
- In contrast, La Niña events bring cooler SSTs, resulting in drier conditions and lower overall humidity, with values generally between $\sim 40\%$ and $\sim 80\%$. The impact of the Andes on moisture retention is still noticeable but less pronounced, given the already reduced atmospheric moisture. Flattening the Andes during La Niña results in smaller changes in humidity compared to El Niño, indicating that the orographic influence is less significant during these cooler phases. In summary, El Niño amplifies the moisture-trapping effect of the Andes, whereas La Niña events produce a drier atmosphere with less terrain-induced variation in humidity.

3.4.4 Precipitation: Strong vs Weak El Niño Analysis

The analysis of precipitation during strong and weak El Niño events shows notable differences in rainfall distribution over Ecuador. Strong events are characterized by distinct precipitation patterns, with anomalies more concentrated in certain regions, while weak events exhibit more subtle variations. These results are presented in Figure 3.44, setting the foundation for a detailed comparison of how the intensity of El Niño influences precipitation.

Strong El Niño Events (March 24, 1983) - Maps at 850 hPa

- **Real Terrain:** Along the northern region, precipitation levels range from moderate to high (especially along the coast) with values between ~ 30 mm and ~ 70 mm. The plot shows that eastern slopes of the Andes receive more precipitation.
- **1% Terrain Height:** An overall similar pattern is observed. The coastal and eastern Andean regions still show significant precipitation. Variations in distribution highlight the increase in precipitation in northern Ecuador.
- **Difference between the real terrain map and the 1% terrain map:** The difference map indicates areas with precipitation changes, where white areas indicate no change blue shades denote an increase in precipitation values, and red zones a decrease. Areas of increased precipitation are mainly concentrated along the eastern slopes of the Andes and zones located in the north of Ecuador. Zones of decreased precipitation are also visible scattered along the coast and less intense in the western slopes.

Comparative Analysis of Precipitation

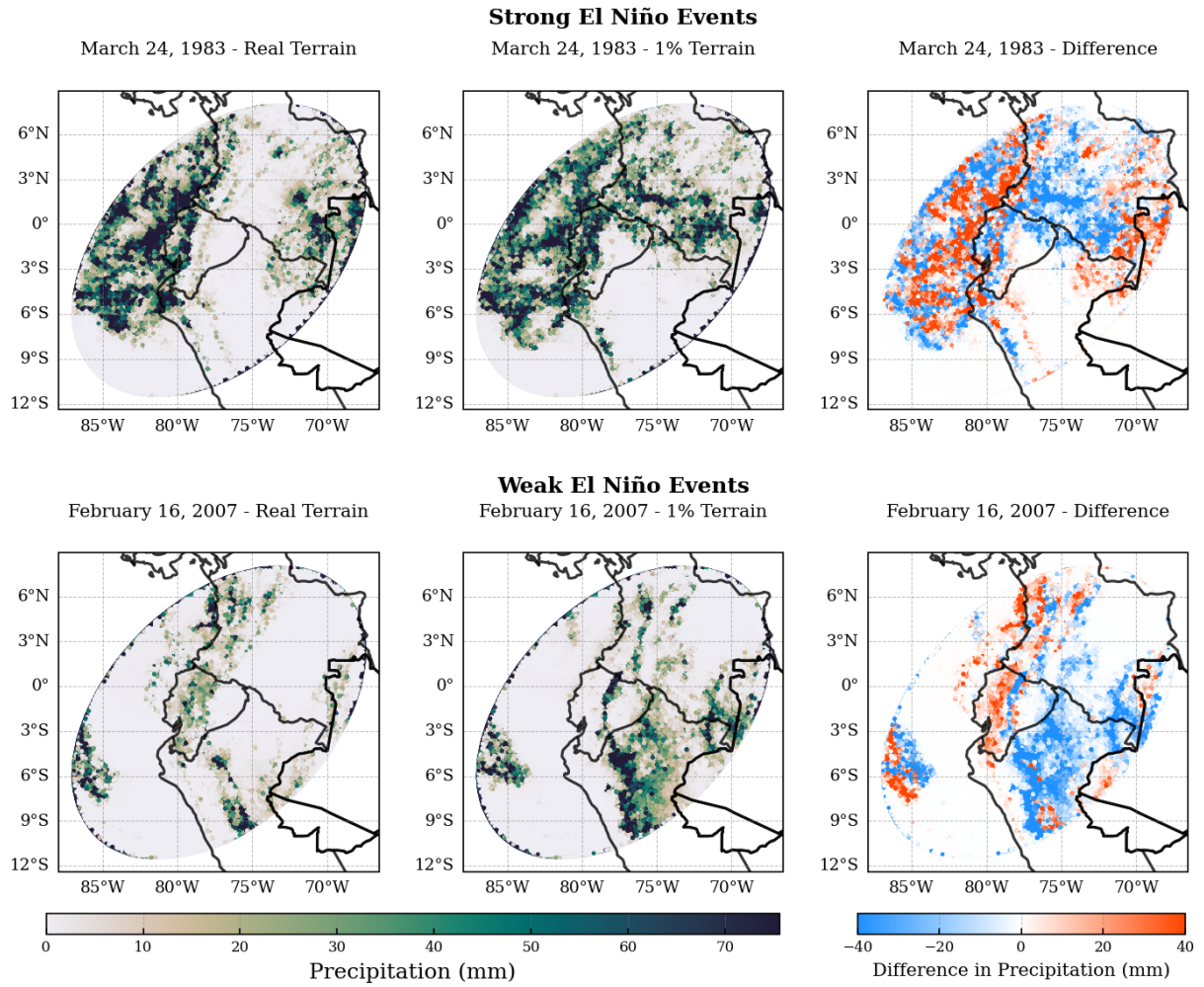


Figure 3.44: Comparative Analysis of Precipitation - Strong and Weak El Niño Events (Real terrain vs 1% of the terrain)

Weak El Niño Events (February 16, 2007) - Maps at 850 hPa

- **Real Terrain:** The plot indicates lower overall precipitation compared to strong El Niño events. Eastern slopes and coastal regions still receive notable rainfall, but the intensity is less (~ 40 mm).
- **1% Terrain Height:** In this map, less spatial distribution of precipitation across the country is observed.
- **Difference between the real terrain map and the 1% terrain map:** Reductions in precipitation values are observed in the eastern and western foothills of the Andes, and some minor decreases along the Coastal region. Significant increases are observed across the eastern Andes in Ecuador and notable ones in the amazon region.

3.4.5 Precipitation: Strong vs Weak La Niña Analysis

The precipitation analysis during strong and weak La Niña events reveals important variations across Ecuador. Strong La Niña events show more concentrated and intense rainfall anomalies, while weak events produce more moderate shifts in precipitation patterns. Figure 3.45 presents these initial results, highlighting the influence of La Niña intensity on regional rainfall distribution.

Strong La Niña Events (November 06, 1998) - Maps at 850 hPa

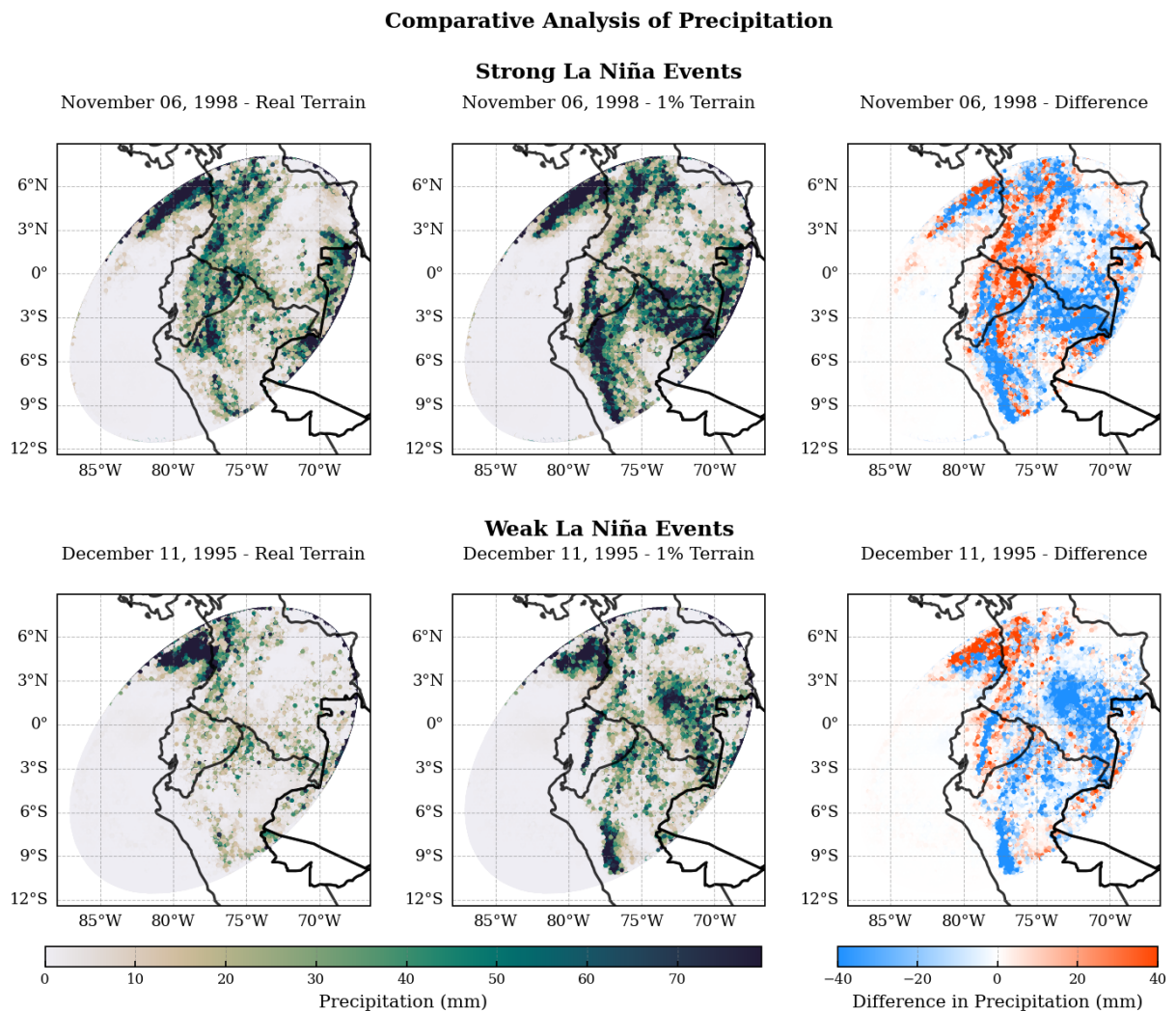


Figure 3.45: Comparative Analysis of Precipitation - Strong and Weak La Niña Events (Real terrain vs 1% of the terrain)

- **Real Terrain:** The eastern slopes of the Andes and the Amazon region show high precipitation levels (up to ~ 70 mm), while the coastal areas indicate very low precipitation

- **1% Terrain Height:** The eastern slopes still show greater moisture uptake, but with differences in distribution and intensity
- **Difference between the real terrain map and the 1% terrain map:** The plot shows considerable reduction (red areas) in the eastern and western foothills of the Andes extending to the Amazon region. The coastal region shows minor decreases in precipitation, and notable increases are observed in the eastern Andes and also the southeast areas.

Weak La Niña Events (December 11, 1995) - Maps at 850 hPa

- **Real Terrain:** The precipitation is moderate along the Andean region. The highest precipitation areas (up to $\sim 45\text{mm}$) are the slopes of the Andes and the east regions of the Amazon.
- **1% Terrain Height:** Precipitation is uniformly lower across Ecuador. The plot shows an increase in precipitation in the Andean regions and more dispersion in the Amazon.
- **Difference between the real terrain map and the 1% terrain map:** The plot displays mixed changes, Significant increases in the eastern Andes and in parts of central and southern Ecuador and the Amazon region also shows notable increases, indicating that air uplift and moisture convergence in these zones are affected by topographic changes.

3.4.6 Overall precipitation observations

- The Andes Mountains affect precipitation patterns in Ecuador. Both strong El Niño and La Niña events exhibit moderate to high-intensity precipitation specially on the eastern slopes of the Andes and the Amazon region.
- Strong El Niño event shows extreme precipitation in the coastal areas compared to the strong La Niña.
- Simulations with 1% height in show slight differences in precipitation distribution, but the general pattern remains.

Chapter 4

Conclusions

This research has provided a comprehensive analysis of the winds that influence Ecuador, considering the presence of the Ecuadorian Andes using the Model for Prediction Across Scales (MPAS). We conducted simulations in four different scenarios of mountain heights – the actual height, half the height, 10% of the height, and 1% of the height – we have gained valuable insights into the complex interactions between topography and wind patterns. Furthermore, our study included an examination of real humidity conditions and precipitation, as well as an analysis of the impacts on the El Niño and La Niña phenomena. The main findings of our research are summarized below:

- (i) *On wind patterns:* The Andes profoundly alter the regional wind dynamics by acting as a physical barrier that deflects and redirects atmospheric flow. Their elevation influences wind speed and direction. During normal conditions, easterly winds strengthen over the Amazon basin, while westerly winds are diverted along the western slopes. These effects are particularly evident when comparing scenarios with reduced Andes height, where wind patterns become less variable. Coastal regions, Andean slopes, and the Amazon basin experience the greatest impact from these modifications.
- (ii) *On relative humidity during El Niño and La Niña Events:* The Andes shape regional humidity gradients by blocking and redistributing moisture transport between the Amazon basin and the Pacific. Moist air from the east is forced to rise along the eastern slopes, creating high humidity levels and fostering cloud formation and rainfall. On the western slopes, the rain shadow effect leads to much drier conditions. These patterns are highly sensitive to climatic events such as El Niño and La Niña. For instance, during El Niño, westerly winds intensify, carrying moisture to the western Andes, while La Niña enhances easterly moisture transport, increasing humidity along the eastern slopes. This barrier effect is evident in vertical cross sections and maps, showing the critical role of the Andes in regional climate dynamics.
- (iii) *On precipitation during El Niño and La Niña Events:* The topography of the Andes directly governs spatial and temporal variability in precipitation, with elevation driving substantial rainfall differences. Orographic lifting causes enhanced precipitation over mountainous regions, particularly along the eastern slopes, where the moisture

from the Amazon converges and increases. During El Nio events, the western Andes and coastal areas experience increased rainfall due to a stronger westerly flow. In contrast, La Nia conditions redirect precipitation patterns, increasing rainfall in the eastern Andes and the Amazon basin. This redistribution of rainfall is crucial for understanding regional hydrology, agriculture, and ecosystems, as it underscores the role of the Andes in determining where and when water resources are available.

Although this study offers significant insights, it is subject to certain limitations. The simulations are constrained by the resolution and parameterization of the model. Variations in model accuracy and the simplifications in representing topography might compromise the precision of the results. Moreover, the research concentrates mainly on wind patterns, relative humidity, and precipitation, while other climatic variables like temperature and cloud cover could offer additional insights into the impact of the Andes Mountains. To address these limitations and build on the research findings, the following recommendations are proposed:

- (i) Future studies should use higher-resolution models and if possible, more detailed topographic data to better capture regional atmospheric dynamics and improve accuracy.
- (ii) Including additional climatic variables could provide a more comprehensive understanding.
- (iii) Implementing long-term observational studies to validate simulation results.
- (iv) Incorporating findings into climate policies and management can help address the impacts of topographic influences on key sectors, including agriculture and water resources.

Bibliography

- [1] UXarray Organization, “UXarray (version 0.0.2),” 2021, [Software].
- [2] S. Hoyer and H. Joseph, “xarray: N-D labeled Arrays and Datasets in Python,” *Journal of Open Research Software*, vol. 5, no. 1, Apr. 2017.
- [3] J. D. Hunter, “Matplotlib: A 2d graphics environment,” *Computing in Science & Engineering*, vol. 9, no. 3, pp. 90–95, 2007.
- [4] Grammarly Inc., “Grammarly,” <https://www.grammarly.com>, 2024, [Software].
- [5] GGWeather. (2024) Oceanic niño index (oni). [Online]. Available: <https://ggweather.com/enso/oni.htm>
- [6] C. A. Valle and F. Cruz, “The impact of the 1982-1983 el niño-southern oscillation on seabirds in the galapagos islands, ecuador,” *Journal of Geophysical Research: Atmospheres*, vol. 92, pp. 14 437–14 452, 1987. [Online]. Available: <https://agupubs.onlinelibrary.wiley.com/doi/10.1029/JC092iC13p14437>
- [7] UNDP. (2000) Economic and social effects of el niño in ecuador, 1997-1998. [Online]. Available: <https://webimages.iadb.org/publications/english/document/Economic-and-Social-Effects-of-El-Ni%C3%B1o-in-Ecuador-1997-1998.pdf>
- [8] CAF, “Evolución, vulnerabilidad e impactos económicos y sociales de el niño 2015-2016 en ecuador,” *Investigaciones Geográficas*, vol. 68, pp. 99–116, 2017. [Online]. Available: <https://www.investigacionesgeograficas.com/article/view/2017-n68-impactos-socioeconomicos-y-sociales-de-el-nino-2015-201>
- [9] F. Rossel and E. Cadier, “El niño and prediction of anomalous monthly rainfalls in ecuador,” *Hydrological Processes*, vol. 23, no. 23, pp. 3253–3260, 2009. [Online]. Available: https://www.researchgate.net/publication/229629382_El_Nino_and_prediction_of_anomalous_monthly_rainfalls_in_Ecuador
- [10] Redalyc. (2011) El niño en la región andina: Impactos y repuestas en el ecuador. [Online]. Available: <https://www.redalyc.org/pdf/126/12627315.pdf>
- [11] NOAA. (2024) Climate variability: Oceanic niño index. [Online]. Available: <http://www.climate.gov/news-features/understanding-climate/climate-variability-oceanic-nino-index>

- [12] J. Boulanger, C. Menkes, and M. Lengaigne. (2000) Les phases el niño et la niña du phénomène enso et leur impact sur la variabilité climatique de l'Équateur. [Online]. Available: https://horizon.documentation.ird.fr/exl-doc/pleins_textes/pleins_textes_7/carton03/010021323.pdf
- [13] EIRD. (2004) Los efectos de el niño en ecuador. [Online]. Available: <https://www.eird.org/estrategias/pdf/spa/doc12863/doc12863-10.pdf>
- [14] IDB. (2000) Economic and social effects of el niño in ecuador, 1997-1998. [Online]. Available: <https://webimages.iadb.org/publications/english/document/Economic-and-Social-Effects-of-El-Ni%C3%B1o-in-Ecuador-1997-1998.pdf>
- [15] Investigaciones Geográficas. (2017) Impactos socioeconómicos y sociales de el niño 2015-2016. [Online]. Available: <https://www.investigacionesgeograficas.com/article/view/2017-n68-impactos-socioeconomicos-y-sociales-de-el-nino-2015-201>
- [16] E. Ortiz-Prado, P. S. Espinosa, A. Borrero, S. P. Cordovez, J. E. Vasconez, A. Barreto-Grimalas, M.-C. Alemida, A. R. Henriquez-Trujillo, K. Simbaña-Rivera, L. Gomez-Barreno, G. Viscor, and P. Roderick, “Stroke-related mortality at different altitudes: A 17-year nationwide population-based analysis from ecuador,” *Frontiers in Physiology*, vol. 12, p. 733928, 2021. [Online]. Available: <https://www.frontiersin.org/articles/10.3389/fphys.2021.733928/full>
- [17] Los Alamos National Laboratory (COSIM) and National Center for Atmospheric Research (NCAR). Model for prediction across scales (mpas). [Online]. Available: <https://mpas-dev.github.io/>
- [18] S. Giralt, A. Moreno, R. Bao, A. Sáez, B. Valero, J. Pueyo, B. Klosowska, A. Hernández, P. González-Sampériz, and C. Taberner, “The history of the el niño - southern oscillation according to lacustrine and marine sediments,” *Contributions to Science*, vol. 3, no. 3, pp. 343–353, 2007. [Online]. Available: https://www.researchgate.net/publication/29495165_The_History_of_the_El_Nino_-_Southern_Oscillation_according_to_lacustrine_and_marine_sediments
- [19] M. D. Team, *MPAS Atmosphere User's Guide*, 2023. [Online]. Available: <https://mpas-dev.github.io/atmosphere/>
- [20] C. D. Ahrens, *Meteorology today: an introduction to weather, climate, and the environment*. Cengage Learning Canada Inc., 2015. [Online]. Available: https://www.google.com/books/edition/Meteorology_Today/jZo78yb5MIMJ?hl=en&gbpv=1&printsec=frontcover
- [21] S. Strauss and B. S. Orlove, *Weather, climate, culture*. Routledge, 2021. [Online]. Available: <https://books.google.com/books?hl=en&lr=&id=MmA4EAAAQBAJ&oi=fnd&pg=PT6&dq=climate+describes+the+long-term+average+of+weather+patterns+over+extended+periods&ots=6OBfyLEMPY&sig=96oHqAeUm7oZXo2ADQqmKopFHRQ>
- [22] J. M. Wallace and P. V. Hobbs, *Atmospheric Science: An Introductory Survey*, 2nd ed. Academic Press, 2006.

- [23] I. P. on Climate Change (IPCC), “Climate change 2021: The physical science basis. contribution of working group i to the sixth assessment report of the intergovernmental panel on climate change,” *Cambridge University Press*, 2021.
- [24] J. Hansen, M. Sato, and R. Ruedy, “Perception of climate change,” *Proceedings of the National Academy of Sciences*, vol. 109, no. 37, pp. E2415–E2423, 2013.
- [25] N. R. Council, *Advancing the Science of Climate Change*. The National Academies Press, 2010.
- [26] E. Kalnay, M. Kanamitsu, R. Kistler, W. Collins, D. Deaven, L. Gandin, and M. Saha, “The ncep/ncar 40-year reanalysis project,” *Bulletin of the American Meteorological Society*, vol. 77, no. 3, pp. 437–471, 1996.
- [27] M. Ghil and P. Malanotte-Rizzoli, “Data assimilation in meteorology and oceanography,” *Advances in Geophysics*, vol. 33, pp. 141–266, 1991.
- [28] K. E. Trenberth, “The changing flow of energy through the climate system,” *Climate Research*, vol. 74, no. 3, pp. 197–209, 2018.
- [29] R. D. Garreaud, M. Vuille, and A. C. Clement, “The climate of the altiplano: observed current conditions and mechanisms of past changes,” *Palaeogeography, Palaeoclimatology, Palaeoecology*, vol. 194, no. 1-3, pp. 5–22, 2003.
- [30] M. Falvey and R. D. Garreaud, “Wintertime precipitation episodes in central chile: Associated meteorological conditions and orographic influences,” *Journal of Hydrometeorology*, vol. 8, no. 2, pp. 171–193, 2007.
- [31] M. Vuille, R. S. Bradley, M. Werner, F. Keimig, and H. F. Diaz, “20th century climate change in the tropical andes: Observations and model results,” *Climatic Change*, vol. 59, no. 1-2, pp. 75–99, 2008.
- [32] M. Vuille, R. S. Bradley, and F. Keimig, “Interannual climate variability in the central andes and their relation to tropical pacific and atlantic forcing,” *Journal of Geophysical Research: Atmospheres*, vol. 105, no. D10, pp. 12 447–12 460, 2000.
- [33] R. Rollenbeck and J. Bendix, “Rainfall distribution in the andes of southern ecuador derived from blending weather radar data and meteorological field observations,” *Atmospheric Research*, vol. 99, no. 2, pp. 277–289, 2011.
- [34] R. E. Villar, J. Ronchail, J.-L. Guyot, G. Cochonneau, F. Naziano, W. Lavado, and R. Pombosa, “Spatio-temporal rainfall variability in the amazon basin countries (brazil, peru, bolivia, colombia, and ecuador),” *International Journal of Climatology*, vol. 29, no. 11, pp. 1574–1594, 2015.
- [35] D. Camuffo, *Microclimate for Cultural Heritage*, 3rd ed. Elsevier, 2021.
- [36] P. Crespo, J. Feyen, P. Vauchel, A. Bückler, L. Breuer, H.-G. Frede, and F. Cisneros, “Identification of runoff processes in a small andean catchment and implications for the ecohydrological modeling of tropical montane cloud forests,” *Hydrology and Earth System Sciences*, vol. 15, no. 8, pp. 2479–2494, 2011.

- [37] E. Moran-Tejeda and T. Ochoa, “Hydroclimatic variability in the ecuadorian andes: An overview,” *Advances in Meteorology*, vol. 2016, pp. 1–17, 2016.
- [38] A. Ochoa and R. Pineda, “Precipitation distribution patterns in the andean region of ecuador,” *Journal of Hydrology*, vol. 519, pp. 2186–2201, 2014.
- [39] F. Porté-Agel, C. Meneveau, and M. Parlange, “A scale-dependent dynamic model for large-eddy simulation: application to a neutral atmospheric boundary layer,” *Journal of Fluid Mechanics*, vol. 415, pp. 261–284, 2000.
- [40] R. Devulapalli, N. Peterson, and J. Carlsson, *Data Visualization Using Weighted Voronoi Diagrams*, 01 2015, pp. 181–203.
- [41] T. Ringler, L. Ju, and M. Gunzburger, “A multiresolution method for climate system modeling: application of spherical centroidal voronoi tessellations,” *Ocean Dynamics*, vol. 58, pp. 475–498, 2008.
- [42] D. Heinzeller, M. Duda, and H. Kunstmann, “Towards convection-resolving, global atmospheric simulations with the model for prediction across scales (mpas) v3.1: an extreme scaling experiment,” *Geoscientific Model Development*, vol. 9, pp. 77–110, 2015.
- [43] M. Fox-Rabinovitz, “Computational dispersion properties of 3d staggered grids for a nonhydrostatic anelastic system,” *Monthly Weather Review*, vol. 124, pp. 498–510, 1996.
- [44] S. Saha, S. Moorthi, H. L. Pan, X. Wu, J. Wang, S. Nadiga, P. Tripp, R. Kistler, J. Woollen, D. Behringer, H. Liu, D. Stokes, R. Grumbine, G. Gayno, J. Wang, Y.-T. Hou, H.-Y. Chuang, H.-M. H. Juang, J. Sela, M. Iredell, R. Treadon, D. Kleist, P. V. Delst, D. Keyser, J. Derber, M. Ek, J. Meng, H. Wei, R. Yang, S. Lord, H. van den Dool, A. Kumar, W. Wang, C. Long, and M. Chelliah, “The ncep climate forecast system reanalysis,” *Bulletin of the American Meteorological Society*, vol. 91, no. 8, pp. 1015–1057, 2010.
- [45] S. Saha, S. Moorthi, X. Wu, J. Wang, S. Nadiga, P. Tripp, R. Kistler, J. Woollen, D. Behringer, H. Liu, D. Stokes, R. Grumbine, G. Gayno, J. Wang, Y.-T. Hou, H.-Y. Chuang, H.-M. H. Juang, J. Sela, M. Iredell, R. Treadon, D. Kleist, P. V. Delst, D. Keyser, J. Derber, M. Ek, J. Meng, H. Wei, R. Yang, S. Lord, H. van den Dool, A. Kumar, W. Wang, C. Long, and M. Chelliah, “The ncep climate forecast system version 2,” *Journal of Climate*, vol. 27, pp. 2185–2208, 2014.
- [46] X. Liang, M. Xu, W. Gao, K. Kunkel, J. Slusser, Y. Dai, Q. Min, P. Houser, M. Rodell, C. Schaaf, and F. Gao, “Development of land surface albedo parameterization based on moderate resolution imaging spectroradiometer (modis) data,” *Journal of Geophysical Research: Atmospheres*, vol. 110, 2005.
- [47] J. J. Danielson and D. B. Gesch, “Global multi-resolution terrain elevation data 2010 (gmted2010),” U.S. Geological Survey, Open-File Report 2011-1073, 2011. [Online]. Available: <https://pubs.usgs.gov/of/2011/1073/pdf/of2011-1073.pdf>

- [48] K. E. Trenberth, “The definition of el niño,” *Bulletin of the American Meteorological Society*, vol. 78, no. 12, pp. 2771–2777, 1997.
- [49] M. H. Glantz, *Currents of Change: Impacts of El Niño and La Niña on Climate and Society*. Cambridge University Press, 2001.
- [50] K. E. Trenberth and T. J. Hoar, “El niño and climate change,” *Geophysical Research Letters*, vol. 24, no. 23, pp. 3057–3060, 1997.
- [51] G. Poveda and O. J. Mesa, “Feedbacks between hydrological processes in tropical south america and large-scale ocean–atmospheric phenomena,” *Journal of Climate*, vol. 10, no. 10, pp. 2690–2702, 1997.
- [52] J. Bendix, K. Trachte, E. Palacios, R. Rollenbeck, D. Göttlicher, T. Naus, and A. Bendix, “El niño meets la niña – anomalous rainfall patterns in the “traditional” el niño region of southern ecuador,” *Erdkunde*, vol. 65, pp. 151–167, 06 2011.
- [53] S. Marjani, O. Alizadeh, and P. Irannejad, “Frequency of extreme el niño and la niña events under global warming,” *Climate Dynamics*, vol. 53, 11 2019.
- [54] S. Vicente-Serrano, E. Aguilar, R. Martinez, N. Martín-Hernández, C. Azorin-Molina, A. Sanchez-Lorenzo, A. Kenawy, M. Tomas-Burguera, E. Morán-Tejeda, J. López-Moreno, J. Revuelto, S. Beguería, J. Nieto, A. Drumond, L. Gimeno, and R. Nieto, “The complex influence of enso on droughts in ecuador,” *Climate Dynamics*, vol. 48, 01 2017.
- [55] NOAA. Monitoring & data: Ocean niño index changes description. [Online]. Available: https://www.cpc.ncep.noaa.gov/products/analysis_monitoring/ensostuff/ONI_change.shtml
- [56] WMO. El niño / la niña. [Online]. Available: <https://wmo.int/topics/el-nino-la-nina>
- [57] NOAA. Forecasting el niño and la niña. [Online]. Available: <https://oceanoday.noaa.gov/observingelnino/>
- [58] NASA. Overview | el niño/la niña watch & pdo. [Online]. Available: <https://sealevel.jpl.nasa.gov/data/el-nino-la-nina-watch-and-pdo/overview/>
- [59] W. C. Skamarock, J. B. Klemp, J. Dudhia, D. O. Gill, D. M. Barker, M. G. Duda, X.-Y. Huang, W. Wang, and J. G. Powers, “A description of the advanced research wrf version 3,” NCAR Technical Note-475+ STR, Tech. Rep., 2008. [Online]. Available: <https://doi.org/10.5065/D68S4MVH>
- [60] C. S. Zender, *NCO: NetCDF Operators*, 2024. [Online]. Available: <http://nco.sourceforge.net/>
- [61] U. Schulzweida, *CDO User Guide: Climate Data Operators*, Max Planck Institute for Meteorology, 2024. [Online]. Available: <https://code.mpimet.mpg.de/projects/cdo>

- [62] WRF-ARW Development Team, *Weather Research and Forecasting (WRF) Model: Preprocessing System (WPS)*, National Center for Atmospheric Research (NCAR), 2024. [Online]. Available: https://www2.mmm.ucar.edu/wrf/users/docs/user_guide_v4/v4.3/users_guide_chap3.html
- [63] L. Fowler, W. Skamarock, G. Grell, S. Freitas, and M. Duda, “Analyzing the grell–freitas convection scheme from hydrostatic to nonhydrostatic scales within a global model,” *Monthly Weather Review*, vol. 144, pp. 2285–2306, 2016.
- [64] G. Thompson, P. R. Field, R. M. Rasmussen, and W. D. Hall, “Explicit forecasts of winter precipitation using an improved bulk microphysics scheme. part ii: Implementation of a new snow parameterization,” *Monthly Weather Review*, vol. 136, no. 12, pp. 5095–5115, 2008. [Online]. Available: <https://doi.org/10.1175/2008MWR2387.1>
- [65] M. J. Iacono, J. S. Delamere, E. J. Mlawer, M. W. Shephard, S. A. Clough, and W. D. Collins, “Radiative forcing by long-lived greenhouse gases: Calculations with the aer radiative transfer models,” *Journal of Geophysical Research: Atmospheres*, vol. 113, no. D13, 2008. [Online]. Available: <https://doi.org/10.1029/2008JD009944>
- [66] G.-Y. Niu, Z.-L. Yang, K. E. Mitchell, F. Chen, M. B. Ek, M. Barlage, ..., and Y. Xia, “The community noah land surface model with multiparameterization options (noah-mp): 1. model description and evaluation with local-scale measurements,” *Journal of Geophysical Research: Atmospheres*, vol. 116, no. D12, 2011. [Online]. Available: <https://doi.org/10.1029/2010JD015139>
- [67] M. Nakanishi and H. Niino, “Development of an improved turbulence closure model for the atmospheric boundary layer,” *Journal of the Meteorological Society of Japan. Ser. II*, vol. 87, no. 5, pp. 895–912, 2009. [Online]. Available: <https://doi.org/10.2151/jmsj.87.895>
- [68] P. A. Jiménez, J. Dudhia, J. F. González-Rouco, J. Navarro, J. P. Montávez, and E. García-Bustamante, “A revised scheme for the wrf surface layer formulation,” *Monthly Weather Review*, vol. 140, no. 3, pp. 898–918, 2012. [Online]. Available: <https://doi.org/10.1175/MWR-D-11-00056.1>
- [69] K.-M. Xu and D. A. Randall, “A semiempirical cloudiness parameterization for use in climate models,” *Journal of the Atmospheric Sciences*, vol. 53, no. 21, pp. 3084–3102, 1996. [Online]. Available: [https://doi.org/10.1175/1520-0469\(1996\)053<3084:ASCPSU>2.0.CO;2](https://doi.org/10.1175/1520-0469(1996)053<3084:ASCPSU>2.0.CO;2)
- [70] S.-Y. Hong, Y. Noh, and J. Dudhia, “A new vertical diffusion package with an explicit treatment of entrainment processes,” *Monthly Weather Review*, vol. 134, no. 9, pp. 2318–2341, 2006. [Online]. Available: <https://doi.org/10.1175/MWR3199.1>

Appendices

.1 Appendix 1.

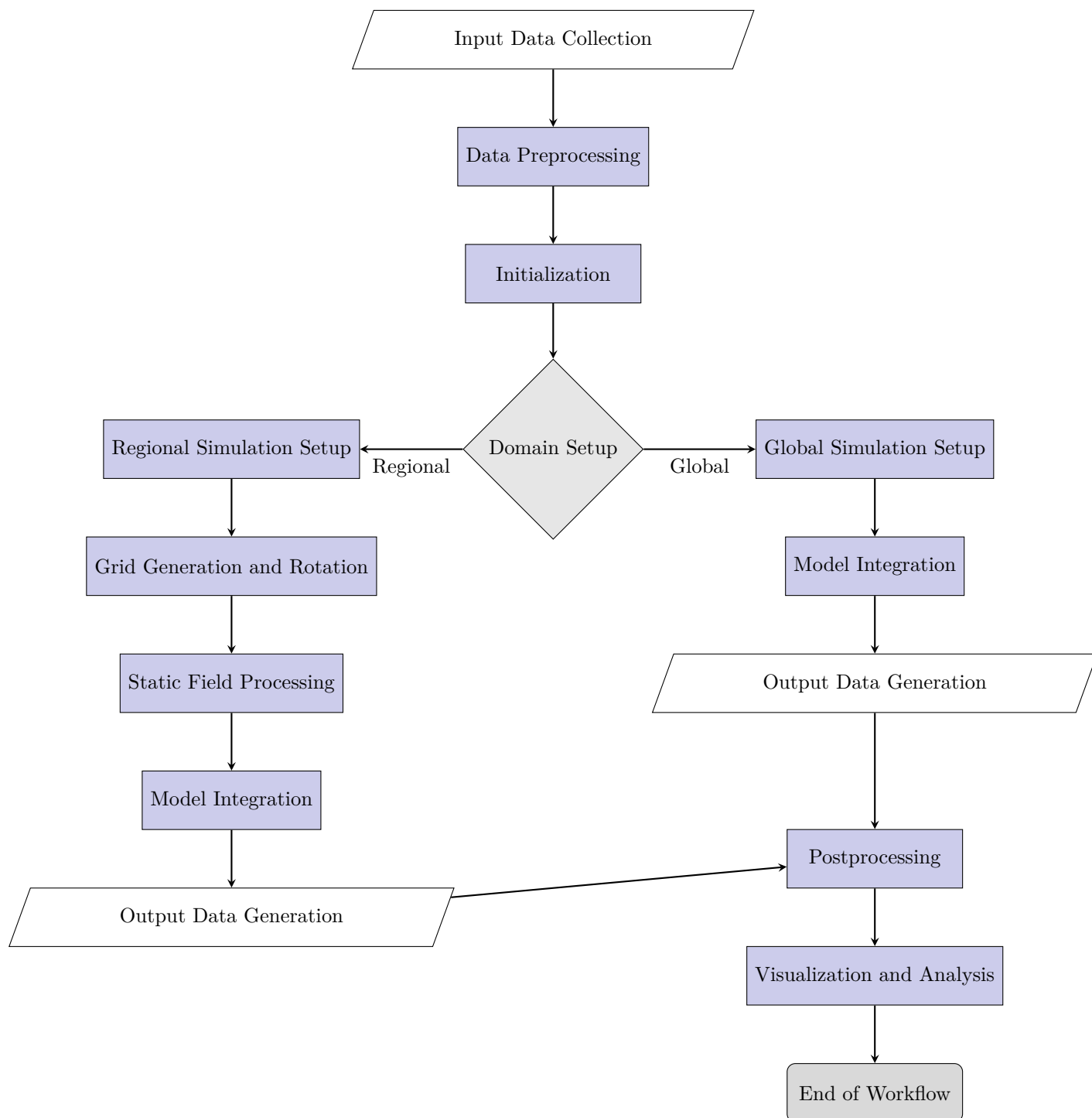


Figure 1: Workflow of MPAS-A Data Handling and Simulation.

.2 Additional Figures

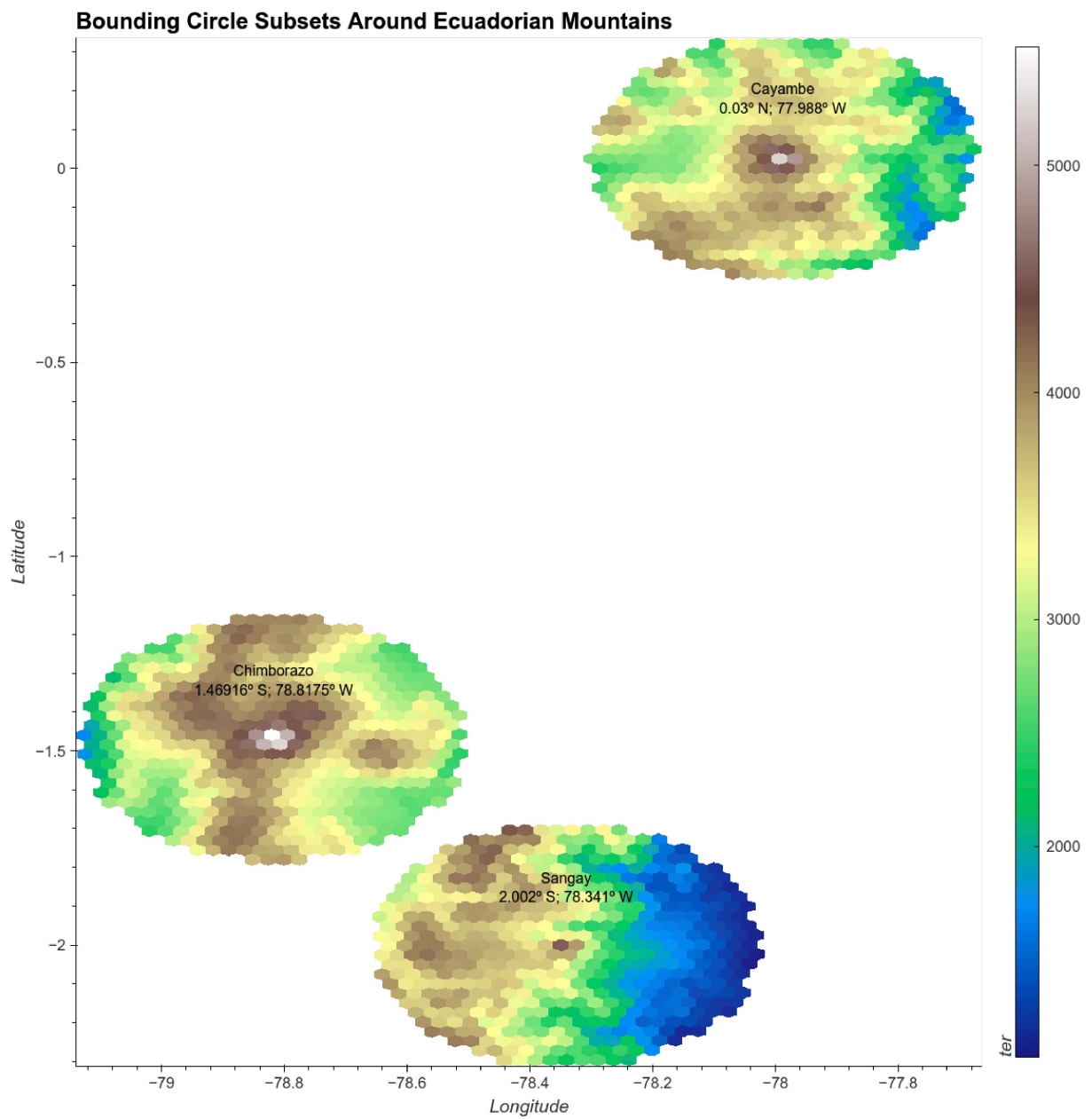


Figure 2: Bounding Circle Subsets Around Ecuadorian Mountains used in our study

.3 Appendix 2: MPAS-Atmosphere Configuration Files

We configured the model using two essential scripts: `namelist.init_atmosphere` and `namelist.atmosphere`. Each script is responsible for setting up specific model parameters, which define the initial and boundary conditions, physics, dynamics, and input-output operations for the simulations.

.4 `namelist.init_atmosphere`

The `namelist.init_atmosphere` script configures the initial conditions and geographical data sources necessary to initialize the model's atmospheric state and topography. Details about the structure of the file and the available options can be found in the MPAS-Atmosphere Model User's Guide Version 8.1.0.

```
1 &nhyd_model
2     config_init_case = 7
3     config_start_time = '2010-01-10_00:00:00'
4     config_stop_time = '2010-01-13_00:00:00'
5     config_theta_adv_order = 3
6     config_coef_3rd_order = 0.25
7     config_interface_projection = 'linear_interpolation'
8 /
9 &dimensions
10    config_nvertlevels = 55
11    config_nsoillevels = 4
12    config_nfglevels = 38
13    config_nfgsoillevels = 4
14 /
15 &data_sources
16    config_geog_data_path = '/glade/work/wrfhelp/WPS_GEOG/'
17    config_met_prefix =
18    ↪ '/hppfs/scratch/09/di35qib/CFSR/2010_01_10-12/CFSR_PGBH'
19    config_sfc_prefix = 'SST'
20    config_fg_interval = 21600
21    config_landuse_data = 'MODIFIED_IGBP_MODIS_NOAH'
22    config_topo_data = 'GMTED2010'
23    config_vegfrac_data = 'MODIS'
24    config_albedo_data = 'MODIS'
```

```

24     config_maxsnowalbedo_data = 'MODIS'
25     config_supersample_factor = 3
26     config_30s_supersample_factor = 1
27     config_use_spechumd = false
28 /
29 &vertical_grid
30     config_ztop = 30000.0
31     config_nsmterrain = 1
32     config_smooth_surfaces = true
33     config_dzmin = 0.3
34     config_nsm = 30
35     config_tc_vertical_grid = true
36     config_blend_bdy_terrain = true
37 /
38 &interpolation_control
39     config_extrap_airtemp = 'lapse-rate'
40 /
41 &preproc_stages
42     config_static_interp = false
43     config_native_gwd_static = false
44     config_vertical_grid = true
45     config_met_interp = true
46     config_input_sst = false
47     config_frac_seaice = true
48 /
49 &io
50     config_pio_num_iotasks = 0
51     config_pio_stride = 1
52 /
53 &decomposition
54     config_block_decomp_file_prefix = 'ecuador3km.graph.info.part.'
55 /

```

.5 namelist.atmosphere

The `namelist.atmosphere` script configures the simulation's dynamics and physics, setting parameters for time integration, physical schemes, and output. Details about the structure of the file and the available options can be found in the MPAS-Atmosphere Model User's Guide Version 8.1.0.

```
1 &nhyd_model
2     config_time_integration_order = 2
3     config_dt = 18.0
4     config_start_time = '2010-01-10_00:00:00'
5     config_run_duration = '3_00:00:00'
6     config_split_dynamics_transport = true
7     config_number_of_sub_steps = 2
8     config_dynamics_split_steps = 3
9     config_horiz_mixing = '2d_smagorinsky'
10    config_visc4_2dsmag = 0.05
11    config_scalar_advection = true
12    config_monotonic = true
13    config_coef_3rd_order = 0.25
14    config_epssm = 0.1
15    config_smdiv = 0.1
16 /
17 &damping
18     config_zd = 22000.0
19     config_xnutr = 0.2
20 /
21 &limited_area
22     config_apply_lbcs = true
23 /
24 &io
25     config_pio_num_iotasks = 0
26     config_pio_stride = 1
27 /
28 &decomposition
29     config_block_decomp_file_prefix = 'ecuador3km.graph.info.part.'
30 /
31 &restart
```

```
32     config_do_restart = false
33 /
34 &printout
35     config_print_global_minmax_vel = true
36     config_print_detailed_minmax_vel = false
37 /
38 &IAU
39     config_IAU_option = 'off'
40     config_IAU_window_length_s = 21600.
41 /
42 &physics
43     config_sst_update = false
44     config_sstdiurn_update = false
45     config_deepsoiltemp_update = false
46     config_radtlw_interval = '00:30:00'
47     config_radtsw_interval = '00:30:00'
48     config_bucket_update = 'none'
49     config_physics_suite = 'convection_permitting'
50 /
51 &soundings
52     config_sounding_interval = 'none'
53 /
```